Computational Fluid Dynamics Modeling of Projectile Drag in Baffled-Tube Ram Accelerator

Jubayer Abdullah Rafiul Alam

A thesis
submitted in partial fulfillment of the
requirements for the degree of

Master of Science in Aeronautics and Astronautics

University of Washington
2024

Committee:
Carl Knowlen
Robert Breidenthal

Program Authorized to Offer Degree:
Aeronautics and Astronautics

University of Washington

Abstract

Computational Fluid Dynamics Modeling of Projectile Drag in Baffled-Tube Ram Accelerator

Jubayer Abdullah Rafiul Alam

Chair of the Supervisory Committee:

Carl Knowlen

William E. Boeing Department of Aeronautics and Astronautics

The ram accelerator operates on principles similar to those of a ramjet engine. In the baffled tube ram accelerator (BTRA), projectiles operate below the Chapman-Jouguet detonation velocity in a thermally choked propulsive mode. Geometry variations of the projectile can significantly change its performance. This investigation aimed to determine the drag of projectiles with varying geometries using computational fluid dynamics (CFD). Nose cone angle, tail cone angle, shoulder diameter, and shoulder length were varied to investigate their influence on drag. The geometric parameters considered here were based on previous experiments conducted in a BTRA. The velocity of the projectile was also varied to understand its effect on drag. ANSYS FLUENT, utilizing the Reynolds-Averaged Navier-Stokes (RANS) equations with the k-omega SST turbulence model was used to solve the transient CFD models. Dynamic mesh with a constant velocity of 1000 m/s (Mach 2.82) was used to understand the interaction between the projectile and the baffle. A non-reactive methane-air mixture at 300 psig was set as the working fluid. The results indicated that a smaller nose cone angle produces less drag compared to a larger nose cone angle. Similarly, a smaller tail cone angle also contributed to lower drag. An increase in shoulder diameter led to higher drag when the shoulder length was fixed. The variation in shoulder length yielded interesting results, i.e., while shoulder lengths of 2 and 3 times the baffle length produced similar drag, a shoulder length of 2.5 times the baffle length resulted in 12% lower drag. For reference purposes, the projectile drags in smooth bore and free-flight were also determined.

Table of Contents

List of Figures

List of Tables

Glossary

Variables

A : Cross-sectional Area (m^2)

C_d : Drag Coefficient

D : Drag (N)

L : Characteristic length (m)

Re : Reynolds Number

U : Velocity (m/s)

ρ : Density (Kg/m^3)

μ : Viscosity (Ns/m^2)

Acronyms

BL : Baffle Length

BTRA : Baffled-Tube Ram Accelerator

TCRA : Thermally Chocked Ram Accelerator

Acknowledgments

First and foremost, I want to express my deepest gratitude to Dr. Carl Knowlen for the incredible opportunity to work in the UW Ram Accelerator Lab. His passion and dedication to the lab have been a constant source of inspiration for me. Under his mentorship, my understanding of compressible flow, gas dynamics, and aerospace propulsion has grown tremendously. Dr. Knowlen's down-to-earth attitude and patience have left a lasting impression on me.

I would also like to extend my heartfelt thanks to Dr. Breidenthal for his exceptional teaching in compressible fluids and vortex dynamics. His classes have been fundamental to my understanding of fluid mechanics, providing a solid foundation for my research.

A special thanks to my fellow grad students in the lab, Navid and John. I am deeply grateful to Navid for his invaluable guidance on CFD simulations and for the countless hours he spent with me on Zoom troubleshooting problems. I am equally thankful to John, who has been the backbone of the Ram Lab, always offering unwavering support and assistance.

Finally, I want to thank my friends and family for their unwavering support throughout the completion of this thesis. Your encouragement and belief in me have been instrumental in this journey.

1. Introduction

The ram accelerator development began in 1983 at the Department of Aeronautics and Astronautics at the University of Washington. (C. Knowlen, personal communication, 2023). There has been much research and development of the ram accelerator throughout the years [1–12]. The working principle of a thermally choked ram accelerator is quite like a ramjet engine [2]. Both require a minimum inlet velocity of the incoming air to gas dynamically start the diffuser, i.e., isentropic deceleration of incoming supersonic flow to sonic at the point of maximum flow constriction in the diffuser. This is referred to as the isentropic diffuser starting velocity. This velocity is supersonic but the exact value depends on the area contraction ratio and propellant properties [13].

1.1 Ram Accelerator Operating Principle

The operating principles of a ramjet engine vs. a thermally choked ram accelerator are shown in Figure 1. It is seen that both compress incoming supersonic flow with a conical diffuser and then use subsonic combustion to produce thrust. In a ramjet engine (Figure 1a), fuel is injected with injectors located behind the centerbody. The flow then undergoes subsonic combustion that is stabilized with a flame holder. After which, the flow is choked and accelerated to a supersonic exit velocity with a converging-diverging nozzle to produce thrust [14].

In the ram accelerator (Figure 1b), fuel is premixed in the entire tube. Projectiles are launched using a light gas gun above the isentropic diffuser starting velocity. When entering the ram accelerator, propellant ignition occurs that results in subsonic combustion behind the projectile and thermal choking of the flow in the tube. This combustion process creates a high-pressure zone on its base that continuously accelerates the projectile.

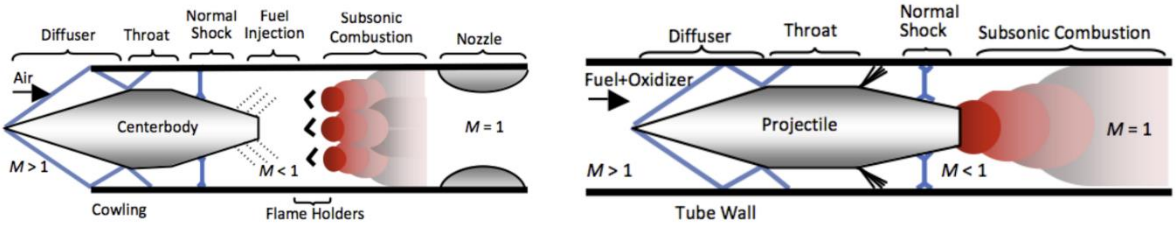

(a) (b)

Figure 1. (a) Air-breathing ramjet flow field. (b) Thermally choked ram accelerator flow field.

Projectiles in ram accelerators can operate in sub-detonative, trans-detonative and super-detonative velocity regimes [3] as shown in Figure 2. Here, the detonative velocity is the Chapman Jouguet detonation velocity V_{cj}, which depends on the propellant and the fill pressure used in the ram accelerator [1]. When projectiles reach super-detonative velocities, they operate as a scramjet engine [12].

Figure 2 shows representative ram accelerator operating modes in three different velocity regimes. Ram accelerator projectiles can continuously accelerate throughout the sub-detonative to trans-detonative to super-detonative velocity regimes. When the projectile velocity is within 0.85 V_{cj} to 1.15 V_{cj}, it is within the trans-detonative velocity regime. Operation in this velocity regime continues until the combustion zone moves completely up onto the projectile and makes a transition to a scram-type propulsive mode in the super-detonative velocity regime [3]. Within the trans-detonative velocity regime, the thrust reaches its minimum value.

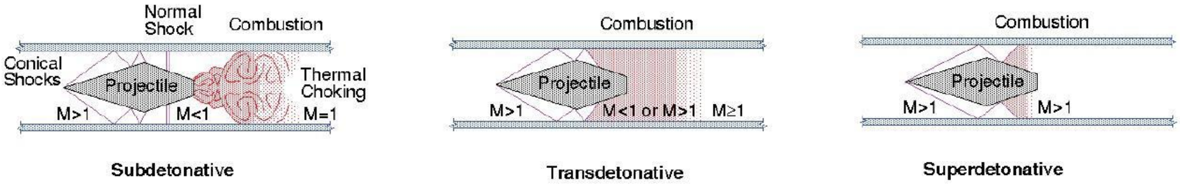

Figure 2. Ram accelerator operating modes within three different velocity regimes.

In this investigation, the projectiles were analyzed at velocities below the Chapman-Jouguet detonation velocity. This investigation aims to determine the drag of the projectile with varying geometric parameters, namely, nose cone angle, tail cone angle, projectile diameter, and projectile shoulder length. The effects of velocity and other flight conditions are subjects of interest as well.

1.2 Thermally Choked Ram Accelerator

Thermal choking occurs when heat addition accelerates flow to sonic velocity (Mach 1) at some point on or behind the projectile. Once the flow reaches Mach 1 in a constant area duct, further heating cannot increase flow Mach number. Instead, it increases the pressure and temperature of the combustion zone [15]. Thermally choked ram accelerators operate within the sub-detonative velocity regime. The propellant heat release and the reactant speed of sound also determine the value of V_{cj}. To start the propulsive cycle, the projectile velocity must be supersonic with respect to the in-tube propellant. The system of shocks generated as the projectile enters the propellant, initiates combustion, and causes the flow to thermally choke behind the projectile. This heat release drives a shockwave up onto the projectile body that renders the flow subsonic at its base, thereby increasing the static pressure and temperature of the flow at the entrance to the combustion zone behind the projectile [2].

Figure 3 shows the operating limit of a thermally choked ram accelerator. Stable operation of the TCRA is constrained by three things: a minimum Mach number, a maximum heat release, and a minimum heat release limit [4]. If the Mach number is below the isentropic diffuser limit, choking will occur at the projectile throat causing a diffuser unstart. This creates subsonic flow over the projectile nosecone and results in high drag. The throat diameter of the projectile governs its ability to contain the combustion wave behind the throat and stop it from passing through for a given amount of heat release. This mechanism results in what is referred to as a "wave unstart." Lastly, the minimum heat release is the heat required for the combustion wave to drive the projectile. If the heat release is below the required level, the combustion wave will fall-off and the projectile thrust will cease.

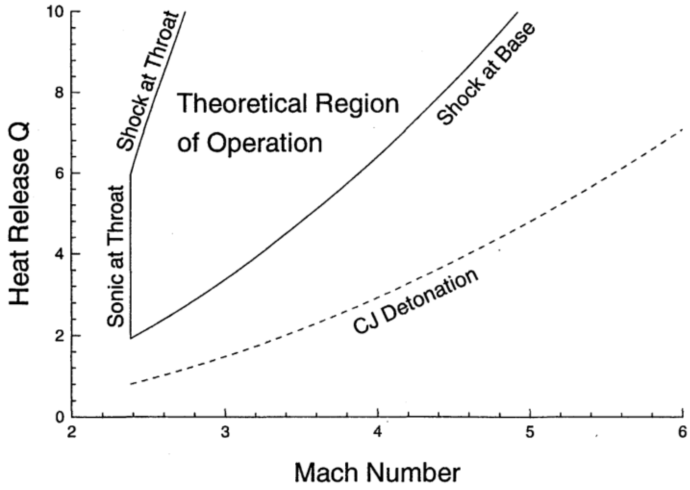

Figure 3. Theoretical operating envelope for a ram accelerator projectile having the throat and base diameter of an experimental projectile.

1.3 Baffled Tube Ram Accelerator

The baffled tube ram accelerator (BTRA) was introduced by the UW Ram accelerator laboratory in 2005 [9]. The BTRA has washer-like baffles with a hole slightly bigger than the projectile that forms sequential chambers, as shown in Figure 4a. It can reduce the minimum starting velocity and increase the maximum operational propellant heat release. In this manner, the BRTA can potentially produce up to three times more thrust when compared to the smooth bore ram accelerator operating at the same fill pressure [10]. Another advantage of the BRTA is that the projectiles can be stabilized by the baffles themselves and therefore they do not require fins and can be axisymmetric. Nonetheless, to guide the projectile and make the baffle chamber stronger, rails are often used (Figure 4a). The axisymmetric projectile configuration simplifies the manufacturing process and reduces their manufacturing cost.

Figure 4b shows the flow field of the BRTA as a projectile passes through the baffles. The projectile shoulder length must be at least one baffle chamber long to ensure it always is fully blocking at least one baffle to prevent pressure waves from the combustion process surging ahead of it. As it can be seen from the flow field schematics, the nose of the projectile enters a chamber and compresses the gas until the projectile shoulder reaches the hole in the baffle. At this point, a normal shock wave is driven ahead of the projectile that then expands radially into the chamber and is overtaken by the leading edge of the shoulder. Combustion behind the projectile creates a high-pressure zone at its base that is prevented from moving forward by the baffles. Thus, the baffle chambers act as one-way valves that allow the propellant to go past the projectile but keep the combustion driven pressure waves aft of the projectile [10].

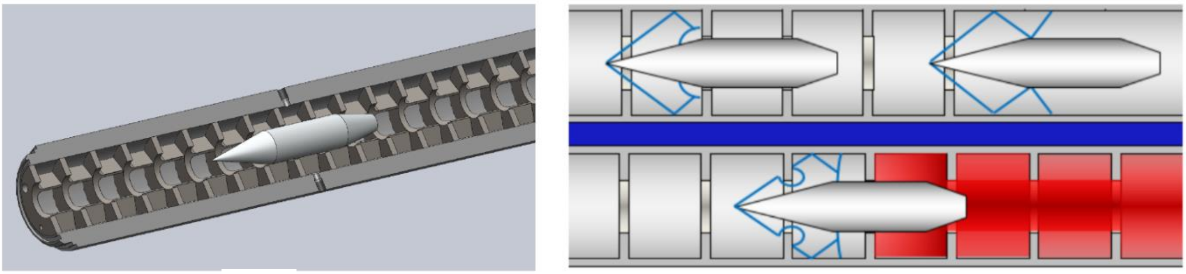

(a) (b)

Figure 4. (a) Axisymmetric projectile in baffled tube ram accelerator. (b) Baffled tube flow field as projectile passes through baffle with combustion being stabilized behind projectile.

1.4 Prior Investigations

An experimental study was done to investigate the influence of projectile geometry on its thrust performance [5]. Projectile thrust as a function of Mach number was considered the key figure of merit. It was found that smaller nose cone angles produced higher thrust at high Mach number whereas larger nose cone angles produced higher thrust at low Mach number. Smaller tail cone angles and longer shoulder lengths were found to produce higher thrust. In this CFD investigation, the drag of all the projectiles were determined at the same conditions, i.e., the same velocity, fill pressure and propellant mixture used in the experiments.

2. Theory

In this CFD investigation, the drags of various projectile geometries were determined. In general, aerodynamic drag, *D*, can be represented using the following formula:

$$D = \frac{1}{2}\rho U^2 A C_D$$

where ρ is flow density, *U* is velocity, *A* is reference area, and C_D is the drag coefficient. From this formula, it can be seen that the drag is proportional to the cross-sectional area of the moving body and its velocity squared [16]. Therefore, in this investigation, the drag is expected to increase for a higher cross-sectional area even though there will be significant interactions between the projectile and baffles.

Figure 5 shows the drag coefficients of objects with different shapes in subsonic flow. It can be seen that the objects with a rounded front edge create a smooth transition of flow direction [17]. Which keeps the flow attached to the body, resulting in lower drag. Similarly, the object with a long and tapered tail produces minimum boundary layer separation at the trailing edge, which reduces the adverse pressure gradient, lowers drag, and decreases drag coefficient.

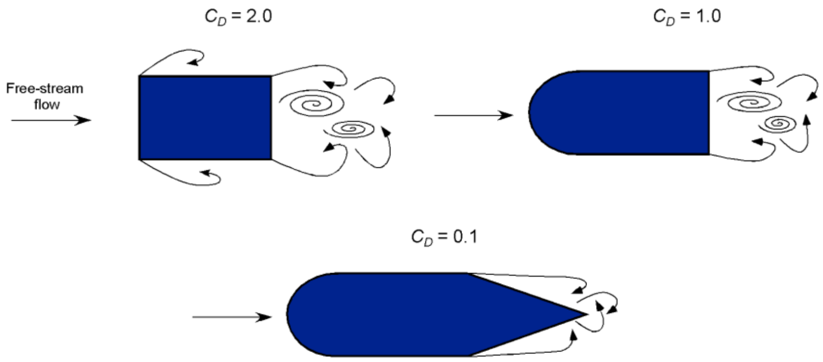

Figure 5. Drag coefficients of objects with different geometries [17].

In supersonic flow, the strength of the conical shock increases with increasing nose angle and the wake of the projectiles also plays an important role in drag. Just like in subsonic flow, a streamlined body will create a smaller wake and produce less drag when compared to a bluff body. Therefore, it is expected that a projectile with a longer nose and longer tail will produce less drag [16].

The Reynolds number also plays a role in determining the drag. The Reynolds number is a dimensionless number that represents the ratio of momentum force to viscous force in a fluid. The Reynolds number, *Re*, is defined as:

$$Re = \frac{\rho U L}{\mu}$$

where μ is viscosity and L is a characteristic length. The drag coefficient of a spherical object depends on Reynolds number and surface roughness as shown in Figure 6 [18]. For the cases considered in this study, the Reynolds number was calculated to be around $5\text{x}10^7$. Thus, at these high Reynolds numbers, the surface roughness is not expected to be significant.

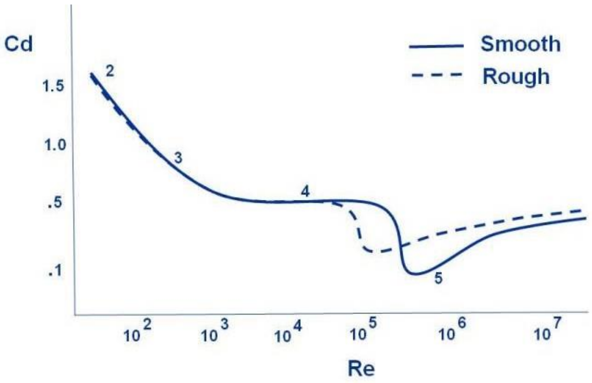

Figure 6. Drag coefficient vs. Reynolds number [18].

3. Geometry Variation

The geometry variations of the projectiles conformed to those used in the experiments done by Ginos (2023) [5]. For simplicity, only one geometric parameter was changed for each new variation. In this investigation, the nose cone angle, tail cone angle, projectile diameter, projectile shoulder length and projectile velocity were varied. The projectile drag was also compared in different confinement conditions, i.e., smooth bore and free-flight.

The three types of baffle inserts used in the baffled-tube ram accelerator for these experiments were BTRA 501, BTRA 501s and BTRA 111, as shown in Figure 7. For the CFD simulations carried out here, only the BTRA 111 insert was considered. The geometric details of the BTRA 111 insert are shown in Figure 8. Some of its features were simplified to make the CFD domain meshing easier.

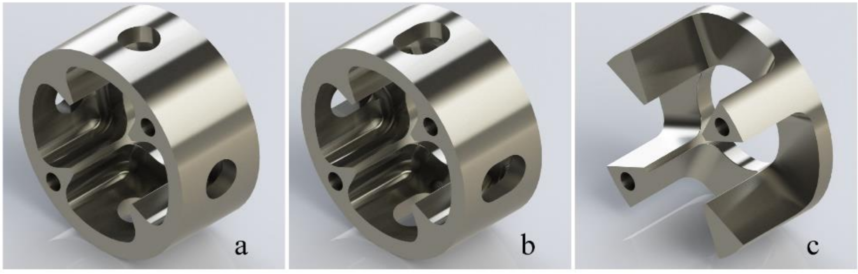

Figure 7. (a) Baffle insert BTRA 501 (b) Baffle insert BTRA 501s (c) Baffle insert BTRA 111.

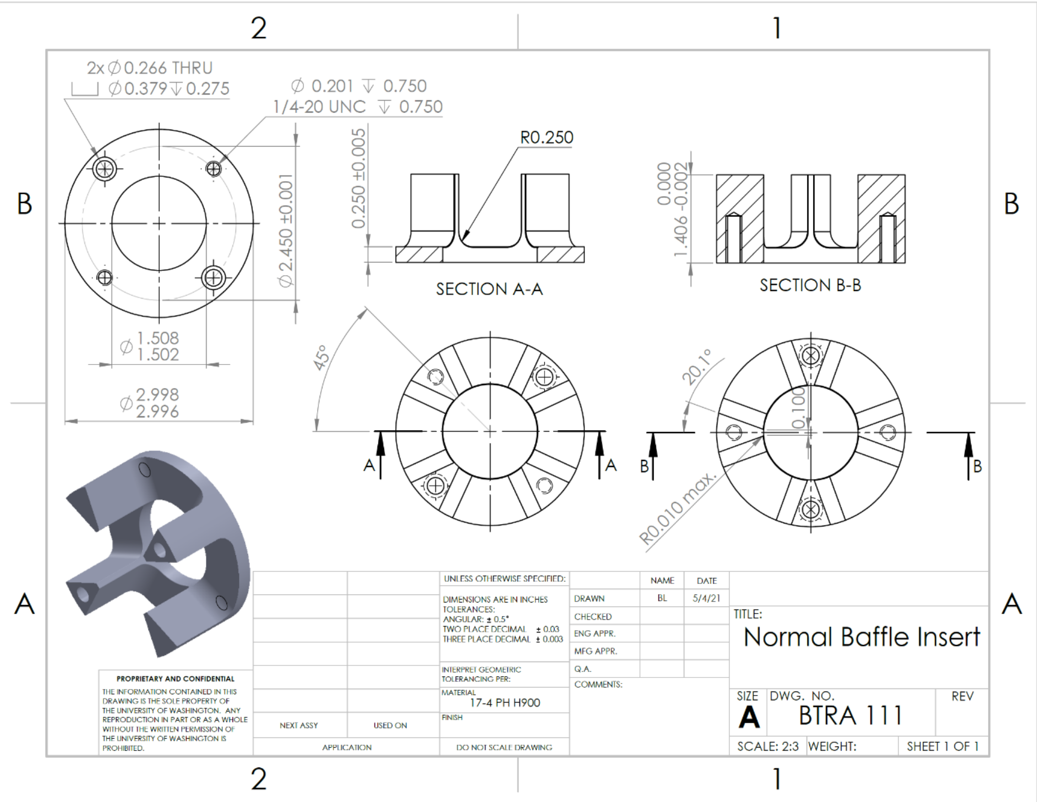

Figure 8. BTRA 111 geometric drawing.

There were four 2-m-long BTRA tubes in the experimental setup used for these experiments [5]. The first BTRA tube at the entrance to the test section mostly consisted of BTRA 111 baffle inserts (colored blue) as shown in Figure 9. Upon projectile entrance, its obturator would immediately recede as the combustion process was established and stabilized. The CFD simulations only considered the flow field of the projectile after the obturator had fallen back and before the propellant was ignited in the BTRA 111 inserts.

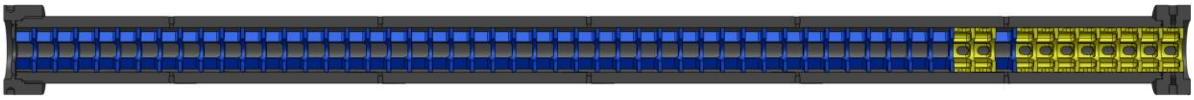

Figure 9. Baffle configuration with BTRA 111 baffles in blue.

Figure 10 shows the front view of the baffle rail extrusion, chamber, and projectile nose. The radius of the fillet was 0.25 inches. The radius of the entire domain was 1.498 inches. The height of the rails, whose edge is shown on upper right side of image, was 0.697 inches. Since the domain is 1/8th symmetry of the actual flow field, only half of the rail thickness was considered, which was 0.05 inches.

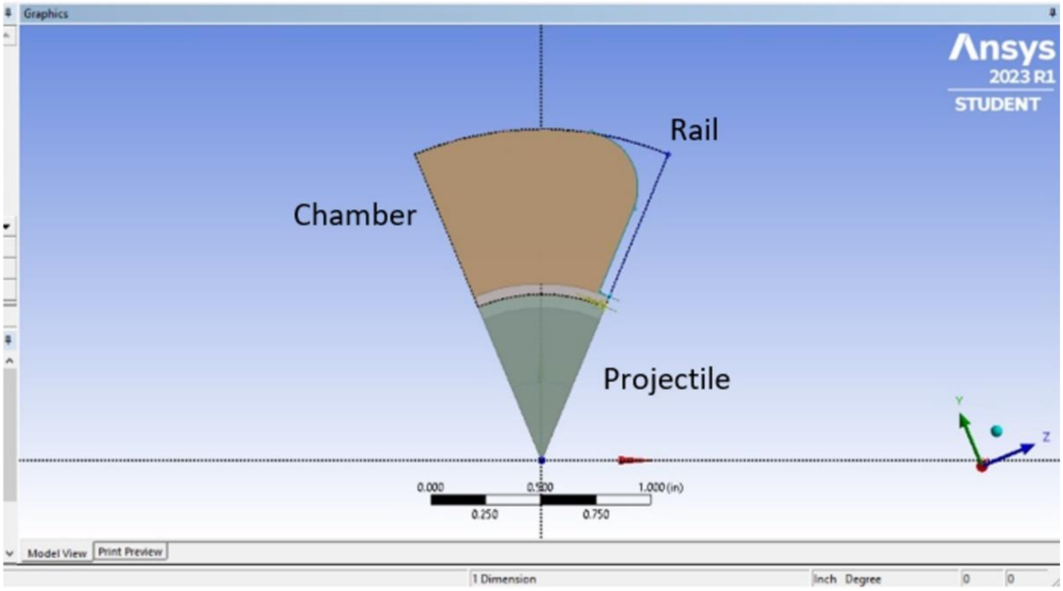

Figure 10. Front view of the baffle rail extrusion on the CFD domain.

Figure 11 shows the side view of the computational domain. The thickness of each baffle was 0.25 inches and the chamber width was 1.156 inches. The distance between the front face of each baffle was thus 1.406 inches, which defines the baffle length, BL.

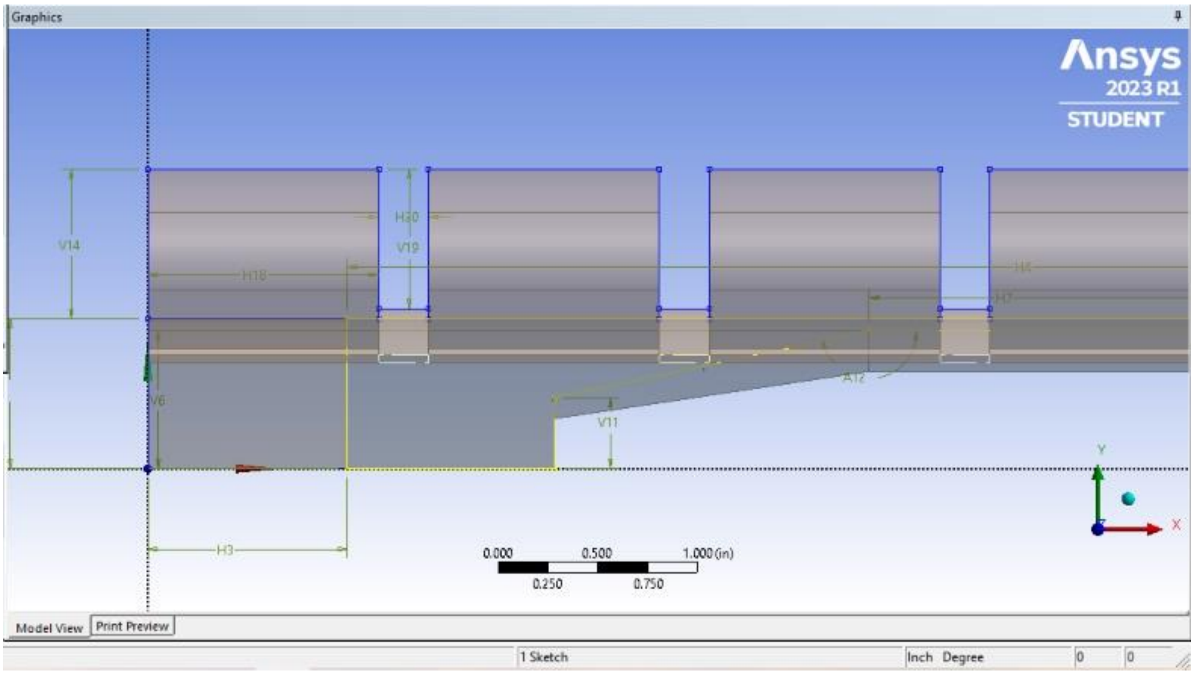

Figure 11. Side view of the baffle extrusion on the CFD domain.

To compare the effect of each projectile parameter, six different series were created: Nose cone, Tail cone, Diameter, Shoulder Length, Operating Condition and Velocity. The base diameter was kept the same at 0.71 inches for all of the projectiles. Every series except the velocity series had a constant velocity of 1000 m/s for all of its cases. The parameters for these projectile series are shown in Tables 1-6.

Table 1. Nose Cone Series.

Name	Nose angle	Tail angle	Shoulder length (in)	Diameter (in)	Mass (g)
P380-2BL-12-09	9°	12°	2.812	1.380	156
P380-2BL-12-12	12°	12°	2.812	1.380	144
P380-2BL-12-15	15°	12°	2.812	1.380	137
P380-2BL-12-18	18°	12°	2.812	1.380	132

Table 2. Tail Cone Series.

Name	Nose angle	Tail angle	Shoulder length (in)	Diameter (in)	Mass (g)
P380-2BL-09-15	15°	9°	2.812	1.380	145
P380-2BL-12-15	15°	12°	2.812	1.380	137
P380-2BL-15-15	15°	15°	2.812	1.380	131
P380-2BL-18-15	15°	18°	2.812	1.380	127

Table 3. Diameter Series.

Name	Nose angle	Tail angle	Shoulder length (in)	Diameter (in)	Mass (g)
P340-3BL-12-15	15°	12°	4.218	1.340	160
P360-3BL-12-15	15°	12°	4.218	1.360	170
P380-3BL-12-15	15°	12°	4.218	1.380	178
P380-2.5BL-12-15	15°	12°	3.515	1.380	157
P400-2.5BL-12-15	15°	12°	3.515	1.400	163
P420-2.5BL-12-15	15°	12°	3.515	1.420	169

Table 4. Shoulder Length Series.

Name	Nose angle	Tail angle	Shoulder length (in)	Diameter (in)	Mass (g)
P380-2BL-12-15	15°	12°	2.812	1.380	137
P380-2.5BL-12-15	15°	12°	3.515	1.380	157
P380-3BL-12-15	15°	12°	4.218	1.380	178

Table 5. Confinement condition Series.

Name	Condition
P380-2BL-12-15	Free Flight
P380-2BL-12-15	Smooth Bore
P380-2BL-12-15	Baffled Tube

Table 6. Velocity Series.

Name	Velocity
P380-2BL-12-15	800 m/s
P380-2BL-12-15	1000 m/s
P380-2BL-12-15	1200 m/s
P380-2BL-12-15	1400 m/s
P380-2BL-12-15	2000 m/s

The projectiles were all axisymmetric with the parameters being varied indicated in Figures 12 and 13. Figure 12 shows the projectile drawings of the nose cone series and the tail cone series. Figure 13 shows the projectile drawings of the diameter series.

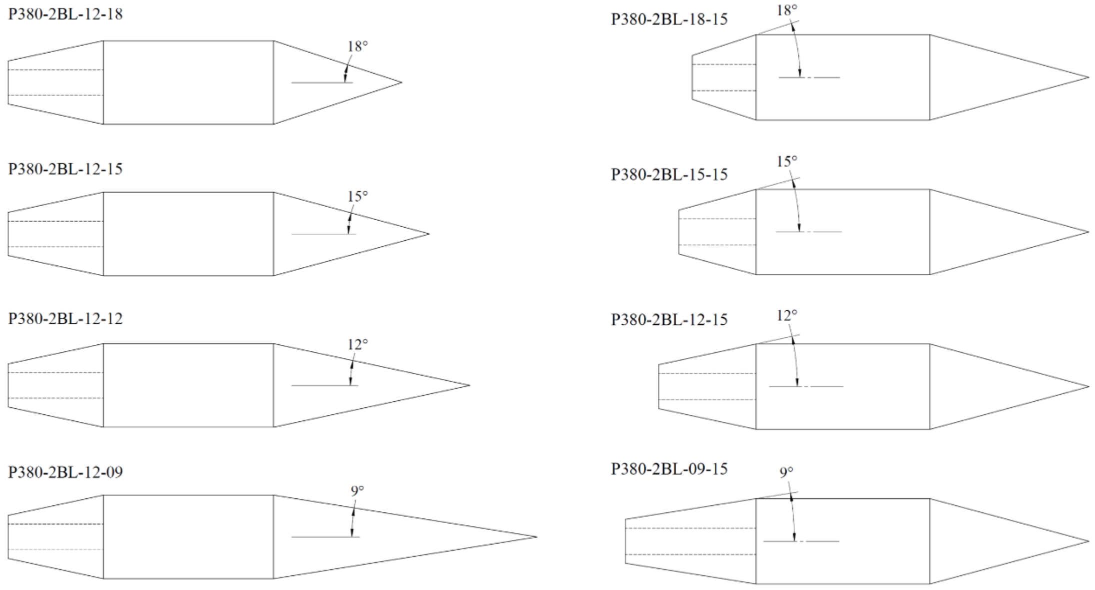

Figure 12 Nose cone series projectiles (left) and tail cone series projectiles (right).

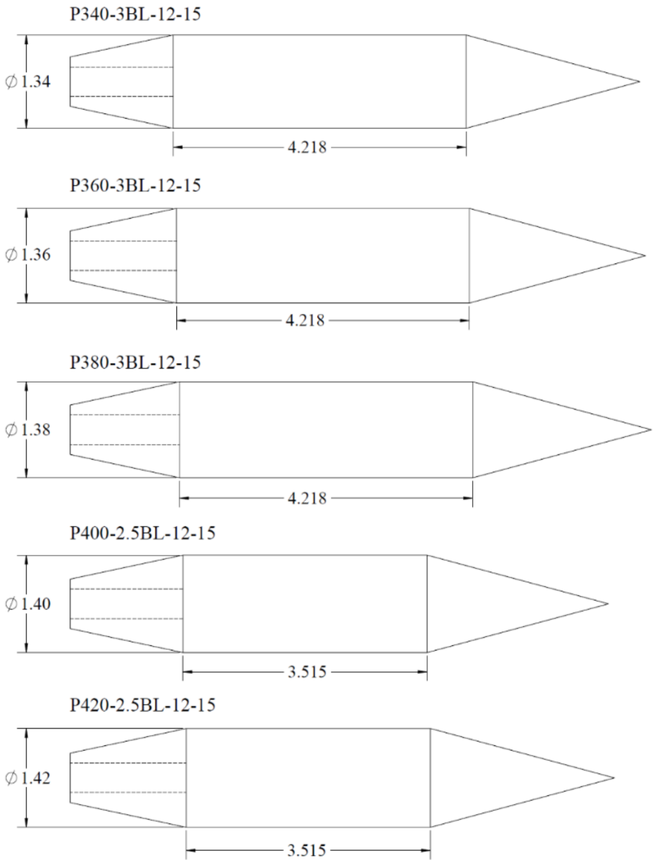

Figure 13. Diameter series projectiles.

4. CFD Modeling

4.1 Domain and Mesh Creation

CFD domains were designed using ANSYS design modeler. Domain dimensions were based on the actual geometry of the baffle tube and the projectiles. Some of the features were simplified to make meshing easier. 1/8th of the tube section with BTRA 111 baffles was created as the domain [6]. This was done to reduce the cell count in the domain needed to resolve the flow field phenomena of the simulation. Each domain had four different sections, with their surfaces attached to each other. The sections were named b1, b2, b3 and b4. After creating a 3D drawing, meshing was done in ANSYS. Various sections had different cell sizes depending on their significance on result accuracy as shown in Table 7. The total number of cells was around 500k for most of the domains. Figure 14 shows the finished domain. The details of meshing are discussed in the appendix section.

Table 7. Mesh sizes.

Domain Section	Cell size (in)	Other sizing(s)
b1	0.33	N/A
b2	0.05	6-layer Inflation around the projectile
b3	0.33	N/A
b4	0.08	Face sizing in 3 different places

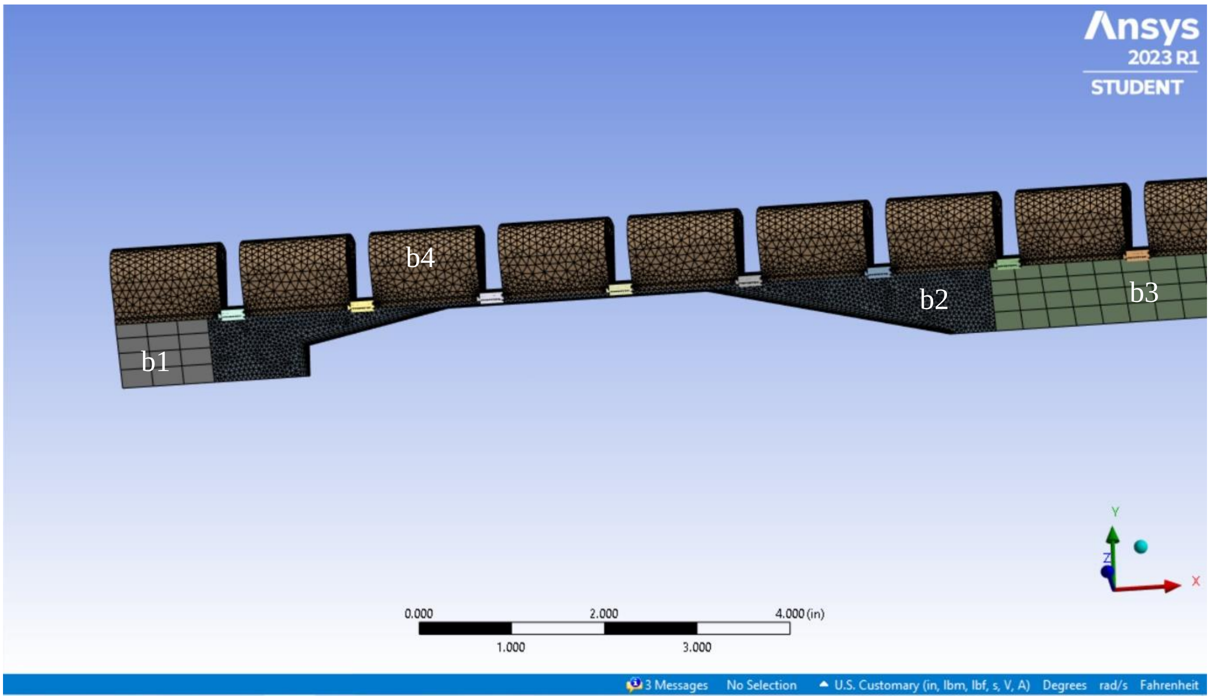

Figure 14. Generated mesh with four sections b1, b2, b3 and b4.

Accurate CFD simulations have low residual values. This is usually achieved by decreasing the cell size and increasing the cell number. In this investigation, the total number of cells was optimized to get the most accurate result with the lowest possible cell number to keep the simulation times less than 12 hours. For a standard 2BL projectile, the value was found to be around 503k cells. The cell number was increased to around 881k cells to see if there were any significant differences in the simulation solution. The difference in the result was found to be less than 1%, yet the computational time was around 40% longer. Similarly, an attempt to decrease the cell number by increasing the cell size and de-featuring the domain produced results that were not useful. Therefore, a cell number of 503k was deemed to be appropriate for this study. It was found that time step size had a bigger impact on the simulation accuracy than cell size.

4.2 Dynamic Mesh

In this CFD investigation, projectiles with different geometries were considered for the simulations. For all the geometry variations, the projectile velocity was assumed to be a constant velocity of 1000 m/s. A User Defined Function (UDF) was created to maintain this projectile velocity as it passed through the computational domain. The dynamic mesh feature was deployed based on this UDF. With time, the domain section b2 (contains the projectile) moved as directed by the UDF. As a result, the domain section behind the projectile, b1 elongated and the section in front of the projectile b3 shortened. At a certain point, b2 would move further than the cell sizes in b1 and b3, which created a negative volume in b3. To fix this, the mesh in b1 was set to automatically generate new cells if the last cells (touching b2) become too long. Similarly, the cells in b3 were set to collapse if the last cells became too small. This way, the simulation was carried out without creating negative volume.

4.3 Solver setup

After completing the mesh, it was exported as a FLUENT input file (msh) to be used as an input file for ANSYS on the ram1 workstation. The solver parameters were set as shown in Figure 15, and dynamic mesh was implemented. The details of the solver setup are discussed in the appendix section. The model used to simulate the turbulence was K omega SST (Shear Stress Transport) with compressibility effect. The working fluid of the simulation was a stoichiometric methane-air mixture at 300 psi with an ideal gas density model and constant viscosity. This model is based on RANS (Reynolds Average Navier Stokes). The solver used was implicit AUSM (Advection Upstream Splitting Method) with a courant number of 0.2. It was found that this courant number kept the residuals from oscillating with high amplitude. Higher-order relaxation with a relaxation factor of 0.75 was selected for better convergence.

The time required to solve a case was dependent on the number of iterations, which depended on the time step size or dt. The dynamic mesh moved the projectile at a constant velocity.

Therefore, a small value of dt would move the projectile slowly between each frame whereas a higher dt would move the projectile quickly. Different values of dt were used to find a value of dt that would provide a good result in a realistic time. It was found that when dt = 2.5e-6s, it took the solver around 300 time steps and seven hours to solve the case. This value was doubled to see the effect and it was found that it reduced the result resolution. Conversely, dt was halved to 1.25e-6s to see its effect. It took the solver around 600 time-steps and 14 hours to solve the case. However, this case did not converge for dt = 1.25e-6 as the residuals blew up before the end of the simulation. The result showed oscillating patterns with very high amplitudes that indicated that the solution was unstable.

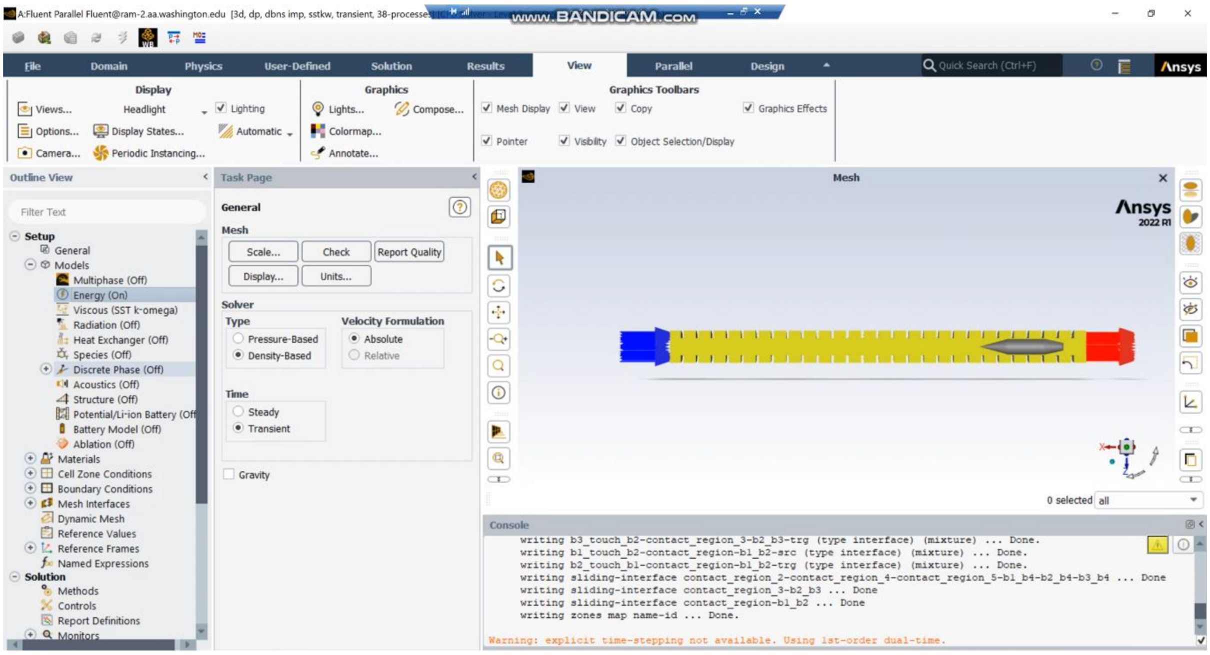

General

Mesh

Scale... Check Report Quality Display... Units...

Solver

Type: ○ Pressure-Based ● Density-Based

Velocity Formulation: ● Absolute ○ Relative

Time: ○ Steady ● Transient

☐ Gravity

0 selected all

Console

```
    writing b3_touch_b2-contact_region_3-b2_b3-trg (type interface) (mixture) ... Done.
    writing b1_touch_b2-contact_region-b1_b2-src (type interface) (mixture) ... Done.
    writing b2_touch_b1-contact_region-b1_b2-trg (type interface) (mixture) ... Done.
    writing sliding-interface contact_region_2-contact_region_4-contact_region_5-b1_b4-b2_b4-b3_b4 ... Done
    writing sliding-interface contact_region_3-b2_b3 ... Done
    writing sliding-interface contact_region-b1_b2 ... Done
    writing zones map name-id ... Done.

Warning: explicit time-stepping not available. Using 1st-order dual-time.
```

Figure 15. Solver setup on Ansys fluent.

5. Results and Discussion

5.1 Projectile Flow Visualization

Figure 16 shows the flow field static pressure contours of projectile P380-2BL-12-09. The pressure is highest at the nose cone of the projectile. The baffles upstream of the projectile have a constant pressure of 300 psi. At the tail of the projectile, pressure is the lowest. This happens because of an adverse pressure gradient leading to flow separation caused by skin friction.

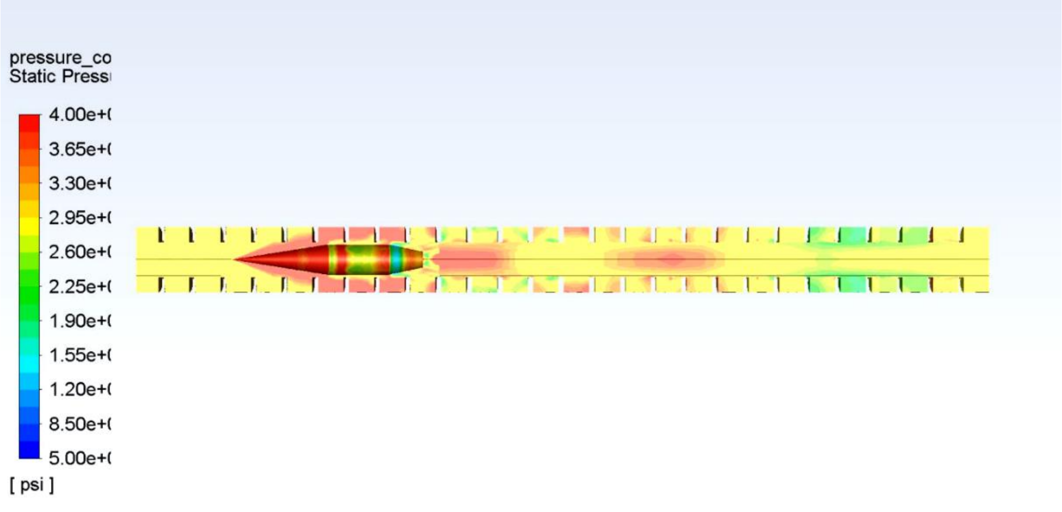

Figure 16. Pressure contour of P380-2BL-12-09 projectile at 1000 m/s.

Figure 17 shows the flow field static temperature contours of projectile P380-2BL-12-09. It is evident that the maximum temperature was at the projectile surfaces at around 680 K. The temperature upstream of the projectile remains constant at 300 K, whereas a 100% temperature increase can be seen in the wake of the projectile. This projectile was assumed to be adiabatic, thus its temperature indicated the flow temperature at its surface.

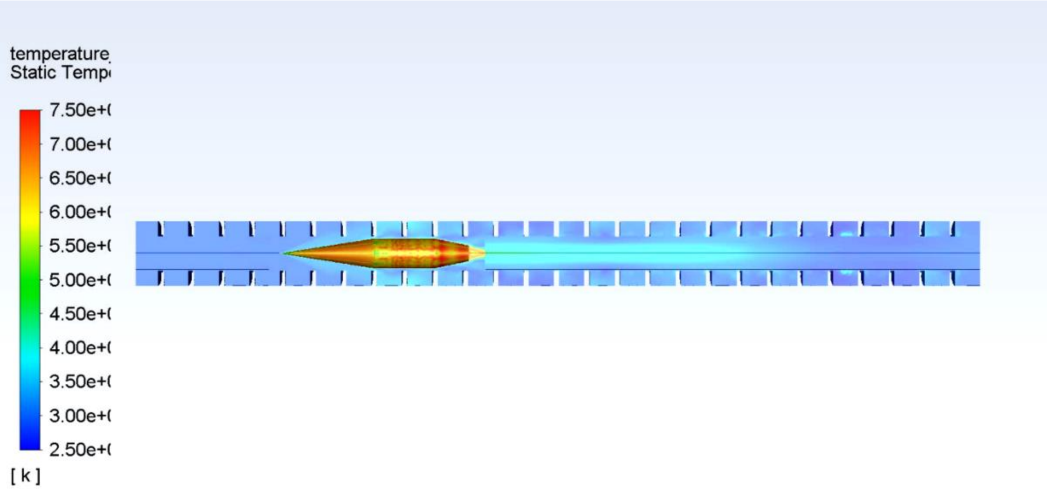

Figure 17. Temperature contour of P380-2BL-12-09 projectile at 1000 m/s.

Figure 18 shows the flow field Mach number contours of projectile P380-2BL-12-09 in the laboratory reference frame. Fluid velocity and Mach number are maximum at the wake of the projectile. Here, the projectile has a constant velocity of 1000 m/s. The inlet and outlet of the tube had zero velocities and had the same pressure of 300 psi, which makes the fluid inside the tube remain static unless disturbed.

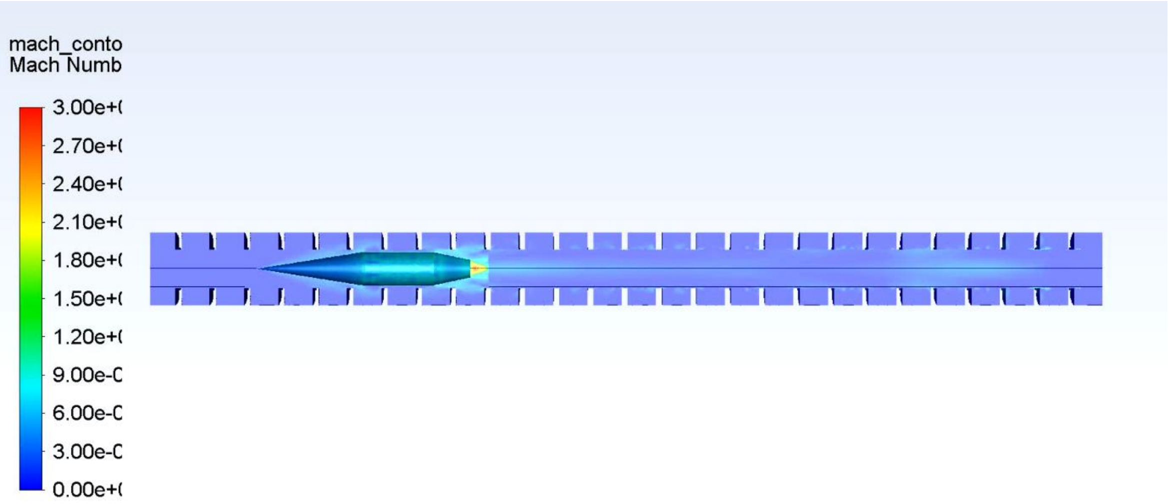

Figure 18. Mach number contour of P380-2BL-12- 09 projectile at 1000 m/s.

Figure 19 shows flow field density contours of the P380-2BL-12-09 projectile. The density increases in the high-pressure zone and decreases in the low pressure zone. Initially, the fluid density was 22.8 kg/m^3 inside the tube, which is indicated by the teal-colored regions.

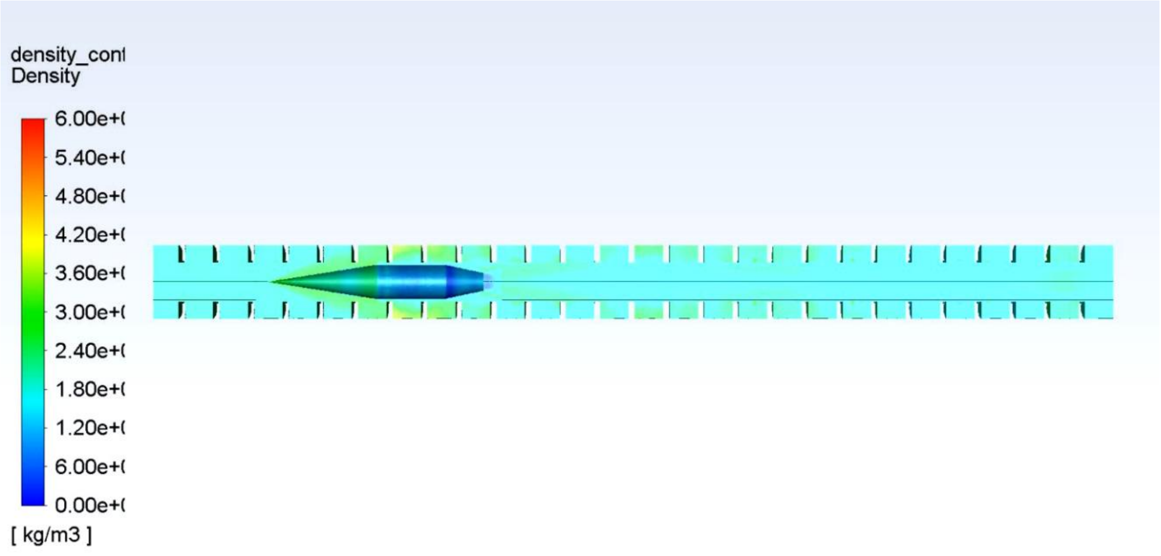

Figure 19. Density contour of projectile P380-2BL-12-09 at 1000 m/s.

Figure 20 shows the pressure contour of P380-2BL-18-15 and P380-2BL-09-15. At the tail of P380-2BL-18-15, the pressure is much lower, indicating flow separation at that region. Circular spots behind the base could be eddies generated from this flow separation. Whereas the P380-2BL-09-15 projectile maintains a high pressure region at its tail.

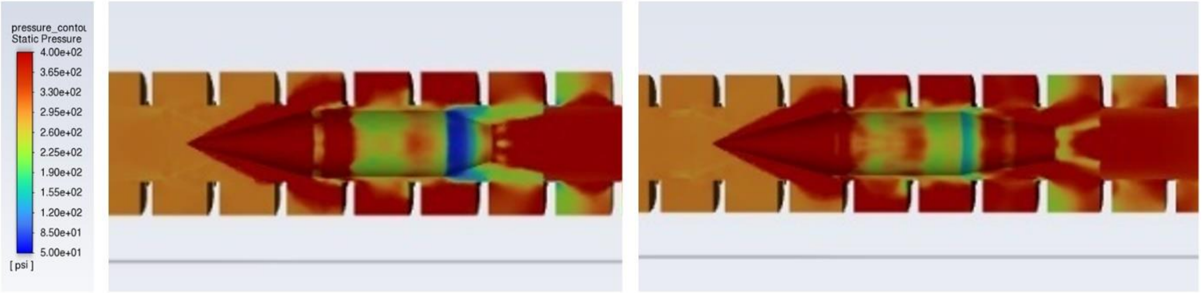

Figure 20. Pressure contour of P380-2BL-18-15 (left) and P380-2BL-09-15 (right) at 1000 m/s.

5.2 Case results

After obtaining the out file, the drag results were plotted on MATLAB. Figure 21 shows the time-history of the P380-2BL-12-15 projectile component drags at a velocity of 1000 m/s. In the beginning of the simulation, drag values were not close to their actual values. With more iterations, the component drags reached oscillatory states about steady values. The nose drag and the tail drag exhibited the highest oscillations, which were likely caused by wave interactions with the baffles as the projectile passed through them. The component drags were summed to get the time-history of the net drag acting on the projectile.

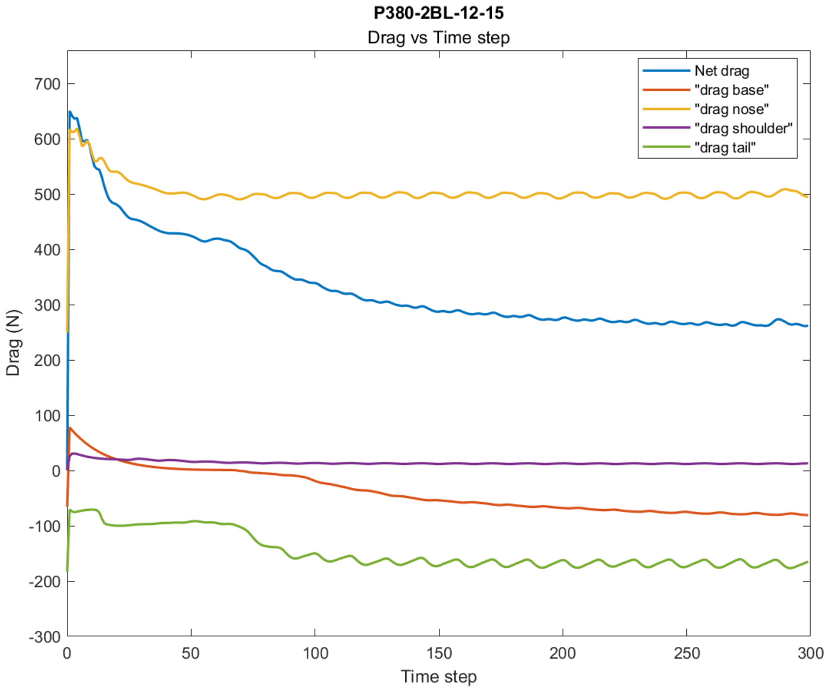

Figure 21. Drag vs. time step of projectile P380-2BL-12-15 at 1000 m/s.

5.3 Comparison Data

From Figure 21, it can be seen that the drag components take 200 or more iterations before reaching a stable oscillation. To get accurate values for component drags, the last five oscillating periods were averaged. The start of the period was selected based on the end value to get full oscillation periods. The net drag was averaged in the same manner and used as the primary figure-of-merit as shown in Tables 8-13. Note, negative drag indicated force was acting in the direction of projectile motion.

Table 8. Nose cone series drag at V = 1000 m/s.

Name	Nose (N)	Shoulder (N)	Tail (N)	Base (N)	Total drag (N)
P380-2BL-12-09	372	12	-161	-52	171
P380-2BL-12-12	427	12	-168	-64	207
P380-2BL-12-15	499	12	-169	-77	266
P380-2BL-12-18	588	13	-177	-86	338

Table 9. Tail cone series drag at V = 1000 m/s.

Name	Nose (N)	Shoulder (N)	Tail (N)	Base (N)	Total drag (N)
P380-2BL-09-15	498	14	-217	-58	237
P380-2BL-12-15	499	12	-169	-77	266
P380-2BL-15-15	499	14	-124	-83	306
P380-2BL-18-15	499	13	-90	-90	332

Table 10. Diameter series drag at V = 1000 m/s.

Name	Nose (N)	Shoulder (N)	Tail (N)	Base (N)	Total drag (N)
P340-3BL-12-15	469	20	-185	-51	253
P360-3BL-12-15	484	20	-197	-48	258
P380-3BL-12-15	499	20	-207	-48	265
P380-2.5BL-12-15	499	17	-224	-59	233
P400-2.5BL-12-15	519	16	-242	-57	237
P420-2.5BL-12-15	538	15	-258	-55	241

Table 11. Shoulder length series drag at V = 1000 m/s.

Name	Nose (N)	Shoulder (N)	Tail (N)	Base (N)	Total drag (N)
P380-2BL-12-15	499	12	-169	-77	266
P380-2.5BL-12-15	499	17	-224	-59	233
P380-3BL-12-15	499	20	-207	-48	265

Table 12. Velocity series drag with P380-2BL-12-15 projectile.

Velocity	Time step (s)	Nose (N)	Shoulder (N)	Tail (N)	Base (N)	Total drag (N)
800 m/s	2.5x10^{-06}	422	10	-224	-59	148
1000 m/s	2.5x10^{-06}	499	12	-169	-77	266
1200 m/s	2.5x10^{-06}	598	18	-80	-58	477
1400 m/s	2.5x10^{-06}	711	23	-75	-16	643
2000 m/s	1.25x10^{-06}	1144	40	-47	-6	1130

Table 13. Confinement condition series drag with P380-2BL-12-15 projectile at V = 1000 m/s.

Confinement condition	Nose (N)	Shoulder (N)	Tail (N)	Base (N)	Total drag (N)
Baffled Tube at 300 psig	499	12	-169	-77	266
Smooth Bore at 300 psig	496	15	-195	-36	280
Free Flight at 300 psig	509	13	-82	-33	407
Free Flight in atmosphere	39	2	1	0	42

5.4 Nose Cone series

In the nose cone series, all projectiles had a constant velocity of 1000 m/s. The nose cone angles were 9°, 12°, 15° and 18°. The drag on the four projectile components along with the total drag of each of the variations of this series were plotted in Figure 22. The highest nose cone drag of 588 N was experienced by P380-2BL-12-18 projectile. The nose cone drag decreased with decreasing nose cone angles. The drag decreased by 15% for 15°, 27% for 12° and 36% for 9° nose cone angle.

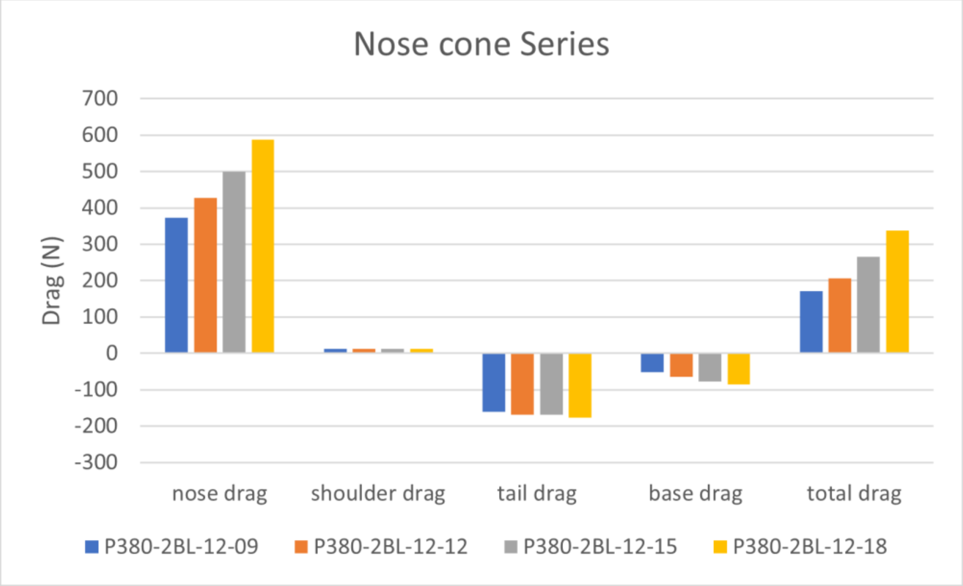

Figure 22. Drag comparison of nose cone series.

Shoulder drag was due only to shear forces and remained around 12 N for all projectiles. Interestingly, larger nose cone angles decreased both the tail and base drags as shown in Figure 22. One possible explanation is that stronger shocks generated by the larger nose cone angles created higher pressure in the baffle chambers around the shoulder that raised the pressure on the tail cone of the projectile as it cleared the baffle openings and resulted in higher base pressure, leading to higher negative drag. Nonetheless, as most of the drag was generated by the nose cone, the trend for total drag was to increase with increasing nose cone angle.

5.5 Tail Cone Series

All projectiles in the tail cone series had a constant velocity of 1000 m/s. The tail cone angles were 9°, 12°, 15° and 18°. Nose drag and shoulder drag remained almost unchanged for different projectiles at around 500 N and 13 N respectively, as shown in Figure 23. The P380-2BL-09-15 projectile had the smallest tail cone angle and had the lowest tail drag at -217 N, followed by P380-2BL-12-15 with 22% higher drag, P380-2BL-15-15 with 42% and P380-2BL-18-15 with 58%. This trend can be explained by the smaller turning angle associated with smaller tail cone angles having less flow separation and thus smaller wakes, resulting in reduced drag [16]. However, base drag increased with decreasing tail cone angle. This may be caused by the higher turning angle at the end of the tail cone resulting in more flow separation at the base and thus less pressure recovery and higher base drag [16]. In any case, it is clear that the tail cone drag is the dominating factor in drag variation. As a result, P380-2BL-09-15 had the lowest total drag of 237 N, followed by P380-2BL-12-15 with a 12% higher drag, P380-2BL-15-15 with 29% and lastly, P380-2BL-18-15 with 40%.

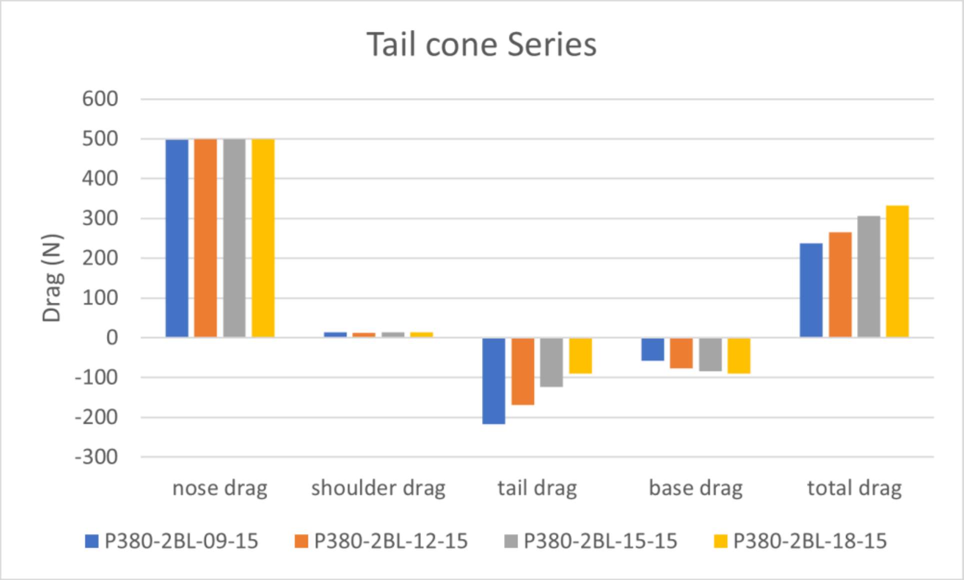

Figure 23. Drag comparison of tail cone series.

5.6 Diameter Series

Simulations of projectiles in the diameter series were carried out at a constant velocity of 1000 m/s. Two different shoulder lengths of 2.5BL and 3BL were used. The projectile diameter was varied from 1.34 inches to 1.42 inches with an increment of 0.02 inches. The component drags for each case are shown in Figure 24. The highest nose drag of 538 N was experienced by P420-2.5BL-12-15 followed by P400-2.5BL-12-15 with 3.5% lower nose drag, P380-2.5BL-12-15 and P380-3BL-12-15 had similar nose drags of 499 N, which is 7% less than P420-2.5BL-12-15. Whereas P360-3BL-12-15 had 10% and P340-3BL-12-15 had 12% less nose drag than P420-2.5BL-12-15. Therefore, a clear correlation between the projectile diameter and nose drag was found; i.e., larger projectile diameters resulted in higher nose cone drags. This was expected because the cross-sectional area is proportional to drag and the amount of gas pushed ahead of the projectile as it passes through the hole in the baffle increases because of increased occlusion (less diametric clearance).

Shoulder drag increased with shoulder length as expected due to shear forces. Shoulder length did not affect the nose drag yet it influenced base and tail drag, which will be further discussed in the shoulder length series. Larger diameters produced lower tail drag, which is due in part to there being more tail cone surface for the expanding gas in the chambers to act upon. P420-2.5BL-12-15 projectiles had the lowest tail cone drag of -257 N, followed by P400-2.5BL-12-15 with 6% higher drag, P380-2.5BL-12-15 with 13%, P380-3BL-12-15 with 20%, P360-3BL-12-15 with 23% and lastly P340-3BL-12-15 with 28%. There was a difference in base drag due to shoulder length, however, Figure 24 clearly shows that the net drag for a given shoulder length increased with increasing shoulder diameter.

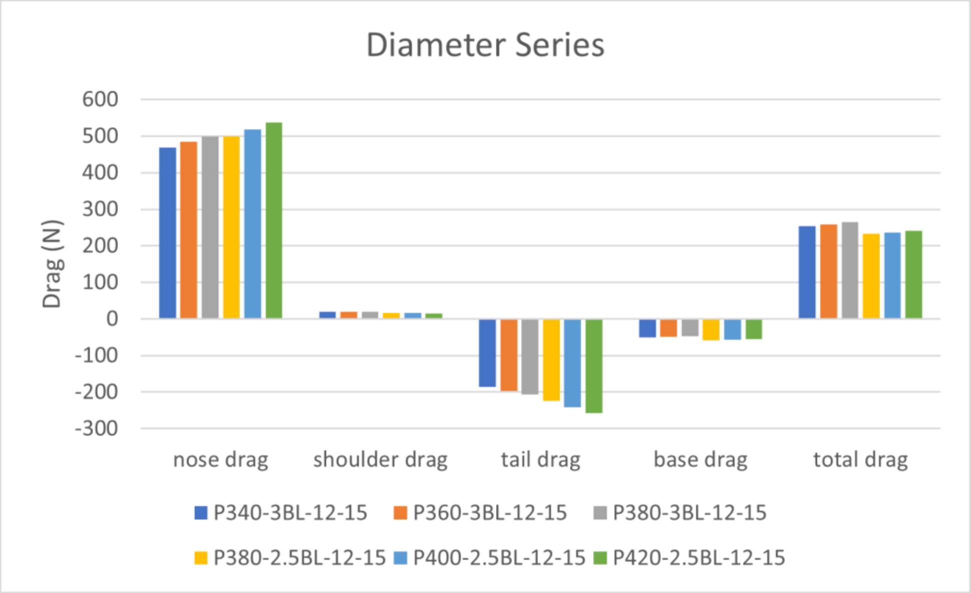

Figure 24. Drag comparison of diameter series.

5.7 Shoulder Length Series

Projectiles in the shoulder length series were modeled at a constant velocity of 1000 m/s. Figure 25 shows the drag comparison of the shoulder length series. In this series, nose drag of approximately 500 N is almost the same for all projectiles. The small changes in values can be attributed to the difference in CFD domain shape. Shoulder drag increased with the shoulder length due to viscous effects. Interestingly, P380-2.5BL-12-15 had the lowest tail drag of -224 N, followed by P380-3BL-12-15 with an 8% increase and P380-2BL-12-15 with 24%. Clearly, the shoulder length increase does not decrease the tail drag linearly. It could be that at 2.5BL, the end of the projectile shoulder is midway between baffles which allows more pressure recovery to occur on the tail cone. This result is to be the subject of further investigation.

The lowest base drag of -77 N was experienced by P380-2BL-12-15, followed by P380-2.5BL-12-15 with a 23% increased drag and P380-3BL-12-15 with 38%. The total drag was similar for P380-3BL-12-15 and P380-2BL-12-15 at around 265 N whereas P380-2.5BL-12-15 had a 12% lower drag.

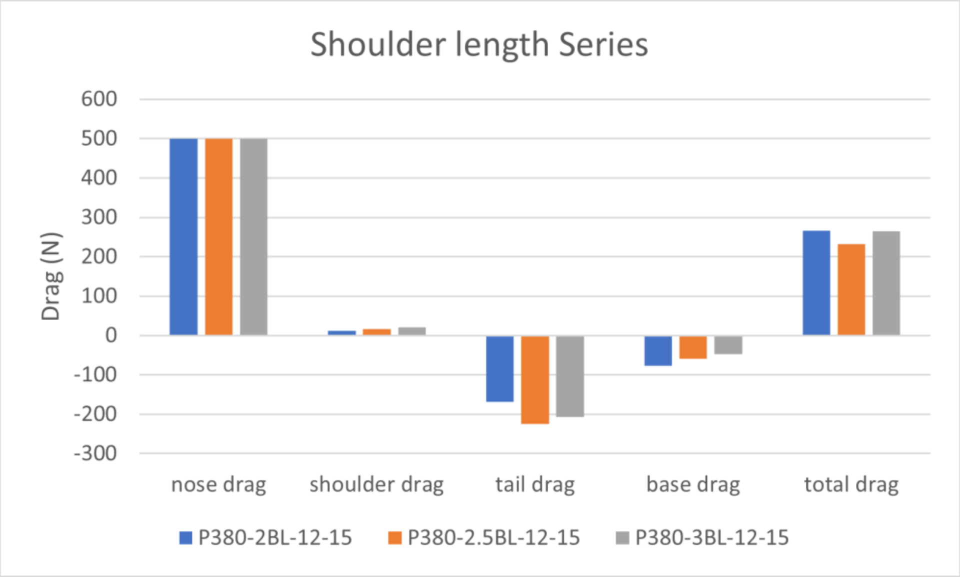

Figure 25. Drag comparison of shoulder length series.

5.8 Velocity Series

In the velocity series simulations, the P380-2BL-12-15 projectile was passed through the BTRA domain at velocities of 800 m/s, 1000 m/s, 1200 m/s, 1400 m/s, and 2000 m/s to quantify the drag dependence on Mach number for a sharp-nosed projectile in a baffled tube. Figure 26 shows the drag comparison of the velocity series. Because aerodynamic drag is proportional to the velocity squared, it was expected that all component drags would show this effect. This was indeed observed for all drag components as the velocity increased except for the projectile base, which actually had a higher base drag at 800 m/s than 1000 m/s. The highest net drag of 1130 N was experienced by the projectile at 2000 m/s, the drag decreased by 43% at 1400 m/s, at 1200 m/s it decreased by 58%, 76% at 1000 m/s and lastly, by 87% at 800 m/s. Therefore, a clear indication of drag increase with velocity increment can be seen in Figure 26.

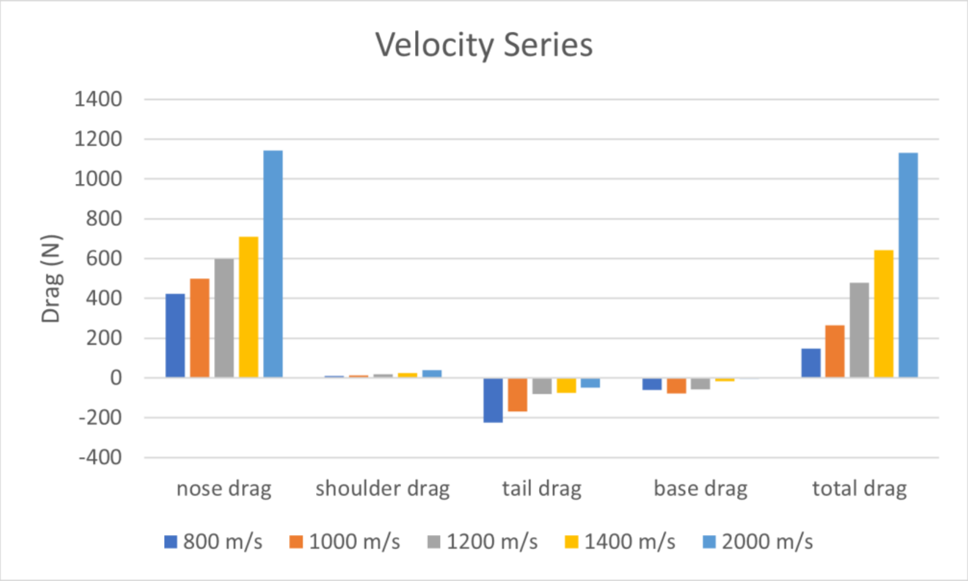

Figure 26. Drag comparison of velocity series.

5.9 Confinement Condition Series

In the confinement condition series, the P380-2BL-12-15 projectile was simulated at a constant velocity of 1000 m/s to determine its drag in a smooth bore tube and at free flight in the same methane-air mixture and at the same pressure for comparison with its baffled tube drag. Figure 27 shows the drag results of the confinement condition series. The projectile in free flight produced the highest nose drag of 509 N, in baffle it had 2% less drag, and in smooth bore, it had 2.5% less drag. The shoulder drag was highest in the smooth bore at 15 N, in the baffled tube it was 10% and in free flight, it was 17% less. The tail drag was lowest in smooth bore with -195 N, followed by baffle with 13% and 58% higher tail drag. The base drag was lowest in the baffle with -77 N, followed by the smooth bore with 53% and free flight with 58% higher tail drag.

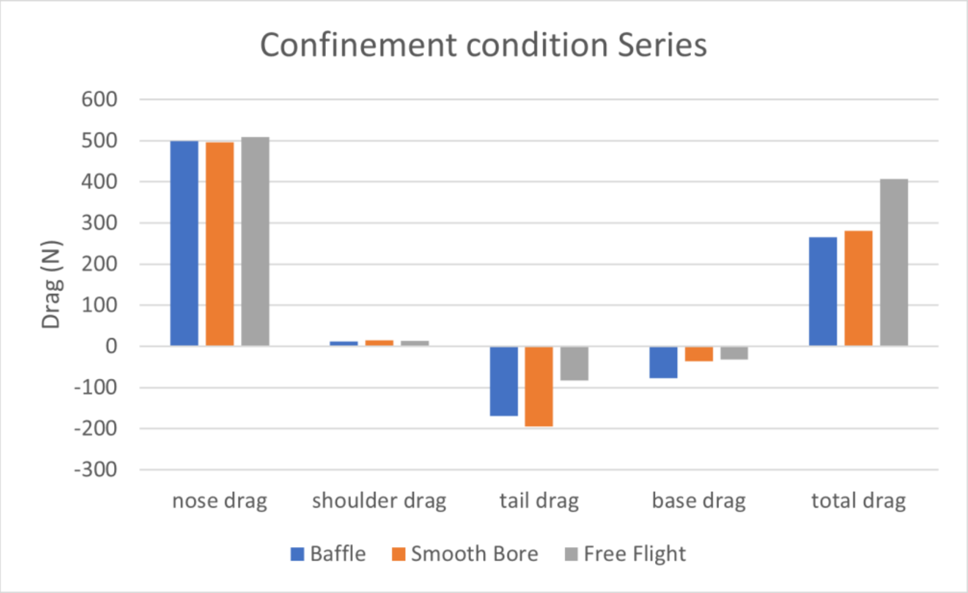

Figure 27. Drag comparison of confinement condition series.

Overall, the net drag was highest in free flight at 407 N followed by a 31% decrease in smooth bore and a 35% decrease in baffle. One possible explanation of this trend can be understood by the effect of baffles on flow over the projectile. The baffles impeded the forward motion of the flow being pushed by the projectile, which resulted in higher pressure recovery at the base of the projectile, and thus higher negative drag. Projectile in free flight experienced the highest drag due to the unrestricted flow over the tail and base of the projectile, creating lower negative drag.

5.10 Experimental Thrust vs. CFD Drag

In this section, the thrust measured from the experiments [5] is compared with the total drag calculated in the CFD simulation. The thrust values obtained from the experiments were subject to many variables. As the projectile moved forward, the velocity increased due to the combustion. Thrust was found to be maximum for these projectile geometry variations at around Mach 3, which occurs about 3-4 m from the entrance to the BTRA test section [5].

The ram tube had different baffle inserts at different sections. Thrust values of the projectile in baffle BTRA 111 and BTRA 501s (first two 2m baffled tube test sections) were recorded in the plots to compare them against drag. Figure 28 shows the thrust vs. drag relationship of the projectiles in the nose cone series. In the BTRA 111, Projectile P380-2BL-12-12 had the highest thrust of 8.7kN. P380-2BL-12-09 had 5% less thrust and P380-2BL-12-18 had 8% less thrust than P380-2BL-12-12. The thrust was lowest for P380-2BL-12-15 with 5.5kN, which is 37% less than P380-2BL-12-12. Interestingly, when the projectiles moved to the second tube containing BTRA 501s inserts, P380-2BL-12-15 had the highest thrust of 13.4kN. Compared to that, P380-2BL-12-18 had 16%, P380-2BL-12-09 had 28% and P380-2BL-12-12 had 31% less thrust. No direct correlation of thrust with nose cone angle and drag is seen in either BTRA section. Note, the net drag force was less than 5% of the thrust, thus its impact may not be apparent at the resolution of thrust measurements presented here.

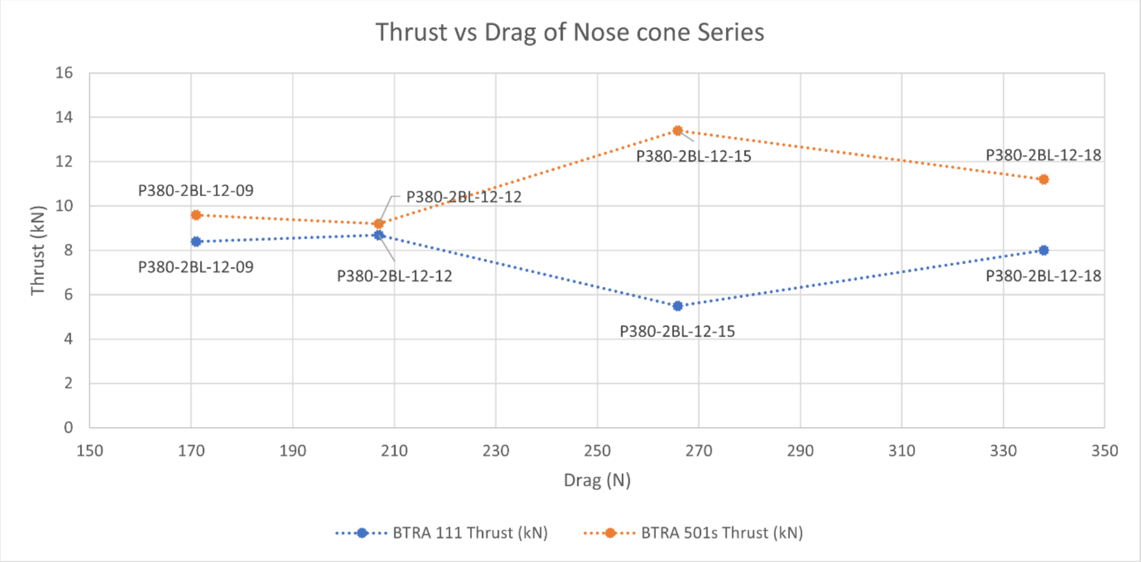

Figure 28. Thrust vs. drag plot of nose cone series.

Figure 29 shows the thrust vs. drag relationship of the projectiles in the tail cone series. In the first tube section, Projectile P380-2BL-15-15 had the highest thrust of 9.6kN whereas P380-2BL-09-15 had 9% and P380-2BL-18-15 had 20% less thrust. The thrust was lowest for P380-2BL-12-15 with 5.5kN, 42% less than P380-2BL-15-15. In BTRA 501s inserts, P380-2BL-12-15 had the highest thrust of 13.4kN. Compared to that, P380-2BL-09-15 had 19%, P380-2BL-

15-15 had 21% and P380-2BL-18-15 had 22% less thrust. No direct correlation of thrust with tail cone angle and drag is seen yet projectile thrust increased as they entered the second tube section.

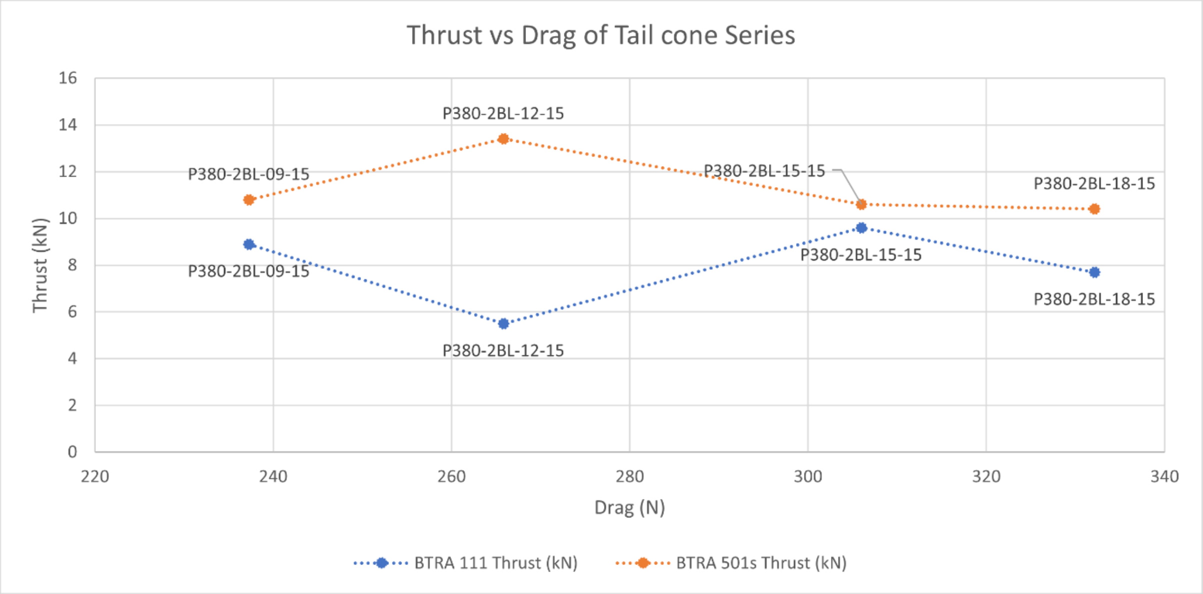

Figure 29. Thrust vs. drag plot of tail cone series.

Figure 30 shows the thrust vs. drag relationship of the projectiles in the diameter series. In BTRA 111, Projectile P380-3BL-12-15 had the highest thrust of 12.4kN. P420-2.5BL-12-15 had 4%, P360-3BL-12-15 and P340-3BL-12-15 had 6% and P400-2.5BL-12-15 had 15% less thrust than P380-3BL-12-15. In BTRA 501s, P360-3BL-12-15 had the highest thrust of 14.1kN, P380-3BL-12-15 had 4% less, P400-2.5BL-12-15 had 6% less, P340-3BL-12-15 had 8% less and P420-2.5BL-12-15 had 27% less thrust. No direct correlation of thrust with projectile diameter and drag is seen yet projectile thrust increased as they entered the second tube section except for P420-2.5BL-12-15.

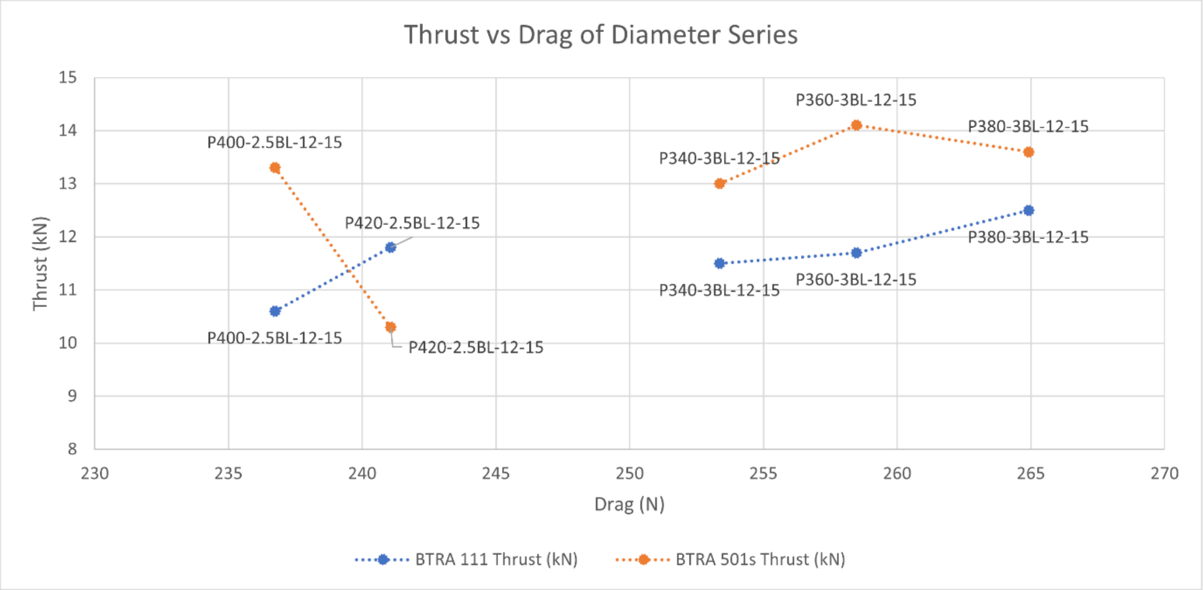

Figure 30. Thrust vs. drag plot of diameter series.

5.11 Drag Coefficient

In this section, the drag coefficient of projectile P380-2BL-12-15 was calculated for different velocities and confinement conditions. Figure 31 shows the Drag Coefficient vs. Mach of projectile P380-2BL-12-15. The drag coefficient increased with Mach number until Mach 3.4, reaching the highest drag coefficient of 0.242. The drag coefficient decreased to 0.24 at Mach 4, and by 14% at Mach 5.6. This trend of gradual increase of drag coefficient up to a certain Mach number and then plateauing was expected from empirical studies [16]. Note, the relatively small variations in drag coefficient indicate that even with the influence of baffles, the drag was generally proportional to the square of the velocity.

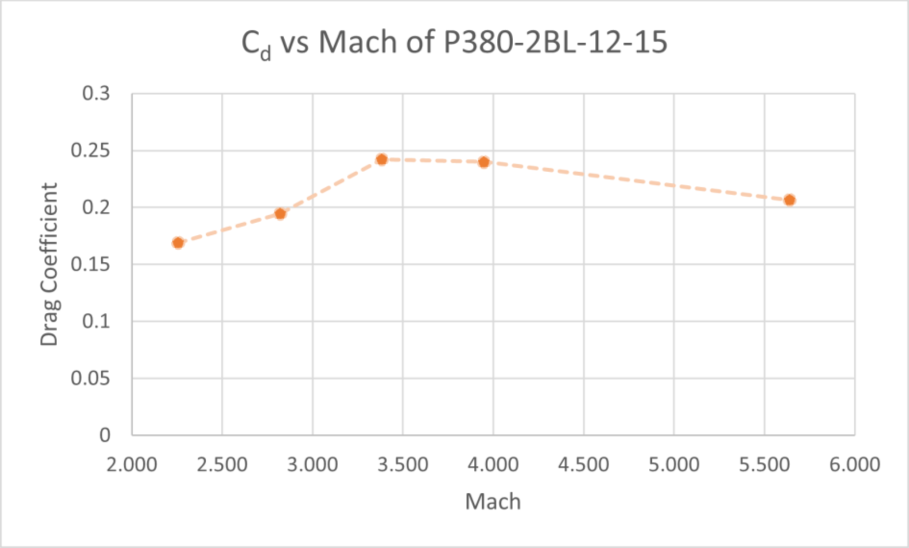

Figure 31. C_d vs. Mach of P380-2BL-12-15.

Figure 32 shows the drag, thrust and C_d vs. Mach for the P380-2BL-12-15 projectile. From the figure, thrust increased drastically from Mach 2.77 and peak thrust was obtained at Mach 3.1. Thereafter the thrust dropped by 28% at Mach 3.46 and further dropped by 40% at Mach 3.72. The drag increased with increasing Mach, whereas the drag coefficient peaked at Mach 3.4.

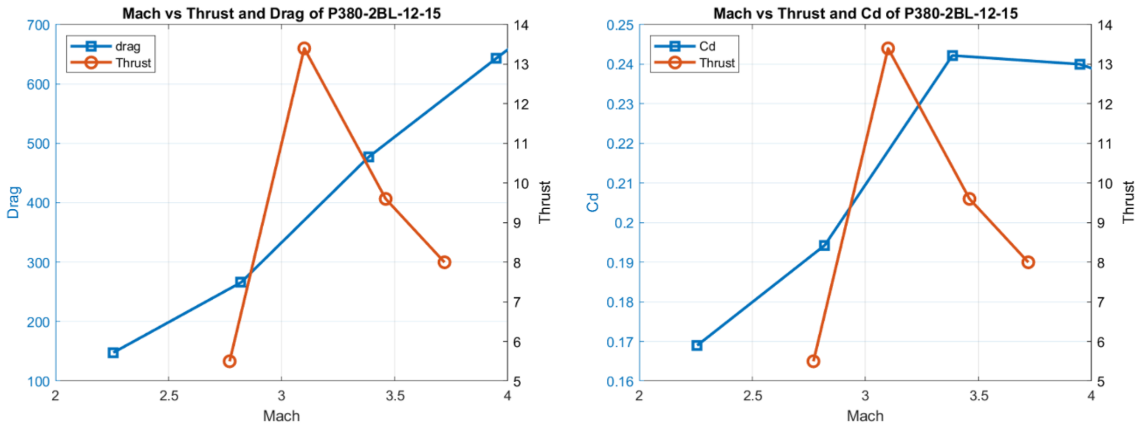

Figure 32. P380-2BL-12-15 projectile (Left) Drag and thrust vs. Mach. (Right) C_d and thrust vs. Mach.

Figure 33 shows the drag coefficient of P380-2BL-12-15 projectile in different confinement conditions. It was found that the drag coefficient was highest at 0.298 in free flight in the atmosphere at 14.7 psia using air and methane-air at 300 psig. The drag coefficient was decreased by 32% in the smooth bore and 35% in the baffled tube.

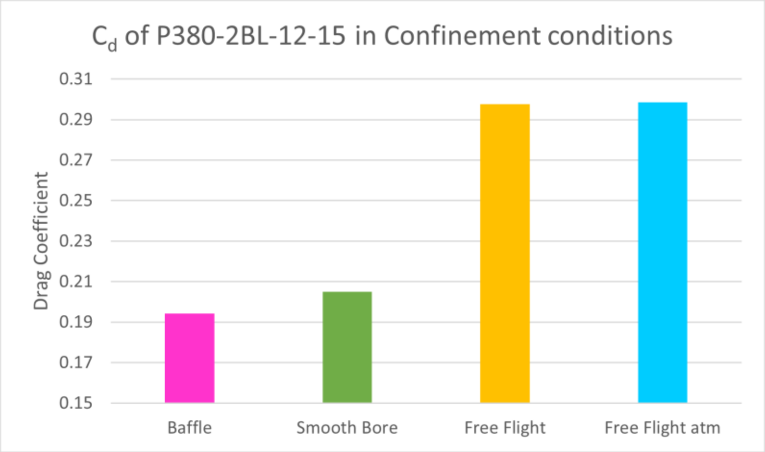

Figure 33. Drag Coefficient of P380-2BL-12-15 in different confinement conditions.

6. Conclusion and Future Plan

6.1 Conclusion

Transient, 3-D simulations at constant velocity were conducted with non-reacting flow to determine the projectile drag in a baffled tube ram accelerator. The nose cone series, tail cone series, diameter series and velocity series showed clear trends of their influences on drag. It was found that projectiles with smaller nose cone angles, smaller tail cone angles and smaller diameters produce less drag. The shoulder length series found that projectiles with a shoulder length of 2.5 times the baffle insert length had 12% less drag than projectiles with shorter and longer shoulder lengths suggesting there might be an ideal shoulder length for a given projectile at a certain velocity to minimize drag.

Increasing the projectile velocity increases the total drag roughly as the square of velocity as expected. Whereas at the same velocity and pressure, projectiles in free flight (i.e., without being confined by a tube) had the highest drag due, the drag in smooth bore tubes was second highest, and drag in baffled tubes was the lowest. These results were attributed to the forward motion of the gases in the BTRA chambers being stopped, resulting in higher pressure recovery over the rear end of the projectile.

CFD drag predictions was compared with experimental thrust results, however, there was no correlation found. It was postulated that because the drag force was less than 5% of the thrust force, its influence was not readily apparent in the experiments.

6.2 Future Plan

Future studies can be done on the shoulder length series in different velocities to understand why 2.5BL produced the least drag. This series can also be expanded with more shoulder lengths between 2BL and 3BL to better understand shoulder length’s influence on drag.

Another line of research is to determine the influence of baffle chamber diameter on drag. Thus simulations with BTRA 501 insert geometry are planned.

In the future, reactive flow in ANSYS FLUENT can be utilized to get more realistic results for the influence of projectile geometry on thrust generation in the baffle tube. Because the combustion process significantly alters the base pressure profiles, only the corresponding nose cone and shoulder drags would be comparable to the inert gas simulations done here.

7. References

[1] Hertzberg, A., Bruckner, A. P., and Bogdanoff, D. W., “Ram Accelerator - a New Chemical Method for Accelerating Projectiles to Ultrahigh Velocities,” *AIAA Journal,* Vol. 26, No. 2, 1988, pp. 195–203. https://doi.org/10.2514/3.9872.

[2] Bruckner, A. P., “Operational Characteristics of the Thermally Choked Ram Accelerator’,” *Journal of Propulsion and Power,* Vol. 7, No. 5, 1991, pp. 828–836. https://doi.org/10.2514/3.23398.

[3] Hertzberg, A., Bruckner, A. P., and Knowlen, C., “Experimental Investigation of RAM Accelerator Propulsion Modes,” *Shock Waves,* Vol. 1, No. 1, 1991, pp. 17–25. https://doi.org/10.1007/bf01414864.

[4] Higgins, A. J., Knowlen, C., and Bruckner, A. P., “RAM Accelerator Operating Limits, Part 1: Identification of Limits’,” *Journal of Propulsion and Power,* Vol. 14, No. 6, 1998, pp. 951–958. https://doi.org/10.2514/2.5359.

[5] Ginos, J., “Influence_of_Projectile_Geometry_on_Baffled_Tube_Ram_Accelerators,” MSAA, University of Washington, 2023.

[6] Daneshvaran, N., “Transient Computational Fluid Dynamic Modeling of BTRA,” MSAA, University of Washington, 2017.

[7] Daneshvaran, N., and Knowlen, C., “Transient Computational Fluid Dynamic Modeling of Baffled Tube Ram Accelerator,” presented at the 55th AIAA Aerospace Sciences Meeting, Grapevine, Texas, 2017. https://doi.org/10.2514/6.2017-0119

[8] Correy, J. P., “Investigation of Baffled-Tube RAM Accelerator Configurations’,” *AIAA SCITECH*, 2023. https://doi.org/10.2514/6.2023-2186.

[9] Higgins, A. J., Knowlen, C., and Kiyanda, C. B., “Gasdynamic Operation of Baffled Tube Ram Accelerator in Highly Energetic Mixtures,” presented at the 20th International Colloquium on the Dynamics of Explosions and Reactive Systems, Montreal, Canada, 2005.

[10] Knowlen, C., Glusman, J., Grist, R., Bruckner, A., and Higgins, A., “Experimental Investigation of a Baffled-Tube Ram Accelerator,” presented at the 52nd AIAA/SAE/ASEE Joint Propulsion Conference, Salt Lake City, UT, 2016. https://doi.org/10.2514/6.2016-4813

[11] Imrich, T. S., “The Impact of Projectile Geometry on Ram Accelerator Performance,” MSAA, University of Washington, 1995.

[12] Knowlen, C., Higgins, A., Bruckner, A., and Bauer, P., “Ram Accelerator Operation in the Superdetonative Velocity Regime,” presented at the 34th Aerospace Sciences Meeting and Exhibit, Reno,NV,U.S.A., 1996. https://doi.org/10.2514/6.1996-98

[13] Mattingly, J. D., “Elements of Gas Turbine Propulsion,” American Institute of Aeronautics and Astronautics, Reston, Va, 2005.

[14] Cumpsty, N., and Heyes, A., “Jet Propulsion: A Simple Guide to the Aerodynamics and Thermodynamic Design and Performance of Jet Engines,” Cambridge University Press, 2015.

[15] Babu, V., “Fundamentals of Gas Dynamics,” John Wiley & Sons, 2015.

[16] Anderson, J. D., “Fundamentals of Aerodynamics,” McGraw-Hill Education, 2017.

[17] “Bluff Body Flows – Introduction to Aerospace Flight Vehicles.” https://eaglepubs.erau.edu/introductiontoaerospaceflightvehicles/chapter/bluff-body-flows/

[18] “Drag of a Sphere.” https://www1.grc.nasa.gov/beginners-guide-to-aeronautics/drag-of-a-sphere/

8. Appendix

8.1 Case results

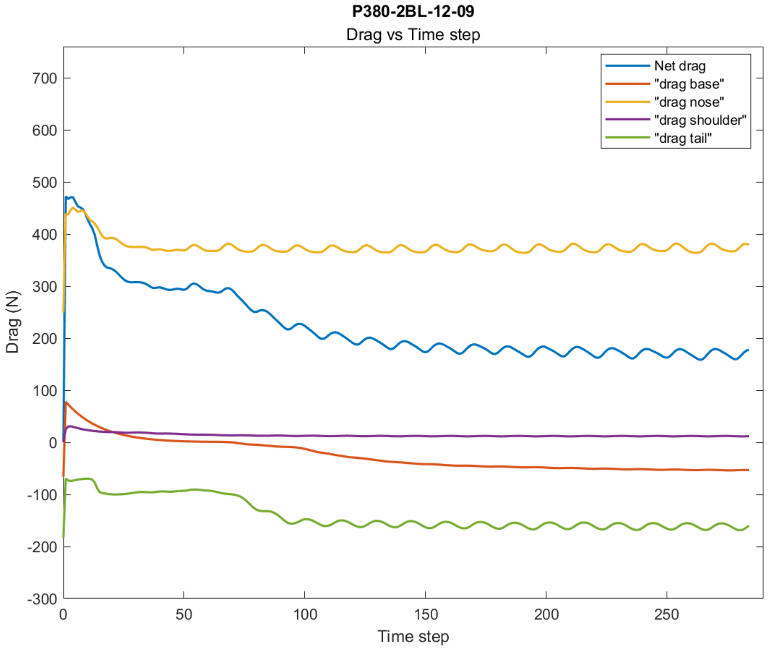

Figure 34. Drag components of P380-2BL-12-09 at 1000 m/s.

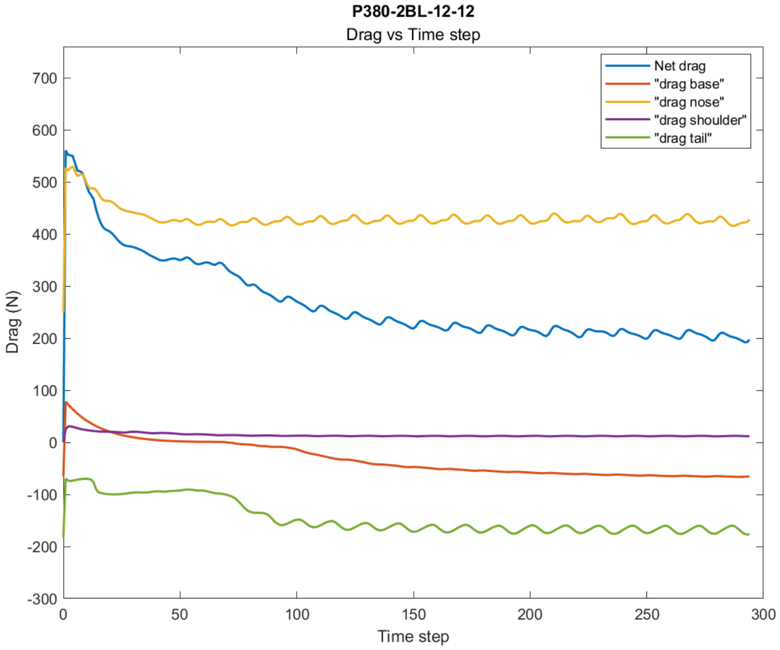

Figure 35. Drag components of P380-2BL-12-12 at 1000 m/s.

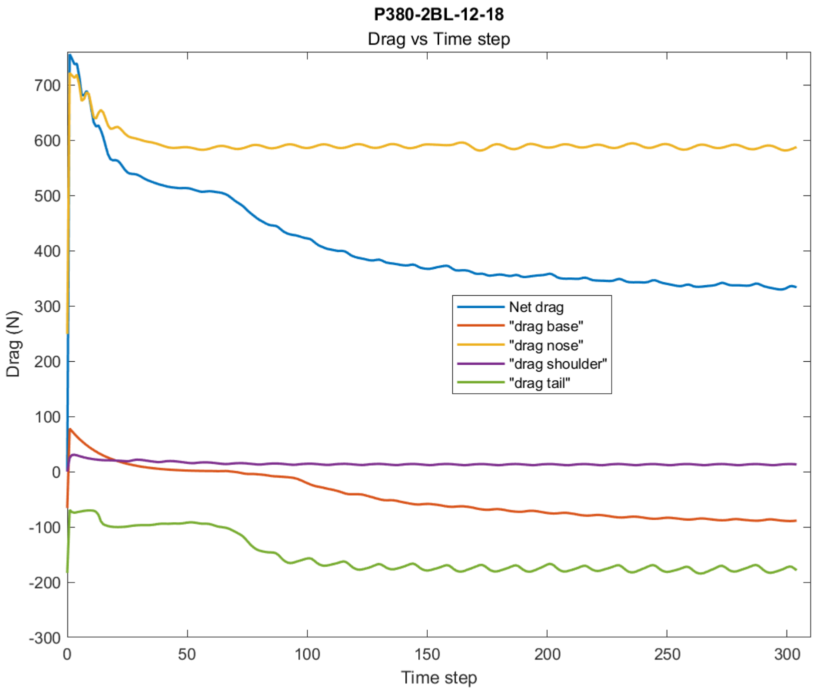

Figure 36. Drag components of P380-2BL-12-09 at 1000 m/s.

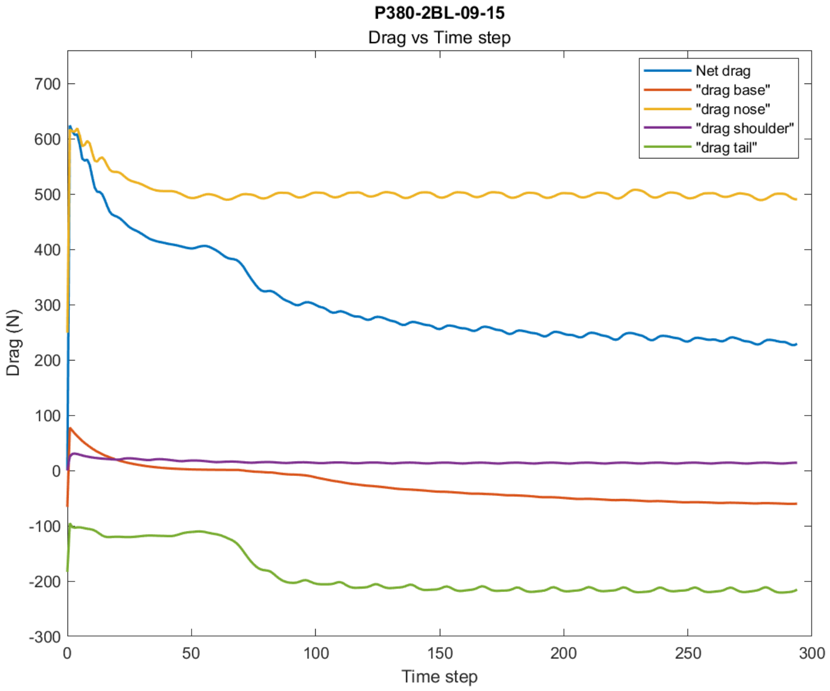

Figure 37. Drag components of P380-2BL-09-15 at 1000 m/s.

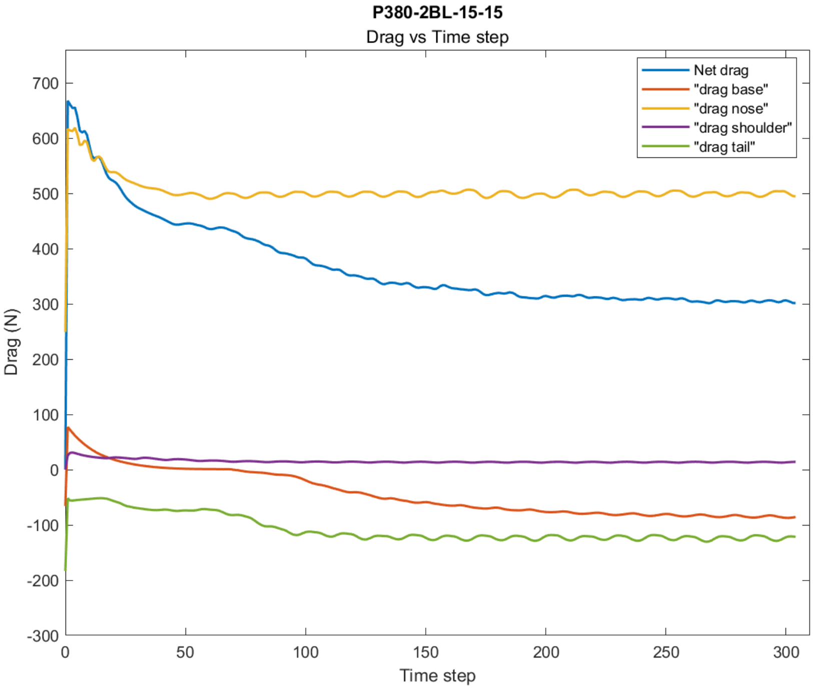

Figure 38. Drag components of P380-2BL-15-15 at 1000 m/s.

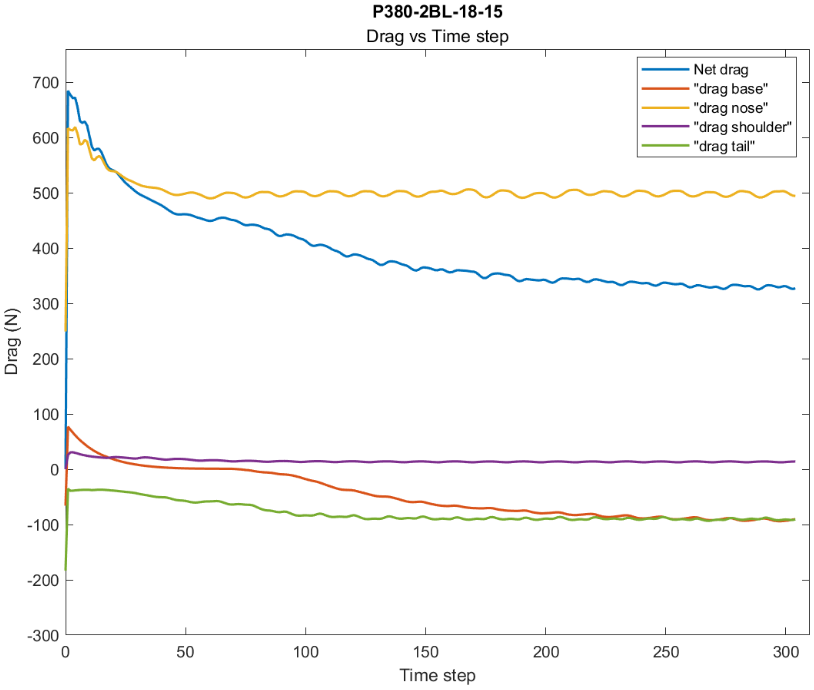

Figure 39. Drag components of P380-2BL-18-15 at 1000 m/s.

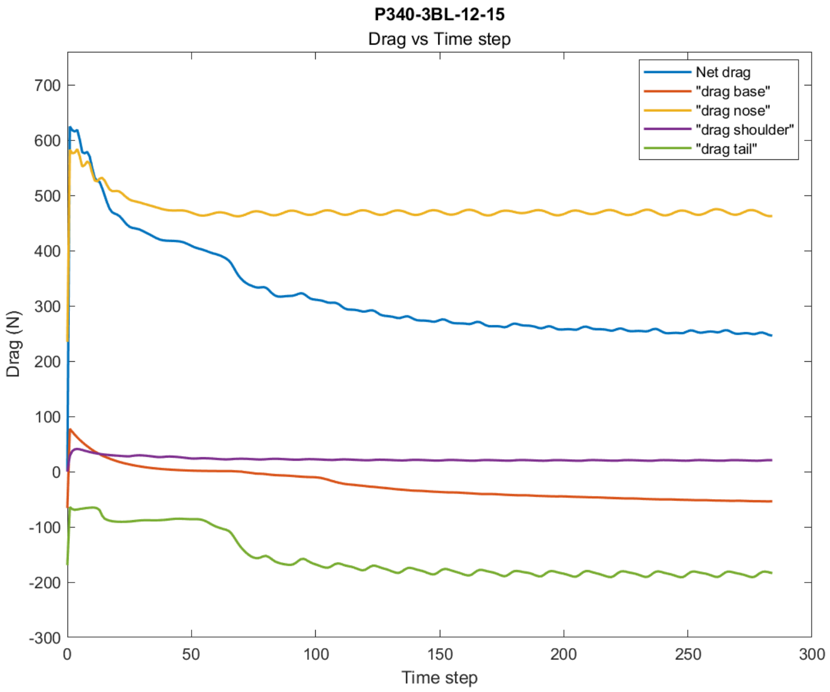

Figure 40. Drag components of P340-3BL-12-15 at 1000 m/s.

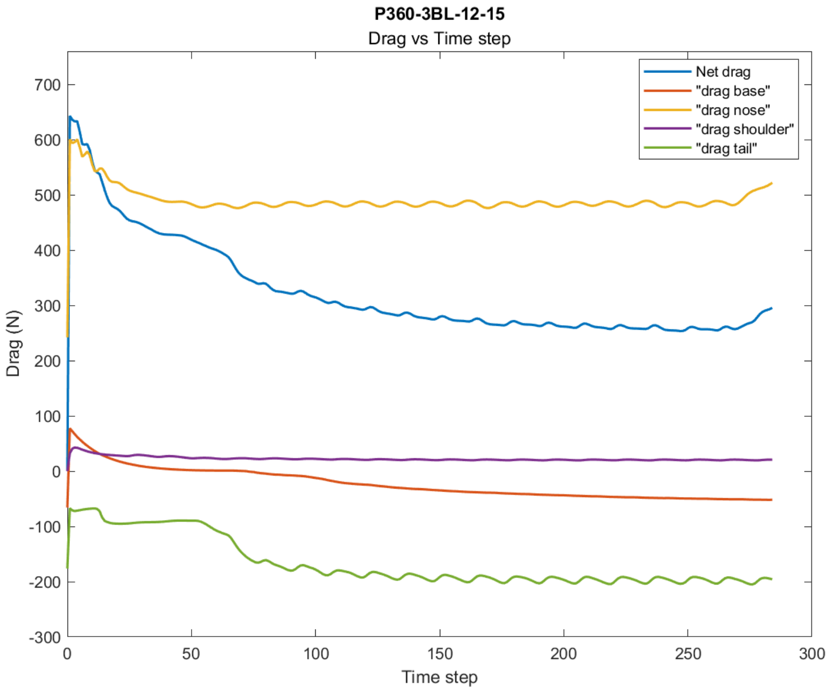

Figure 41. Drag components of P360-3BL-12-15 at 1000 m/s.

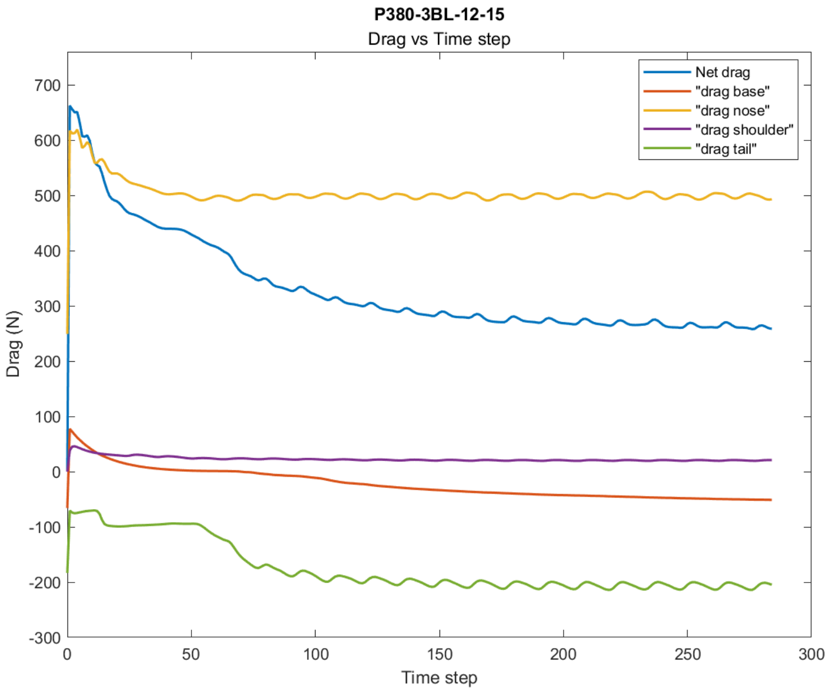

Figure 42. Drag components of P380-3BL-12-15 at 1000 m/s.

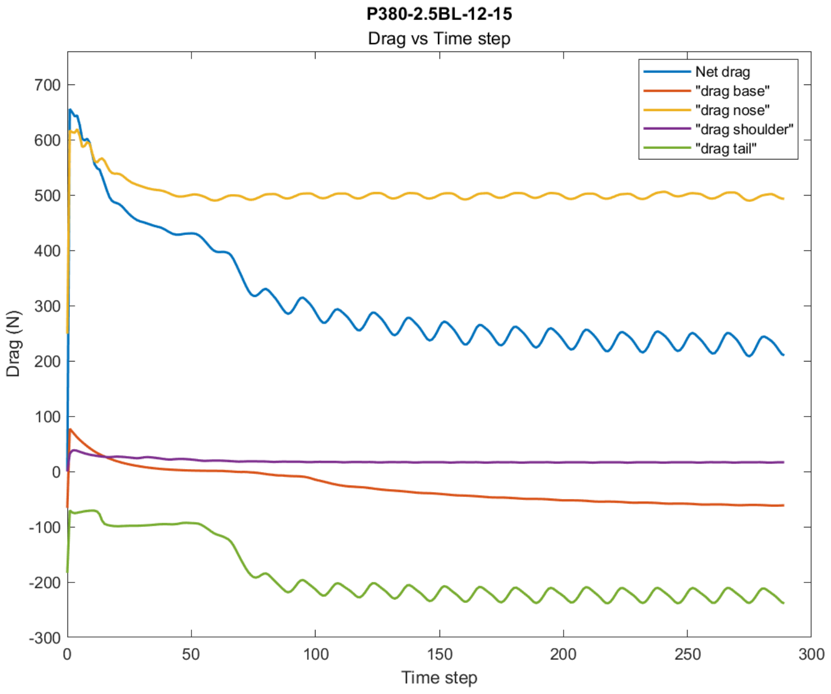

Figure 43. Drag components of P380-2.5BL-12-15 at 1000 m/s.

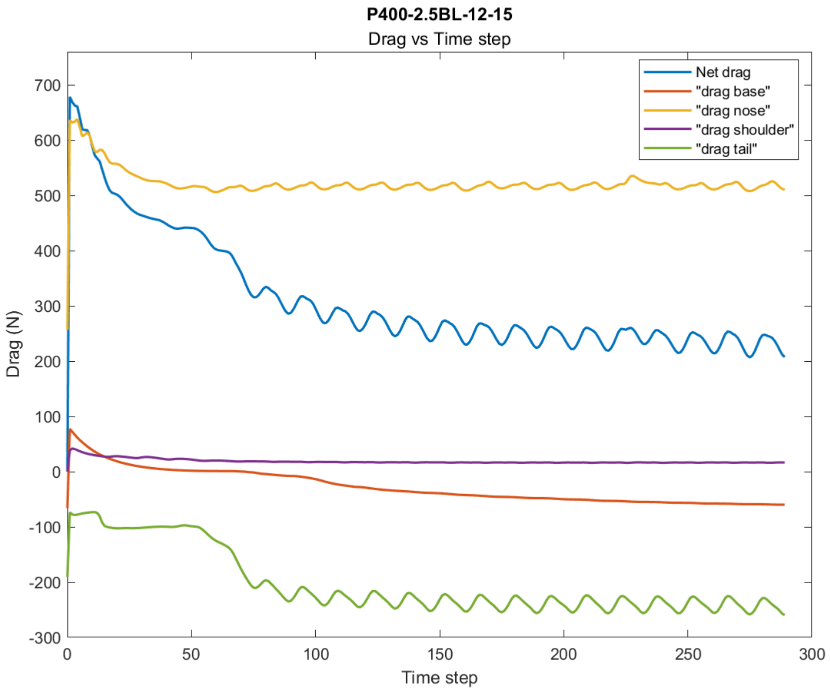

Figure 44. Drag components of P400-2.5BL-12-15 at 1000 m/s.

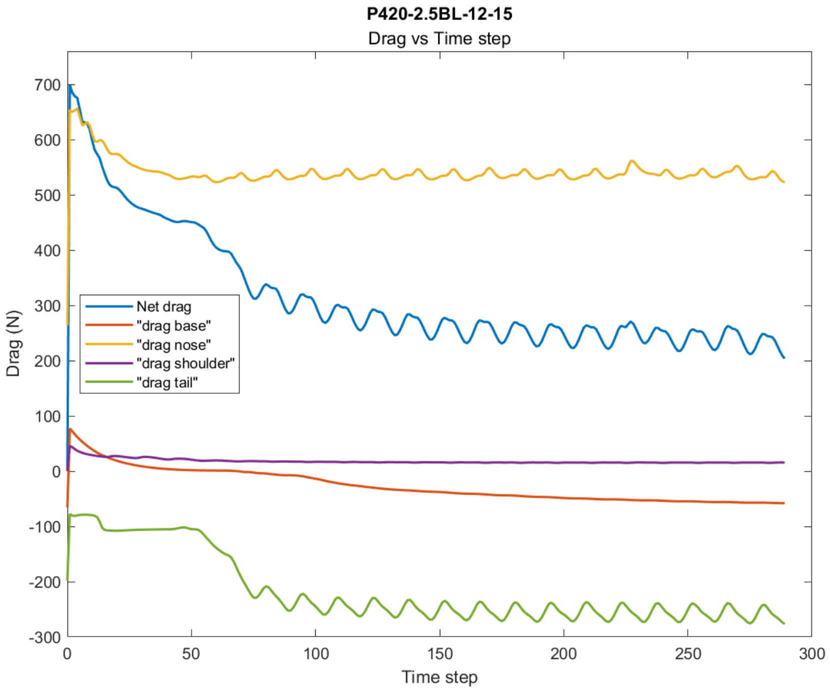

Figure 45. Drag components of P420-2.5BL-12-15 at 1000 m/s.

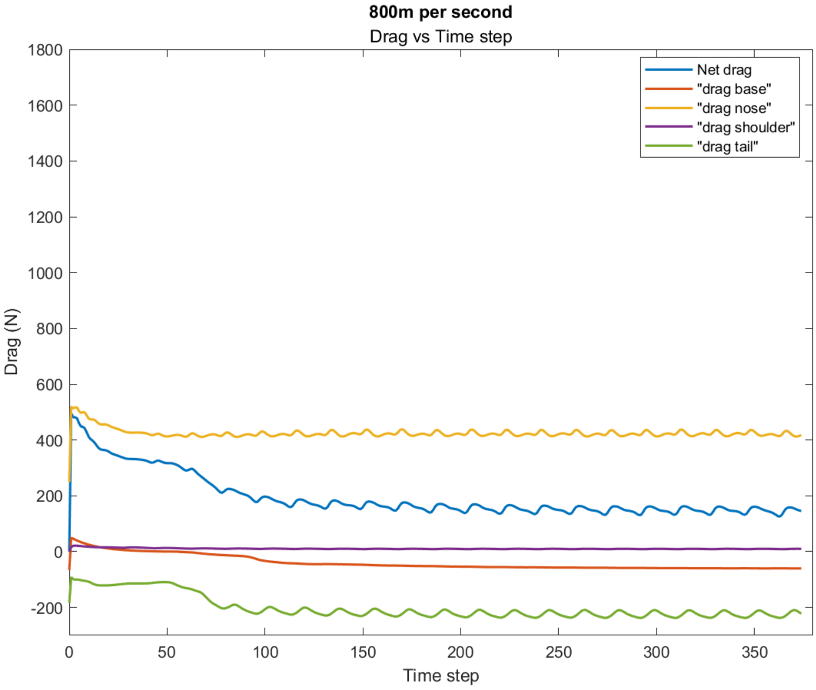

Figure 46. Drag components of P380-2BL-12-15 at 800 m/s.

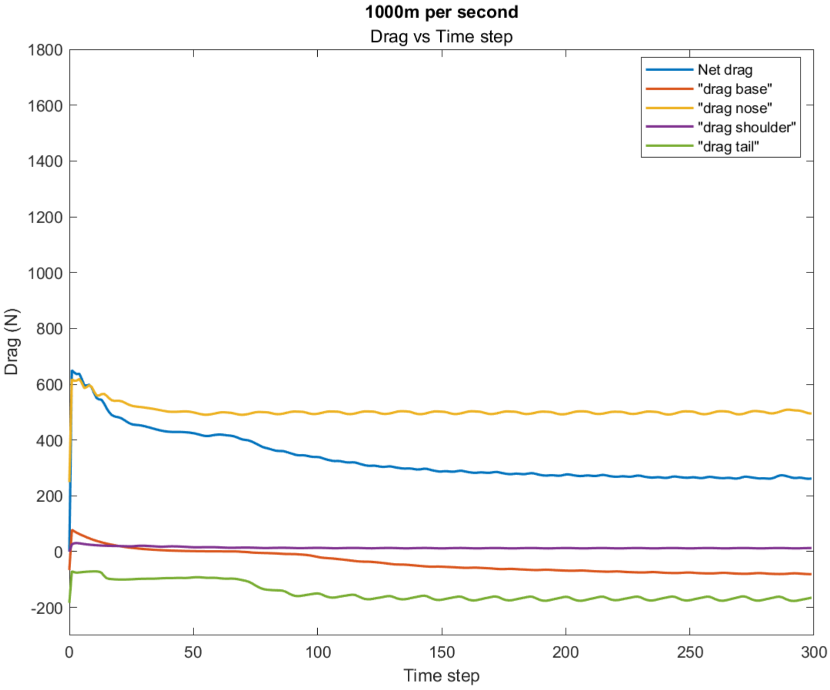

Figure 47. Drag components of P380-2BL-12-15 at 1000 m/s.

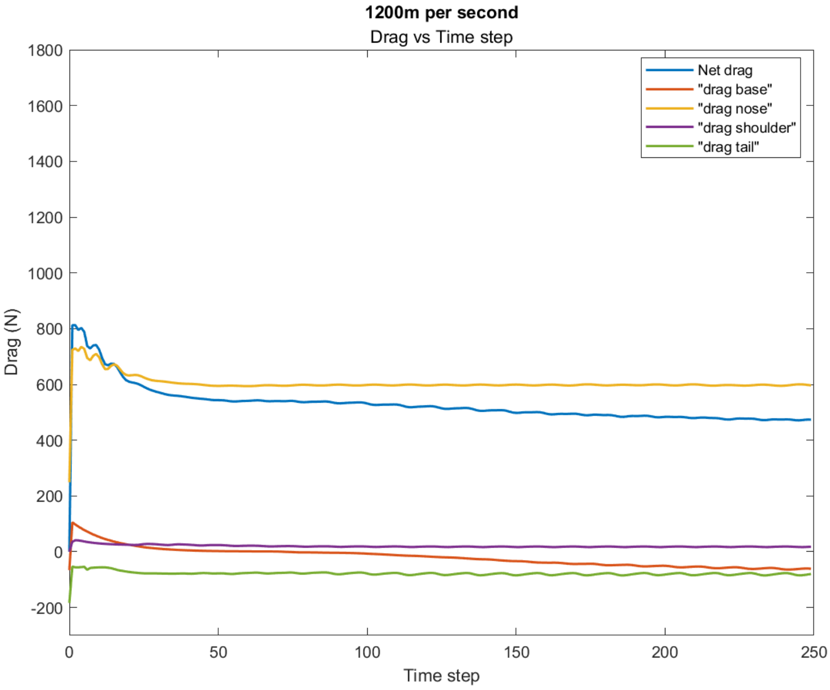

Figure 48. Drag components of P380-2BL-12-15 at 1200 m/s.

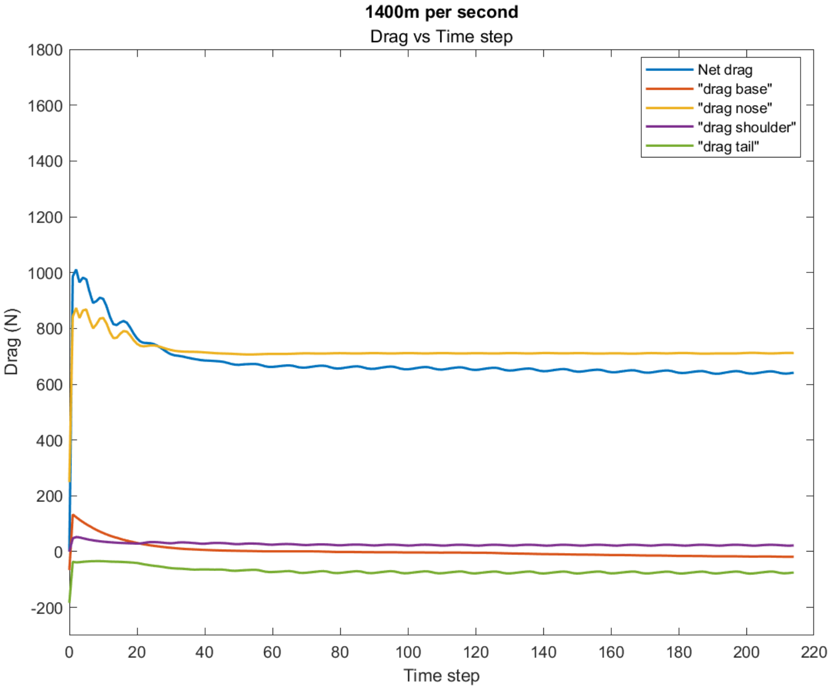

Figure 49. Drag components of P380-2BL-12-15 at 1400 m/s.

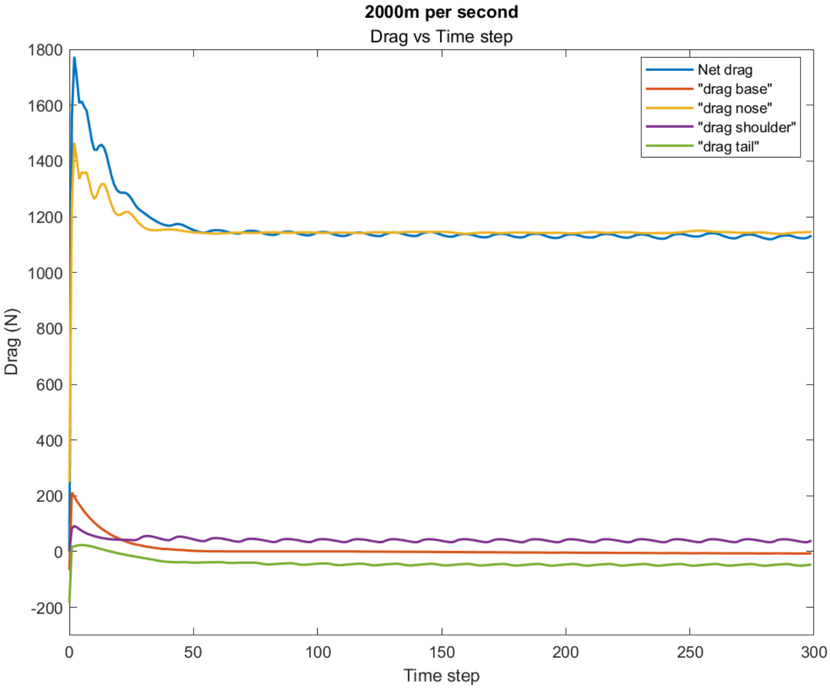

Figure 50. Drag components of P380-2BL-12-15 at 2000 m/s.

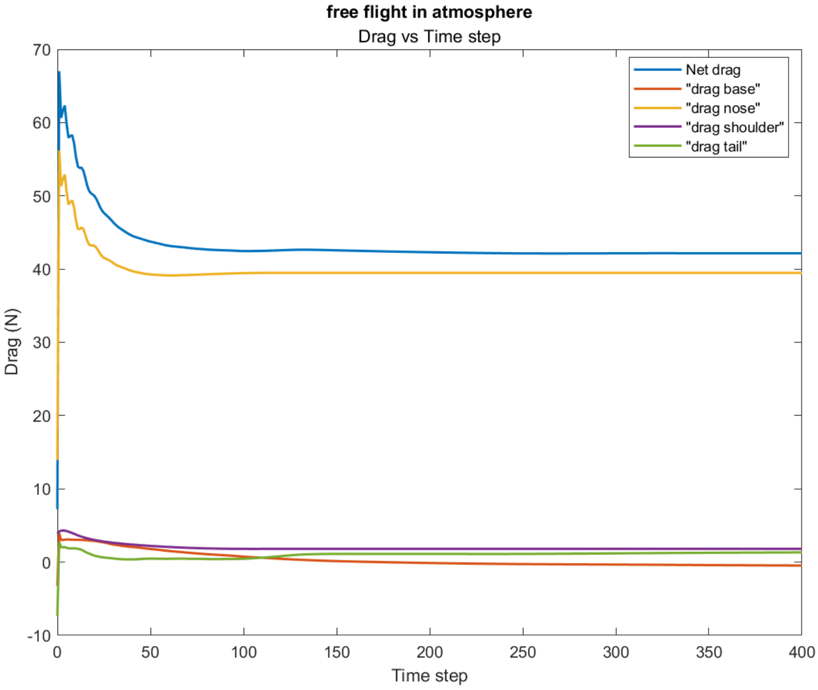

Figure 51. Drag components of P380-2BL-12-15 in free flight in atmosphere at 1000 m/s.

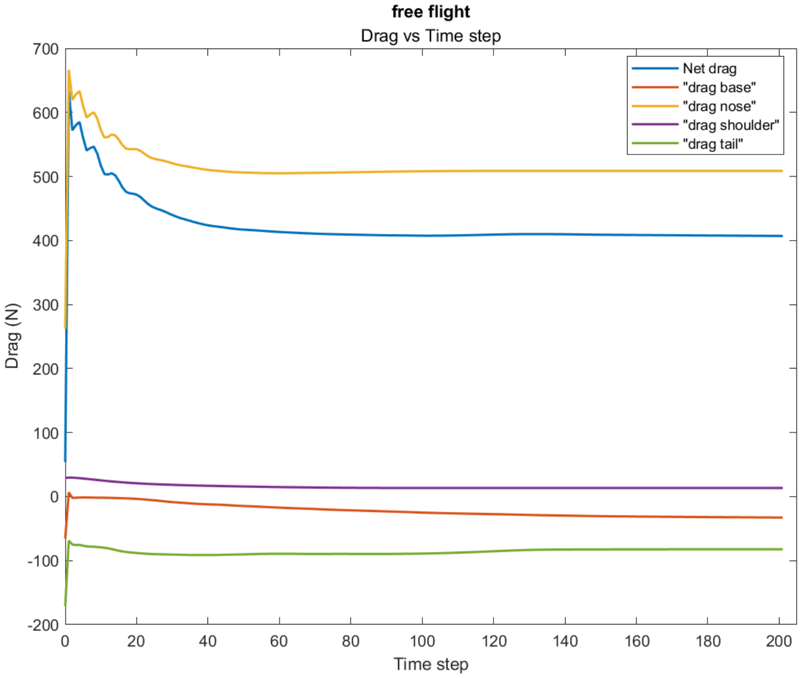

Figure 52. Drag components of P380-2BL-12-15 in free flight in methane-air at 300 psi at 1000 m/s.

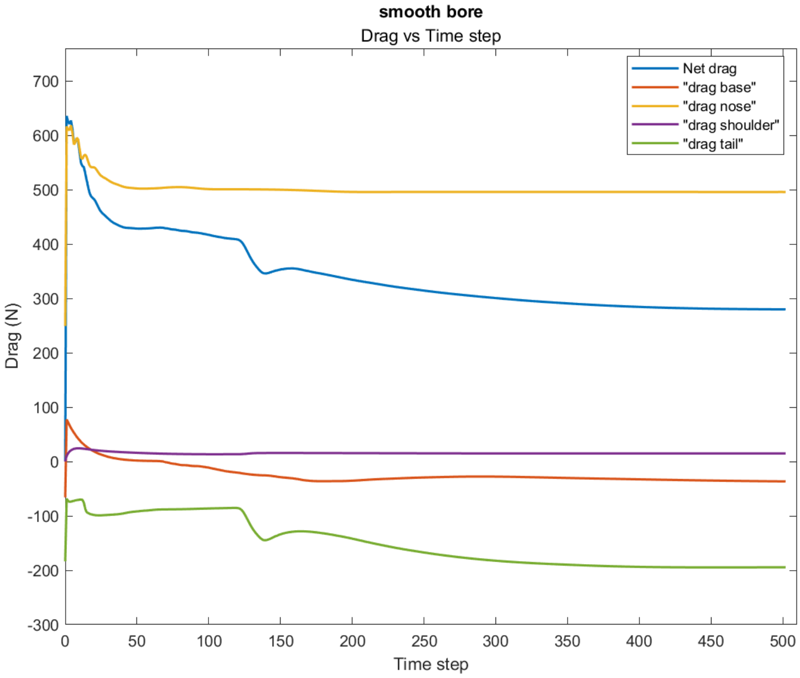

Figure 53. Drag components of P380-2BL-12-15 in smooth bore (tube without baffles) at 1000 m/s.

8.2 Projectile Flow Visualization

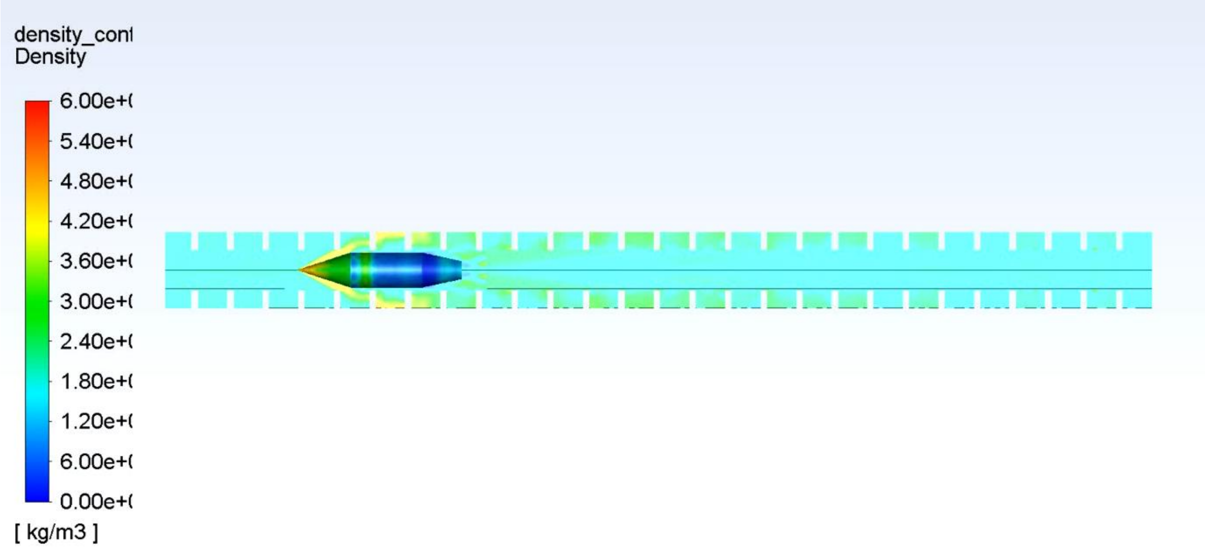

Figure 54. Density contour of P380-2BL-12-18 at 1000 m/s.

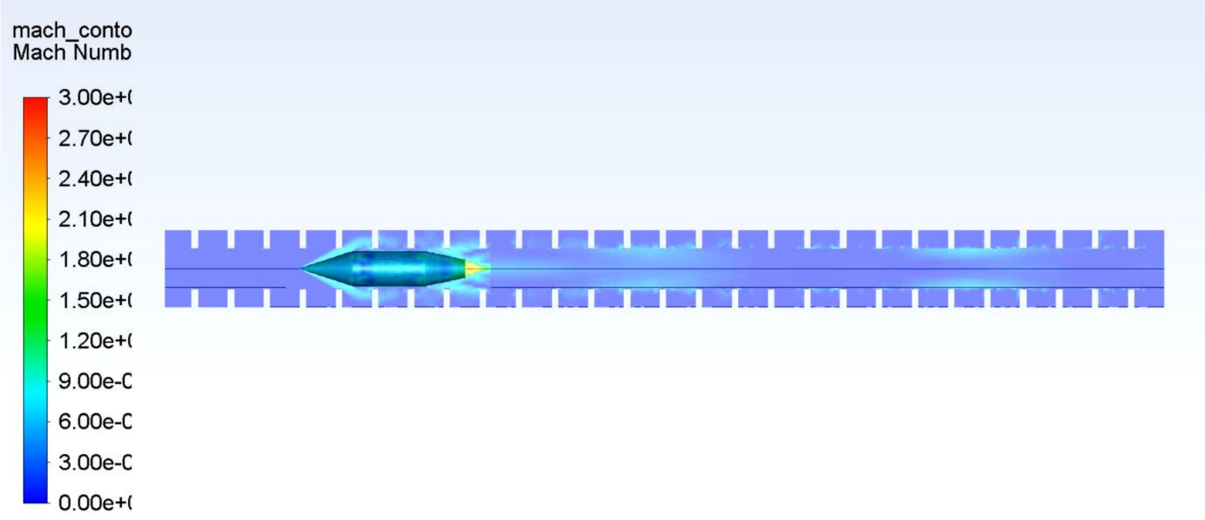

Figure 55. Mach contour of P380-2BL-12-18 at 1000 m/s.

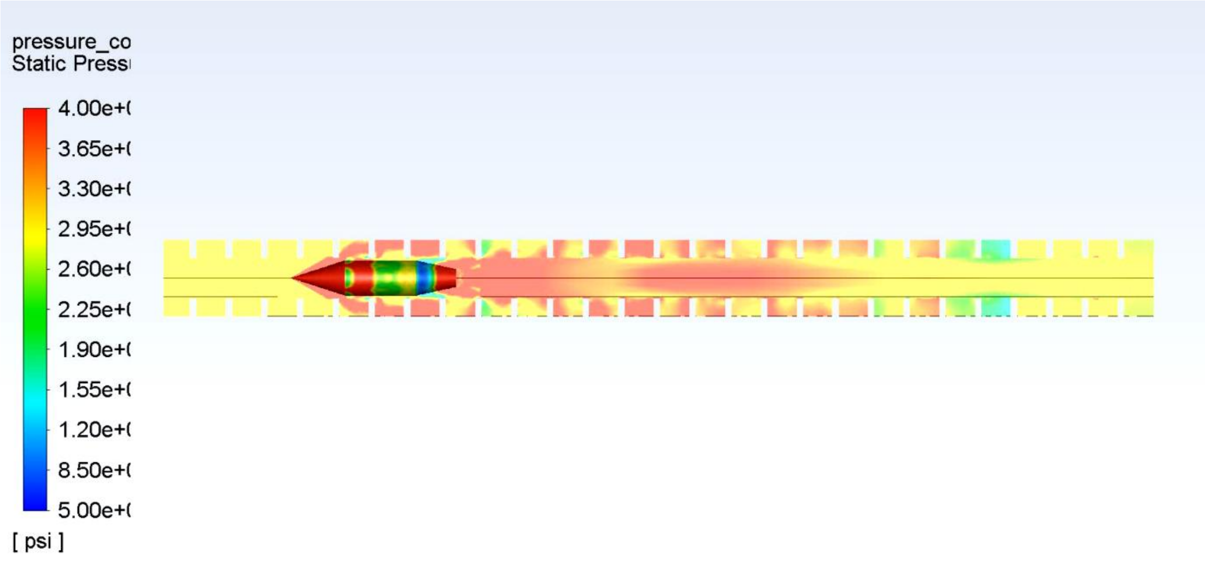

Figure 56. Pressure contour of P380-2BL-12-18 at 1000 m/s.

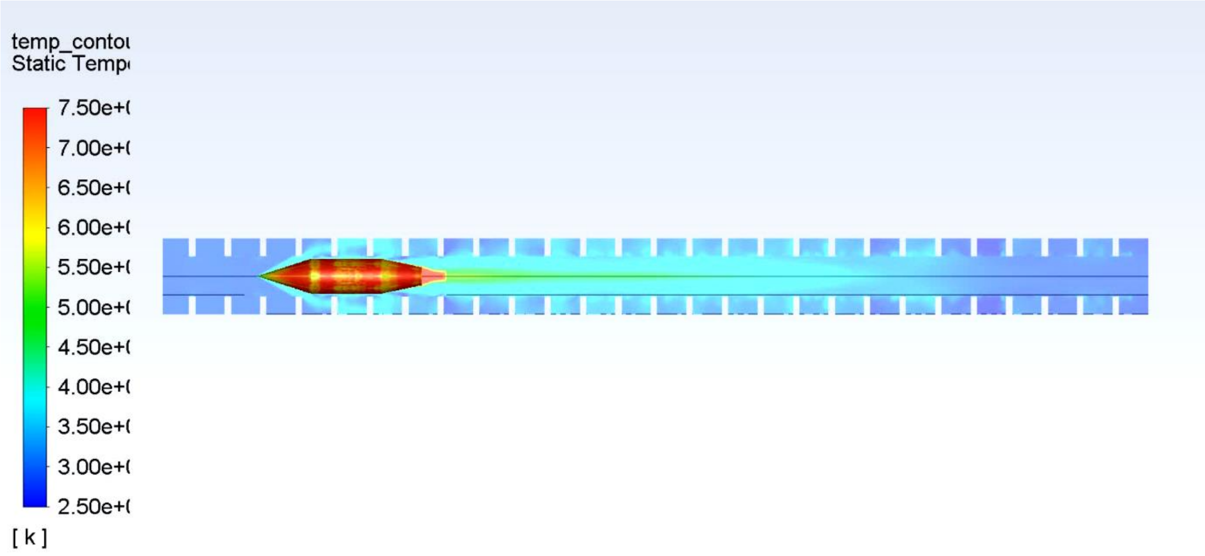

Figure 57. Temperature contour of P380-2BL-12-18 at 1000 m/s.

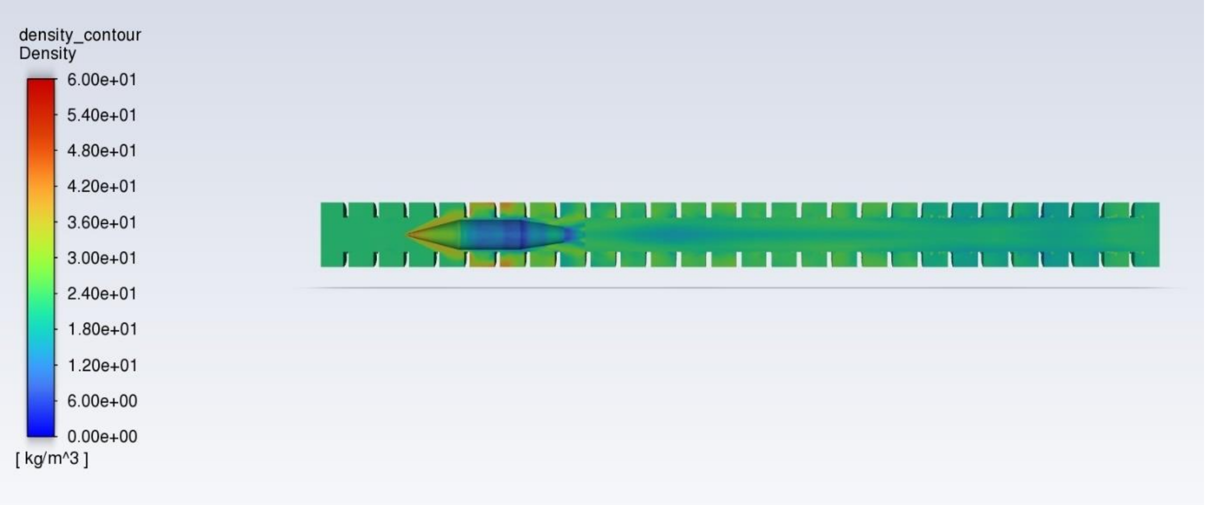

Figure 58. Density contour of P380-2BL-09-15 at 1000 m/s.

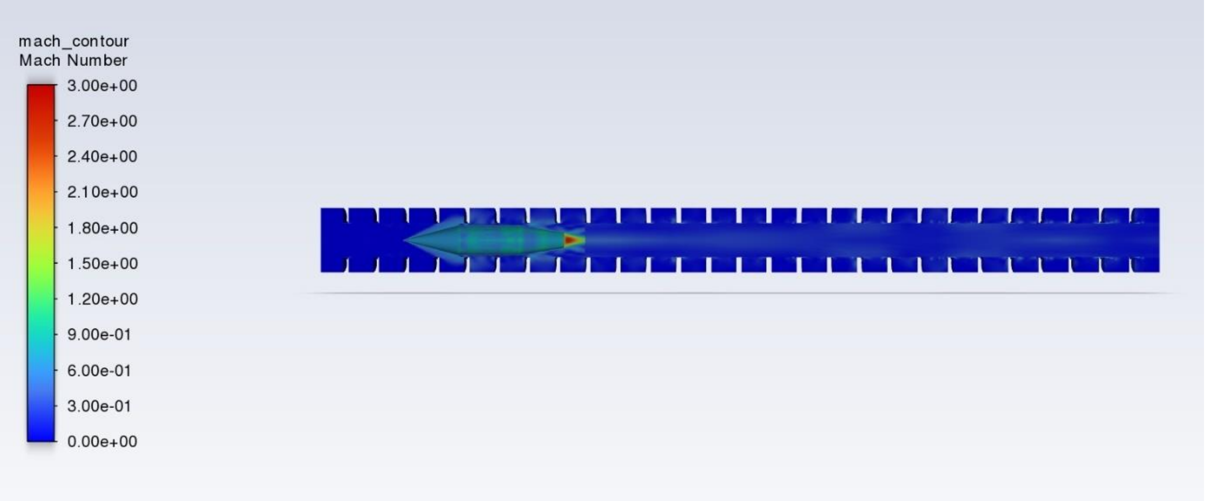

Figure 59. Mach contour of P380-2BL-09-15 at 1000 m/s.

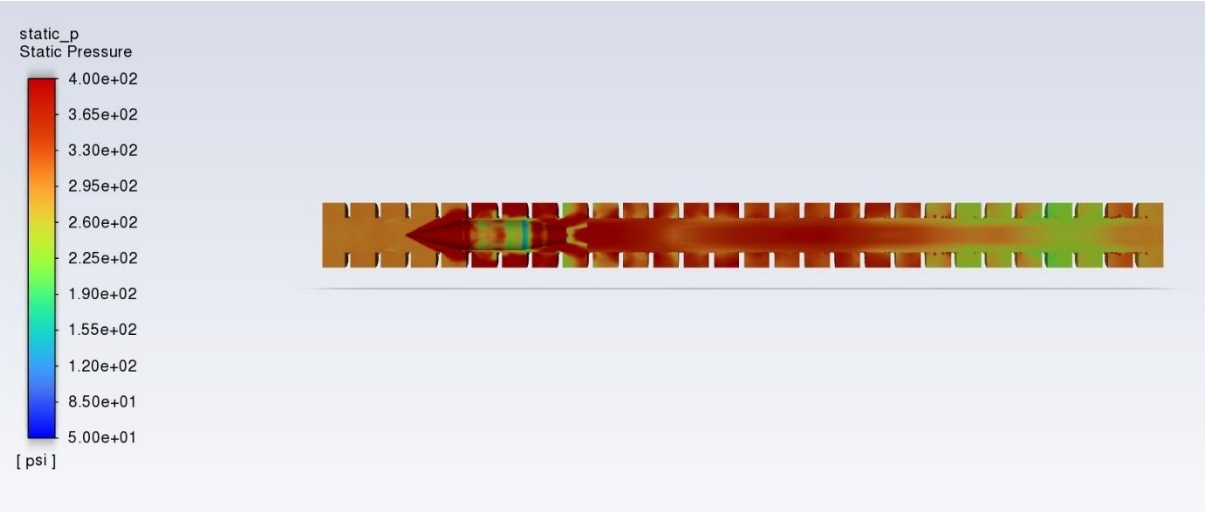

Figure 60. Pressure contour of P380-2BL-09-15 at 1000 m/s.

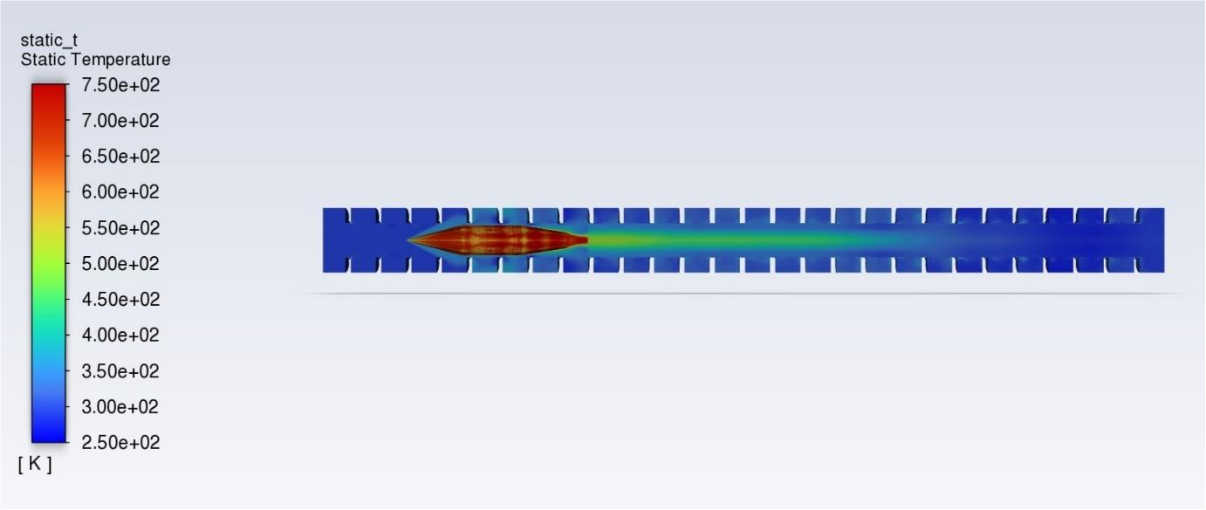

Figure 61. Temperature contour of P380-2BL-09-15 at 1000 m/s.

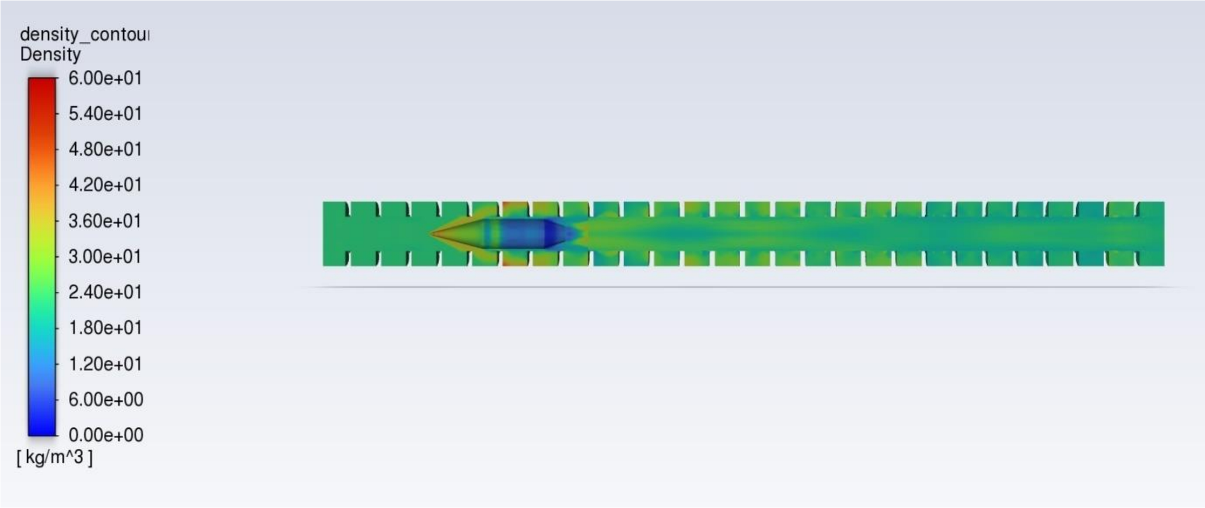

Figure 62. Density contour of P380-2BL-18-15 at 1000 m/s.

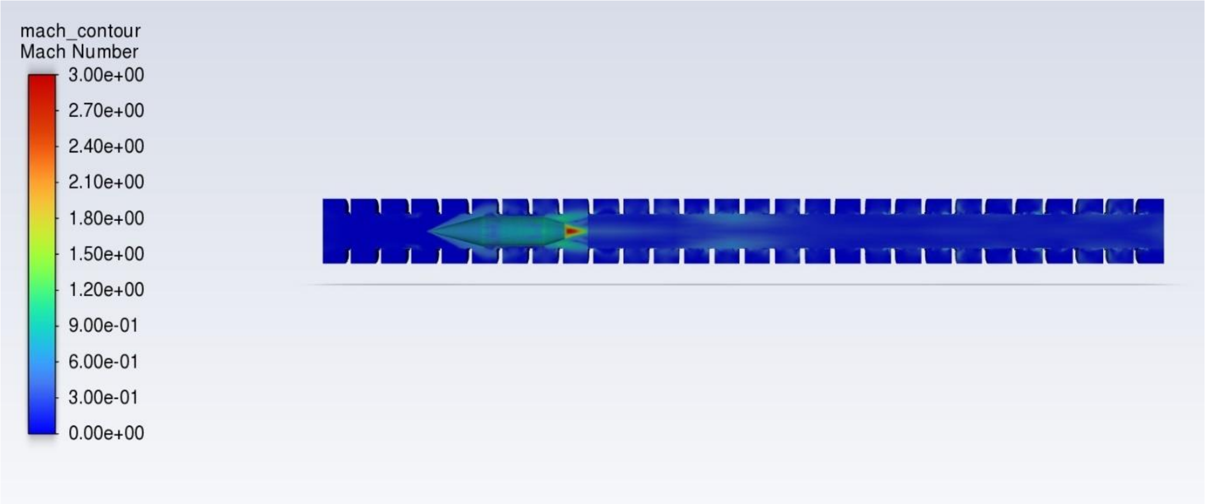

Figure 63. Mach contour of P380-2BL-18-15 at 1000 m/s.

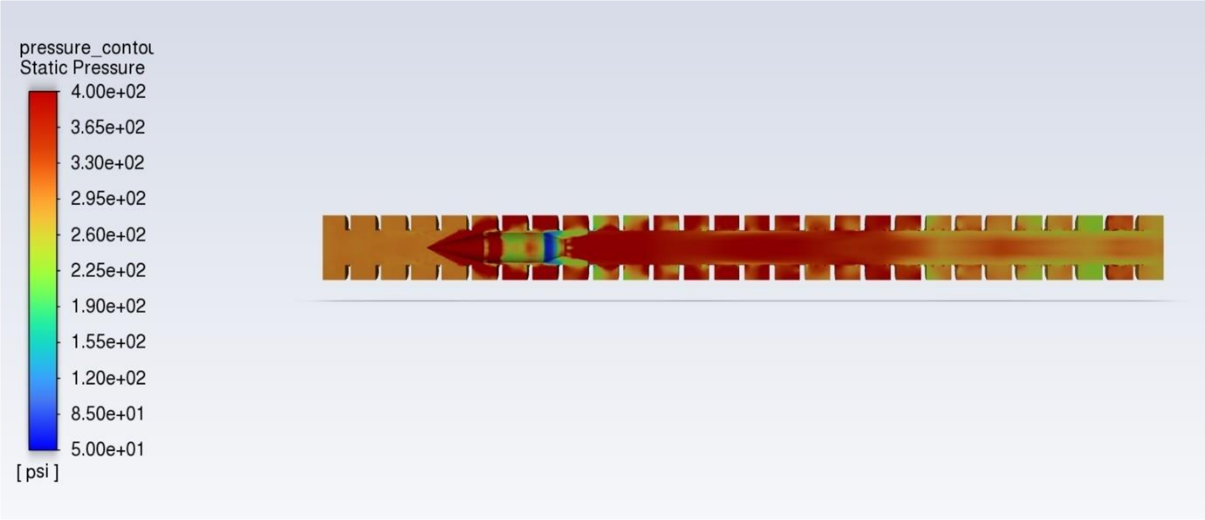

Figure 64. Temperature contour of P380-2BL-18-15 at 1000 m/s.

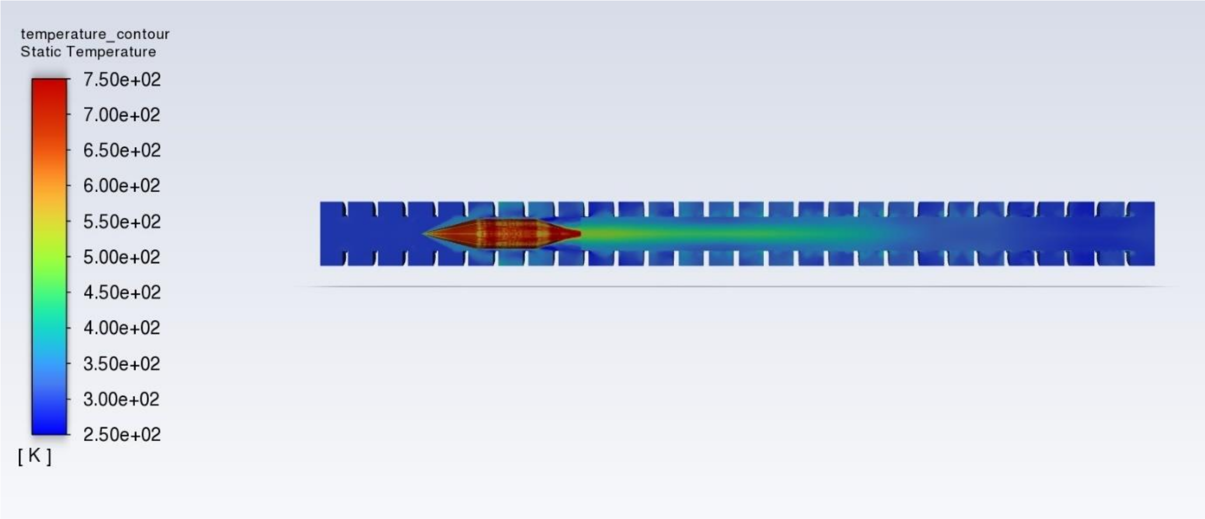

Figure 65. Temperature contour of P380-2BL-18-15 at 1000 m/s.

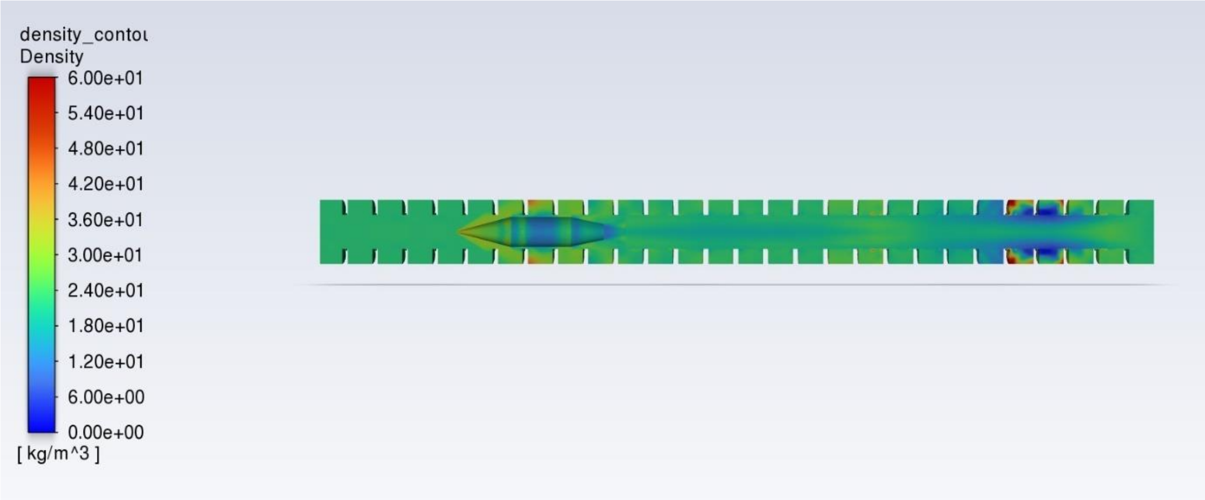

Figure 66. Density contour of P380-2BL-12-15 at 800 m/s.

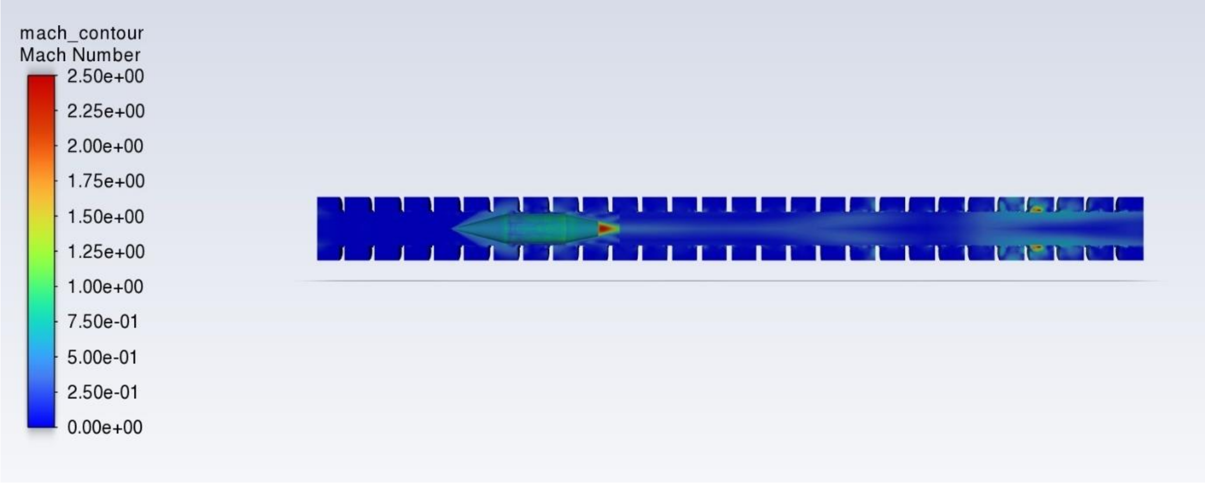

Figure 67. Mach contour of P380-2BL-12-15 at 800 m/s.

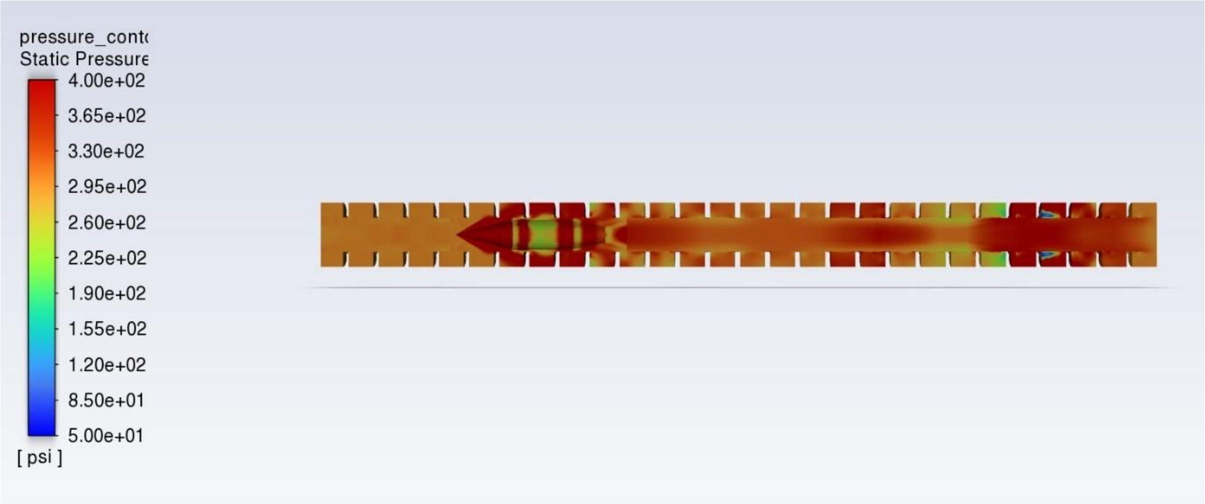

Figure 68. Pressure contour of P380-2BL-12-15 at 800 m/s.

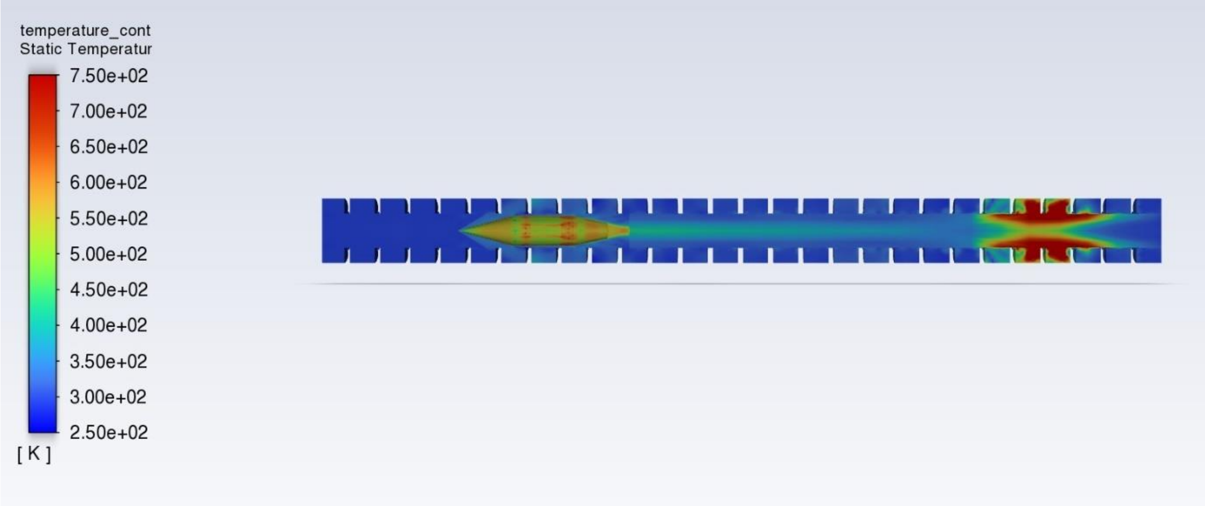

Figure 69. Temperature contour of P380-2BL-12-15 at 800 m/s.

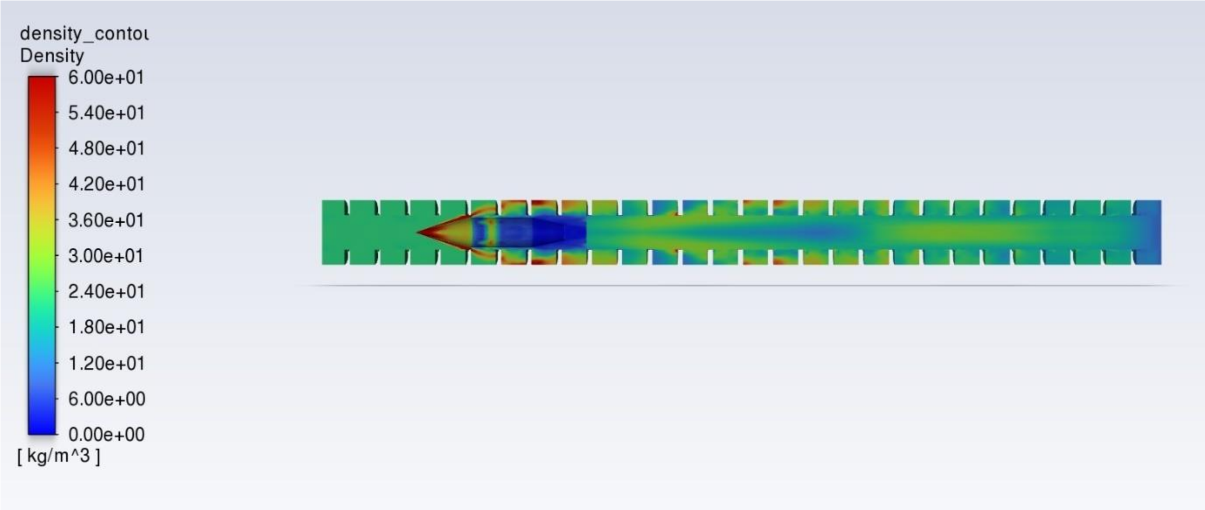

Figure 70. Density contour of P380-2BL-12-15 at 2000 m/s.

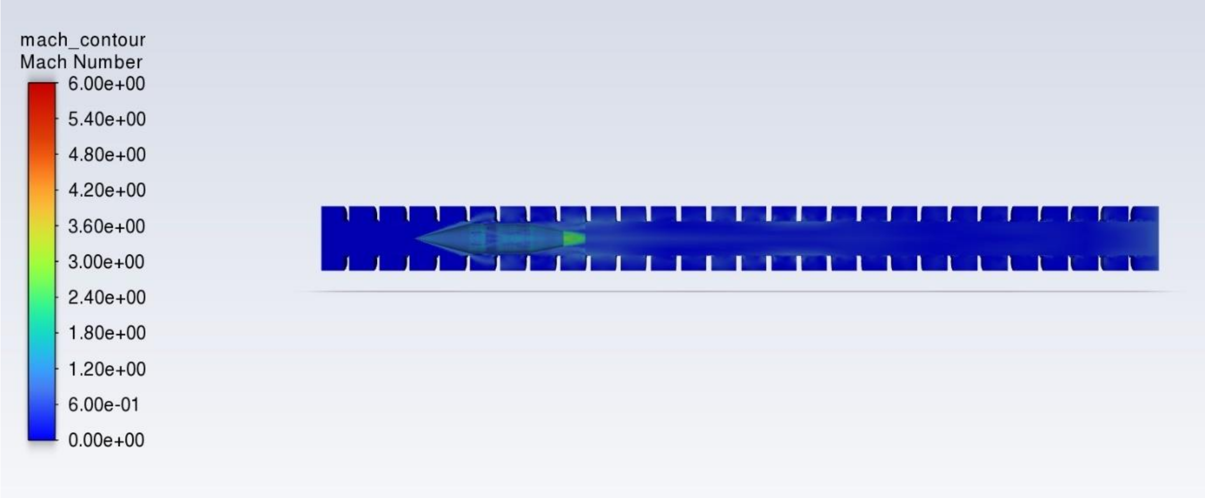

Figure 71. Temperature contour of P380-2BL-12-15 at 2000 m/s.

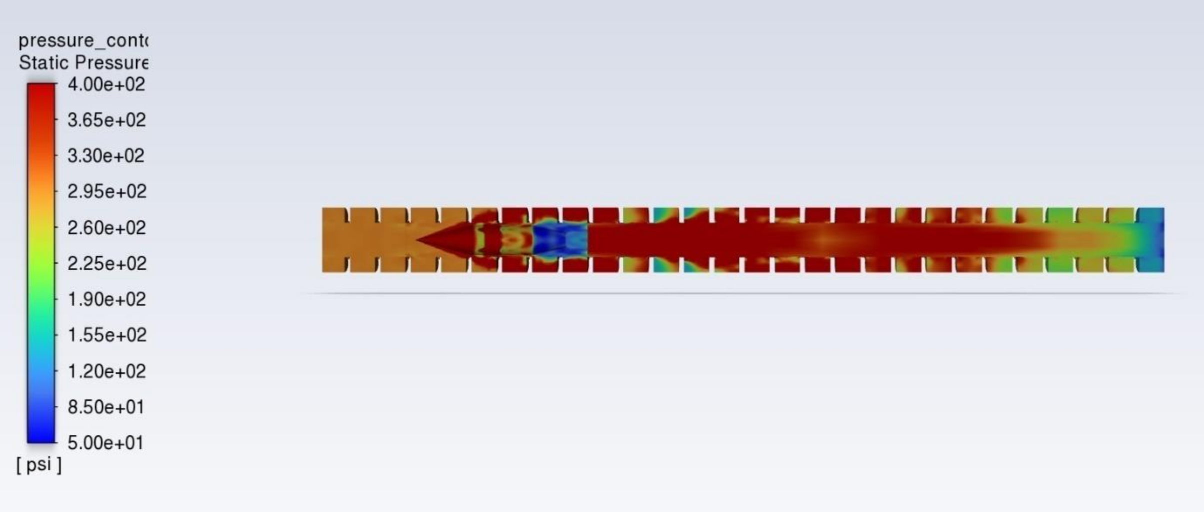

Figure 72. Pressure contour of P380-2BL-12-15 at 2000 m/s.

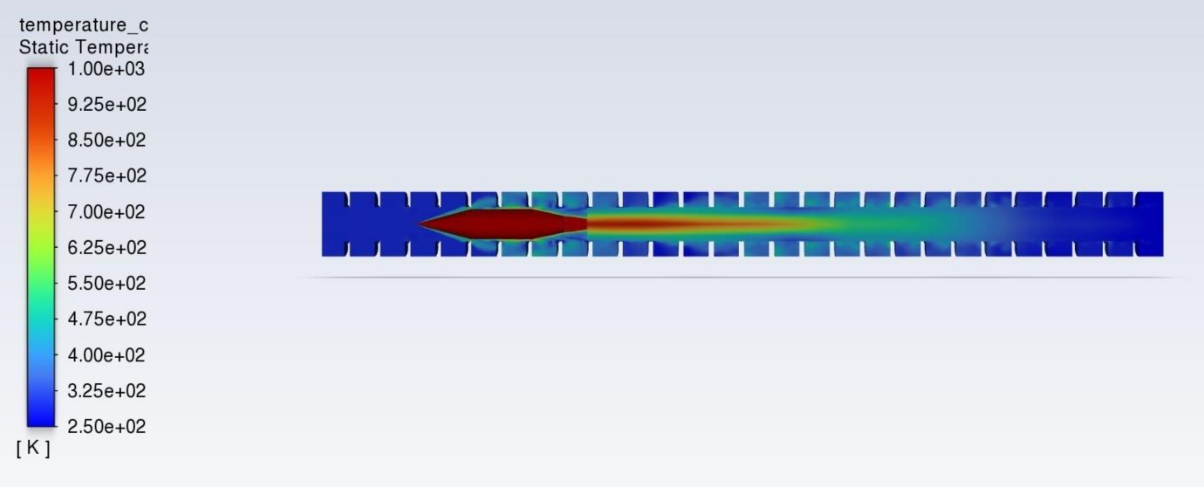

Figure 73. Temperature contour of P380-2BL-12-15 at 2000 m/s.

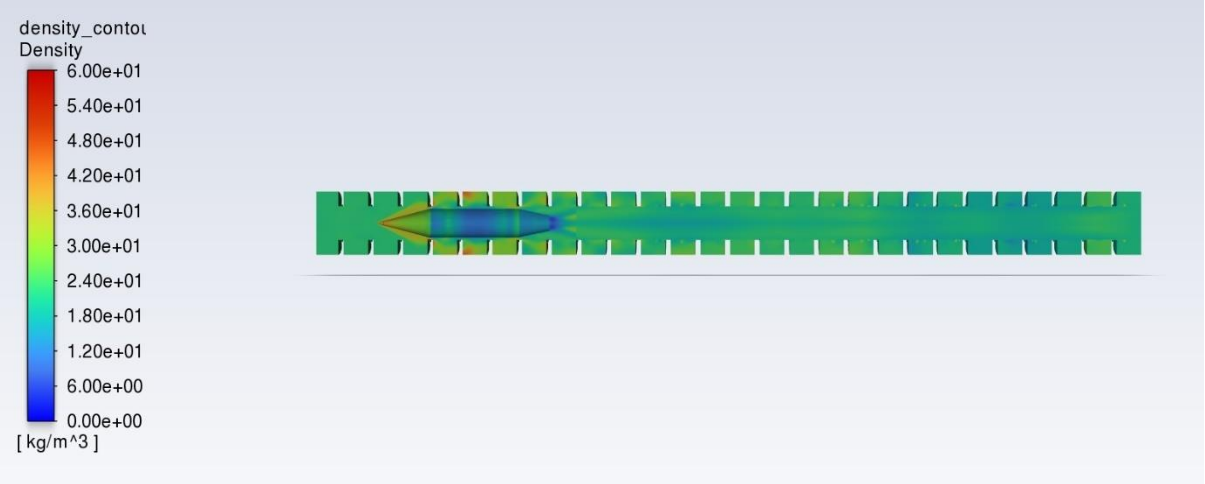

Figure 74. Density contour of P340-3BL-12-15 at 1000 m/s.

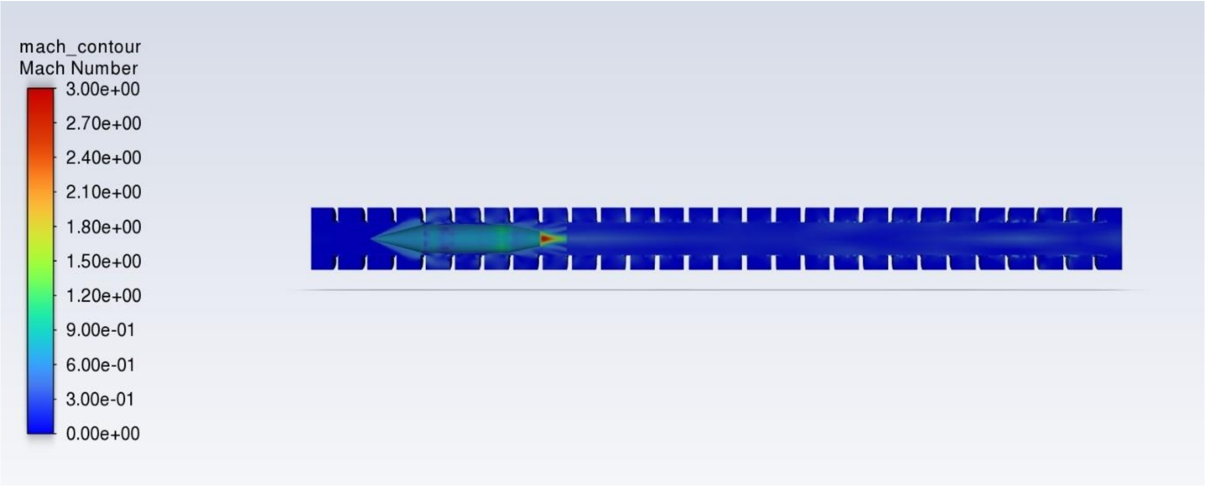

Figure 75. Mach contour of P340-3BL-12-15 at 1000 m/s.

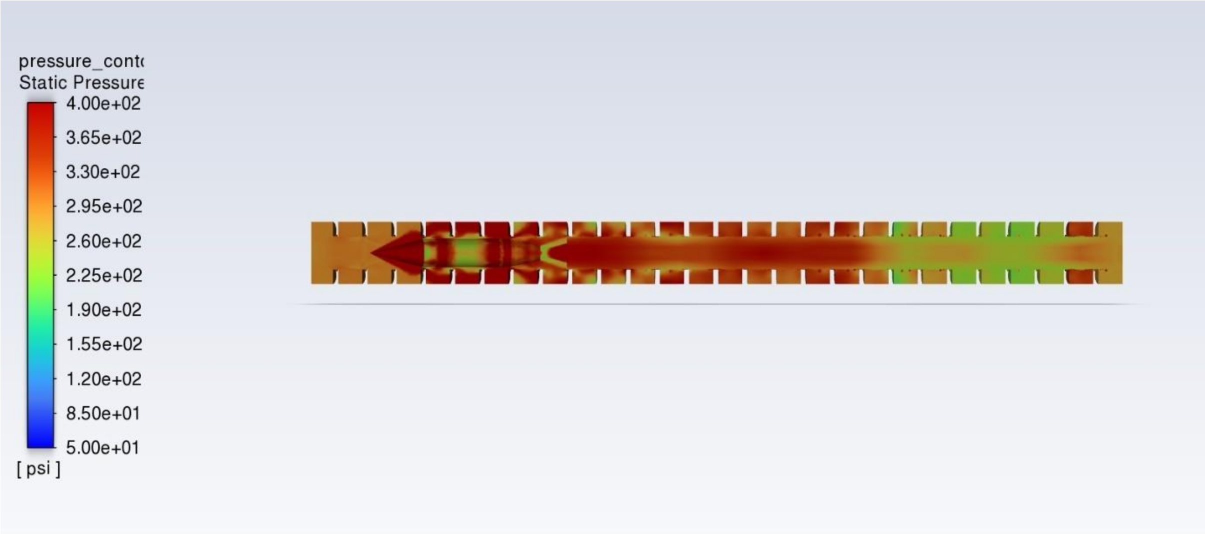

Figure 76. Pressure contour of P340-3BL-12-15 at 1000 m/s.

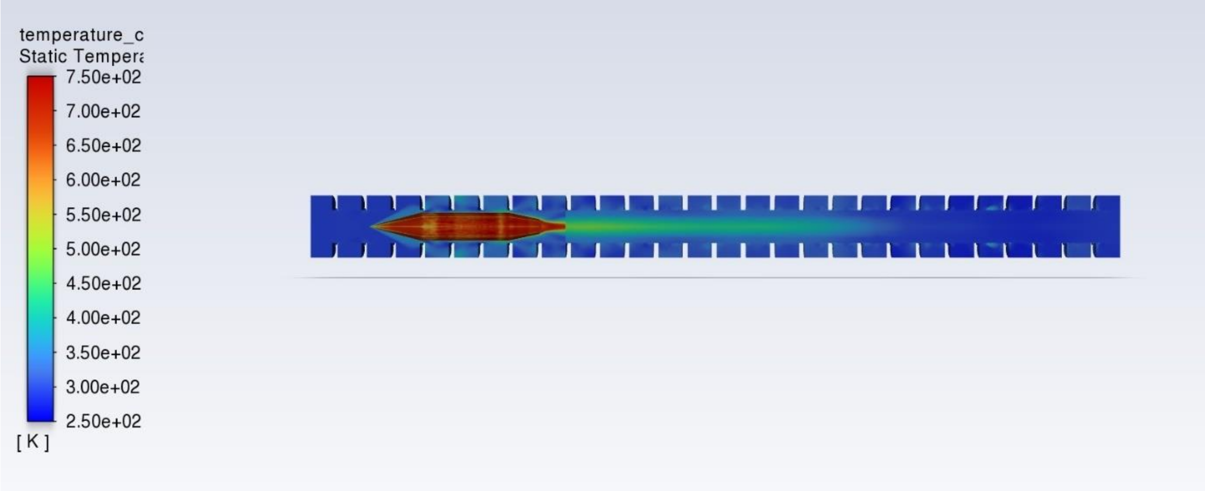

Figure 77. Temperature contour of P340-3BL-12-15 at 1000 m/s.

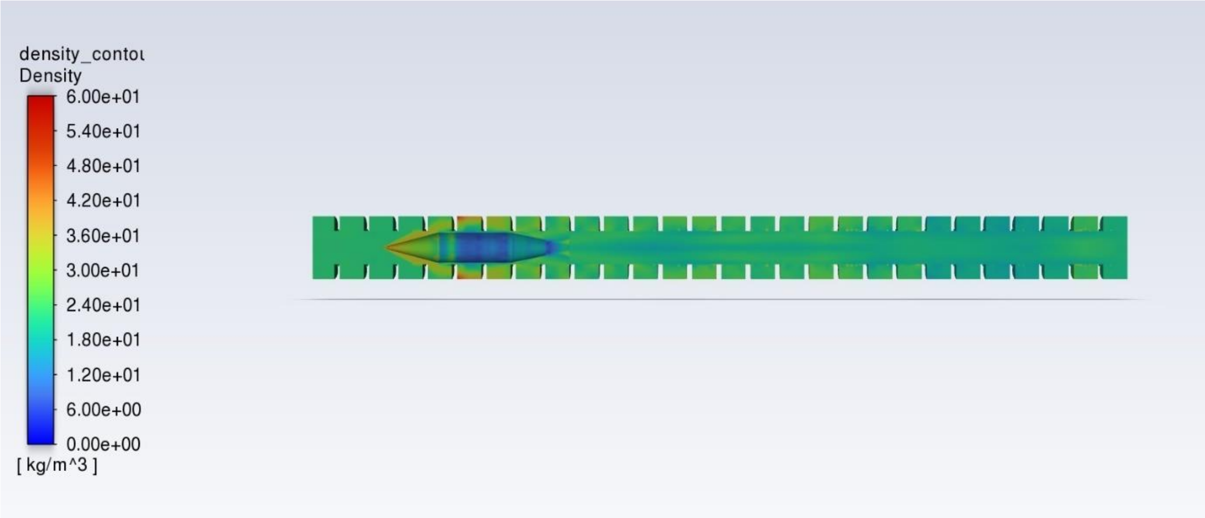

Figure 78. Density contour of P420-2.5BL-12-15 at 1000 m/s.

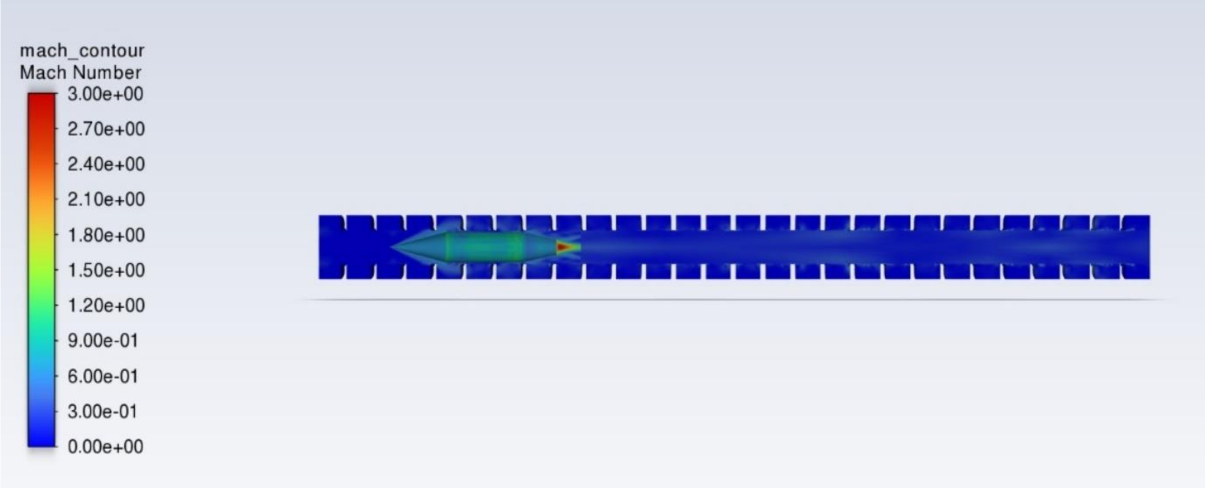

Figure 79. Mach contour of P420-2.5BL-12-15 at 1000 m/s.

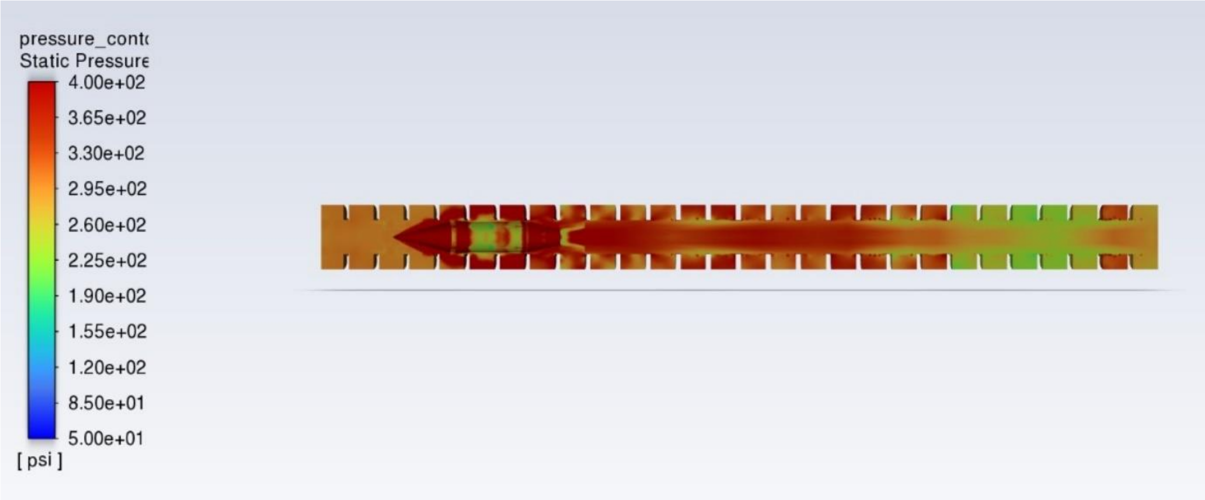

Figure 80. Pressure contour of P420-2.5BL-12-15 at 1000 m/s.

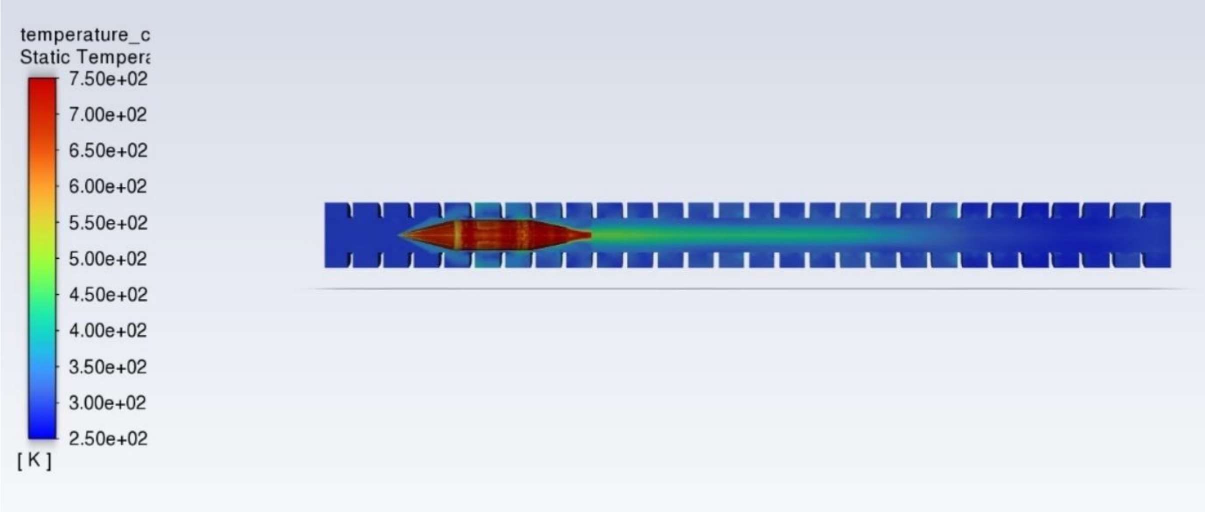

Figure 81. Temperature contour of P420-2.5BL-12-15 at 1000 m/s.

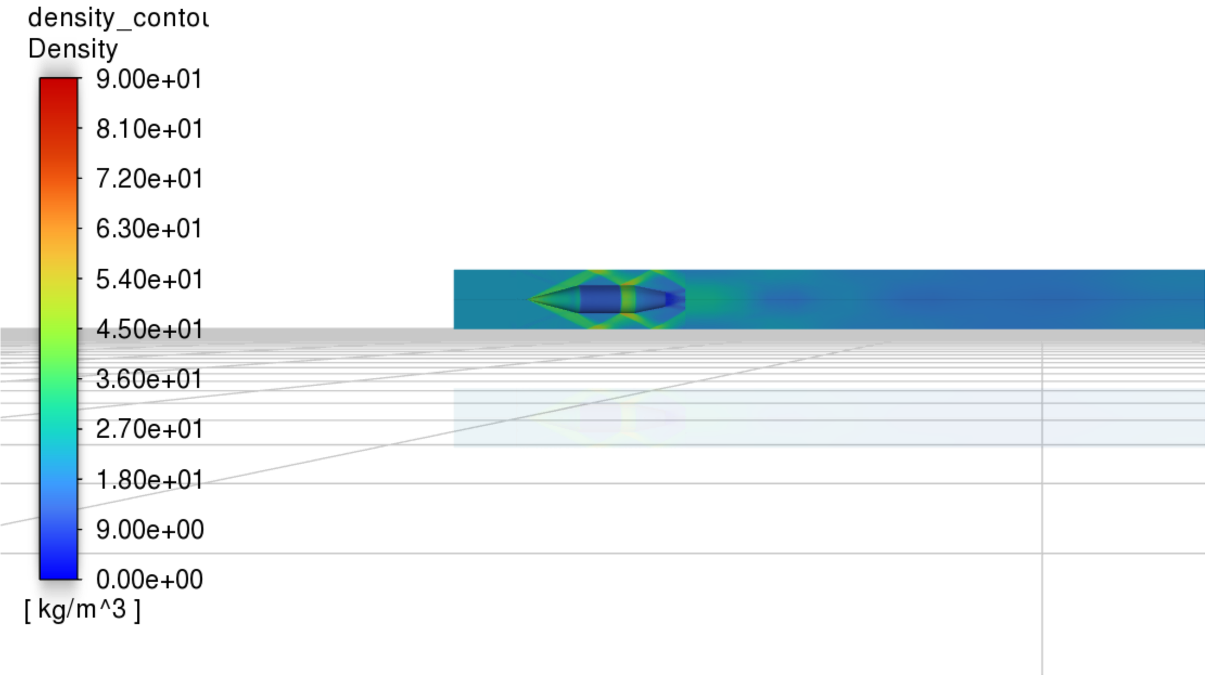

Figure 82. Density contour of P380-2BL-12-15 in smooth bore (tube without baffles) at 1000 m/s.

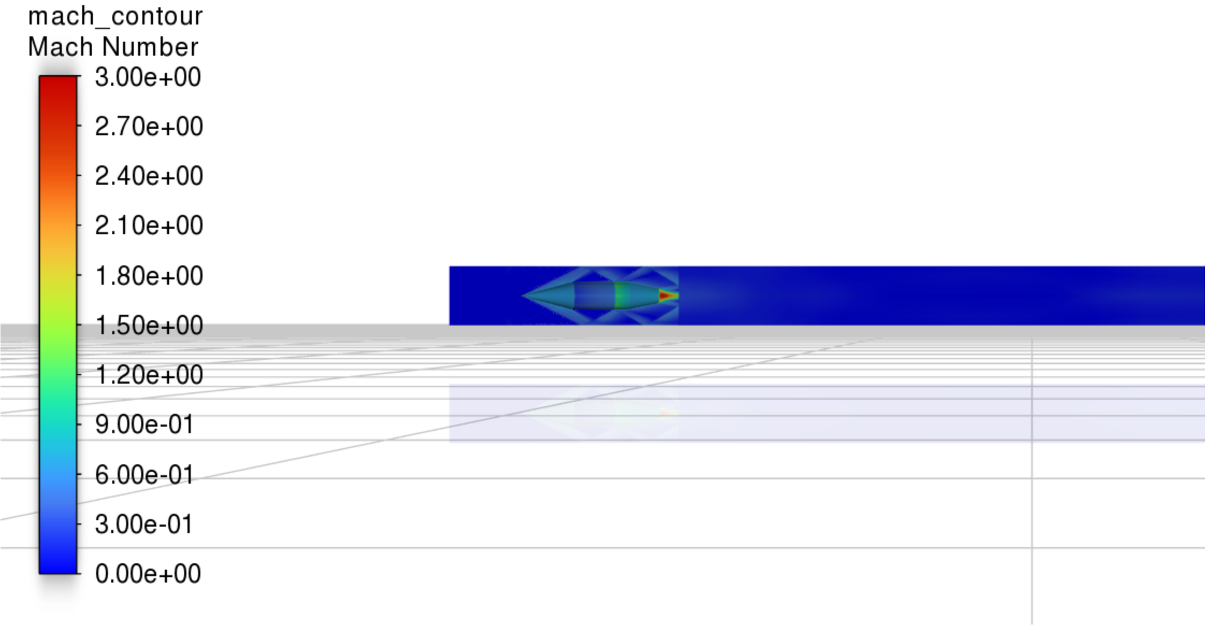

Figure 83. Mach contour of P380-2BL-12-15 in smooth bore (tube without baffles) at 1000 m/s.

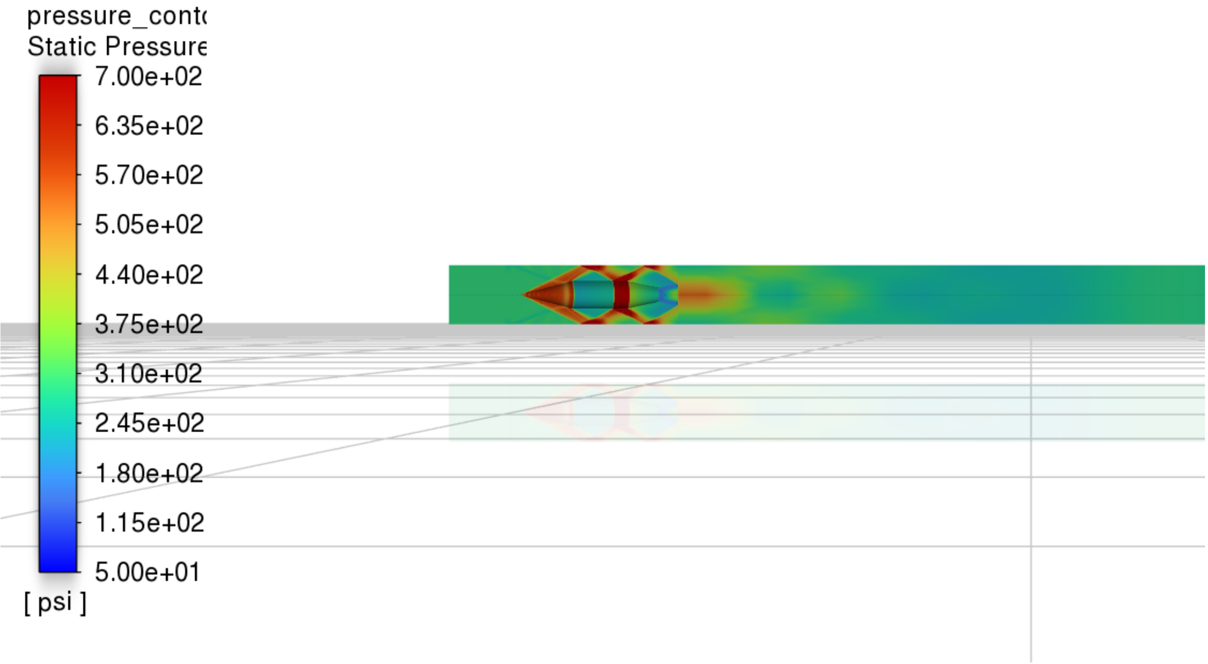

Figure 84. Pressure contour of P380-2BL-12-15 in smooth bore (tube without baffles) at 1000 m/s.

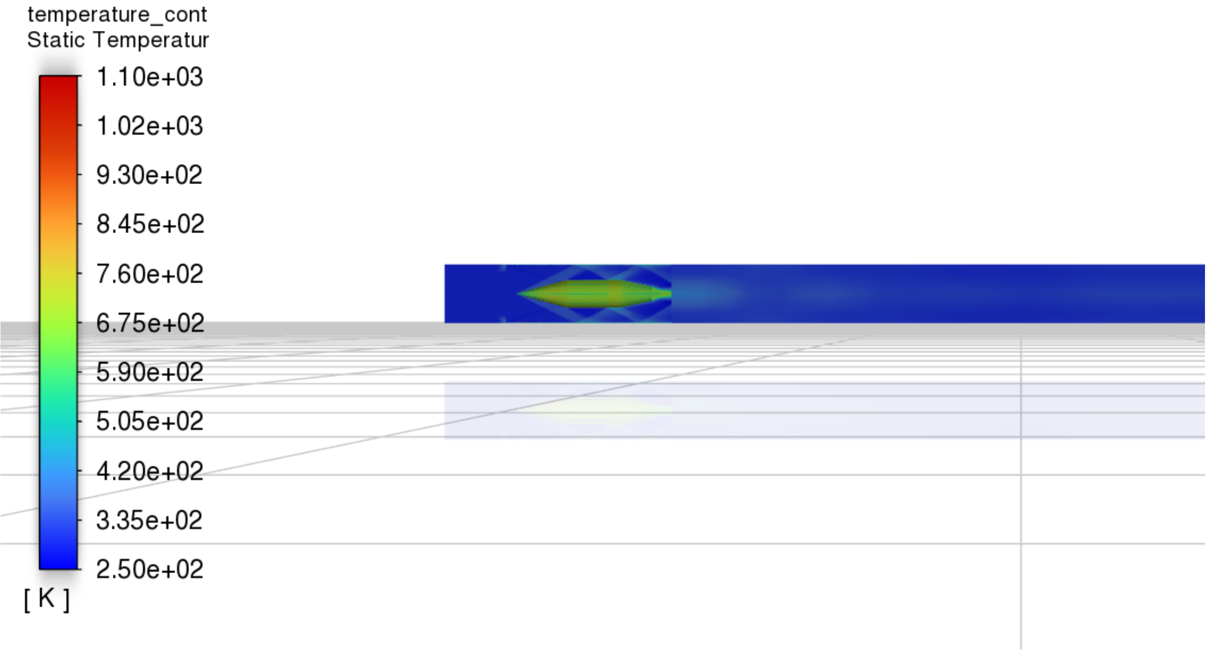

Figure 85. Temperature contour of P380-2BL-12-15 in smooth bore (tube without baffles) at 1000 m/s.

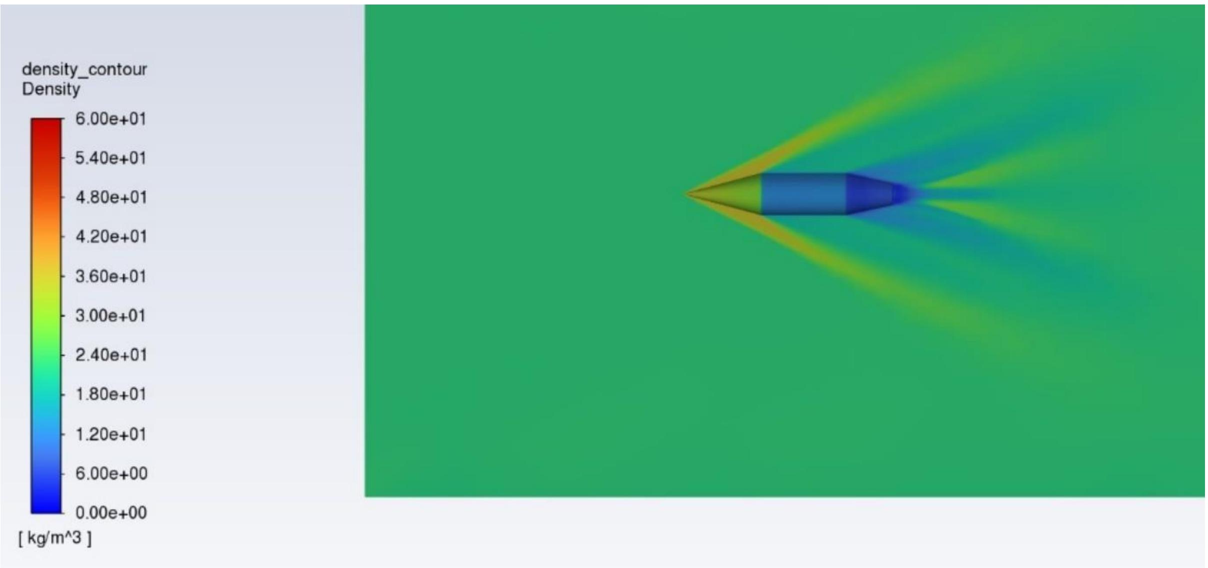

Figure 86. Density contour of P380-2BL-12-15 in free flight at (methane-air mixture at 300 psi) at 1000 m/s.

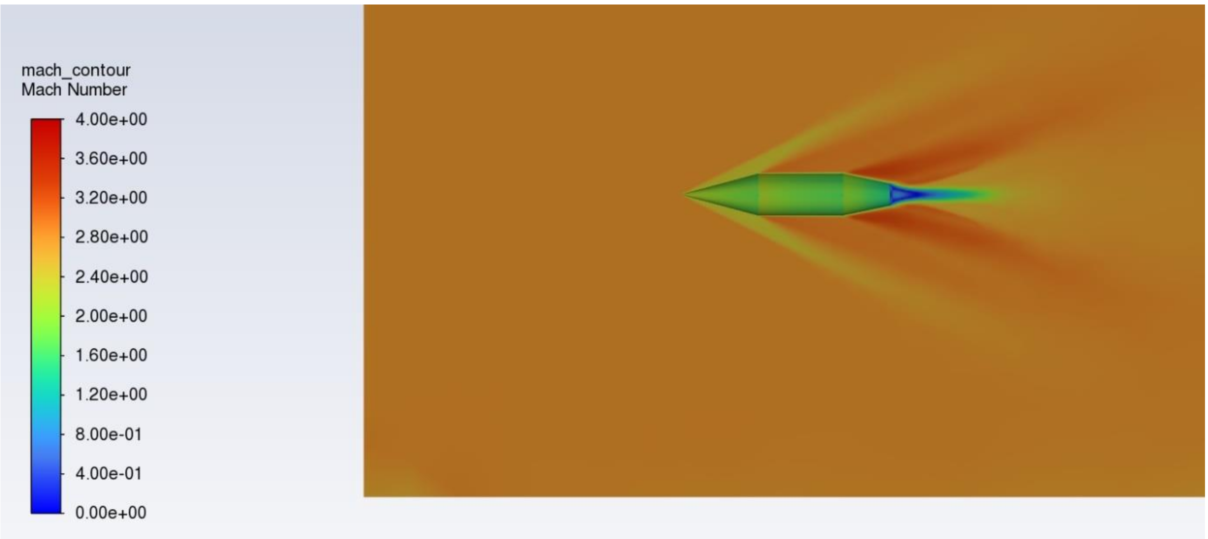

Figure 87. Mach contour of P380-2BL-12-15 in free flight (methane-air mixture at 300 psi) at 1000 m/s.

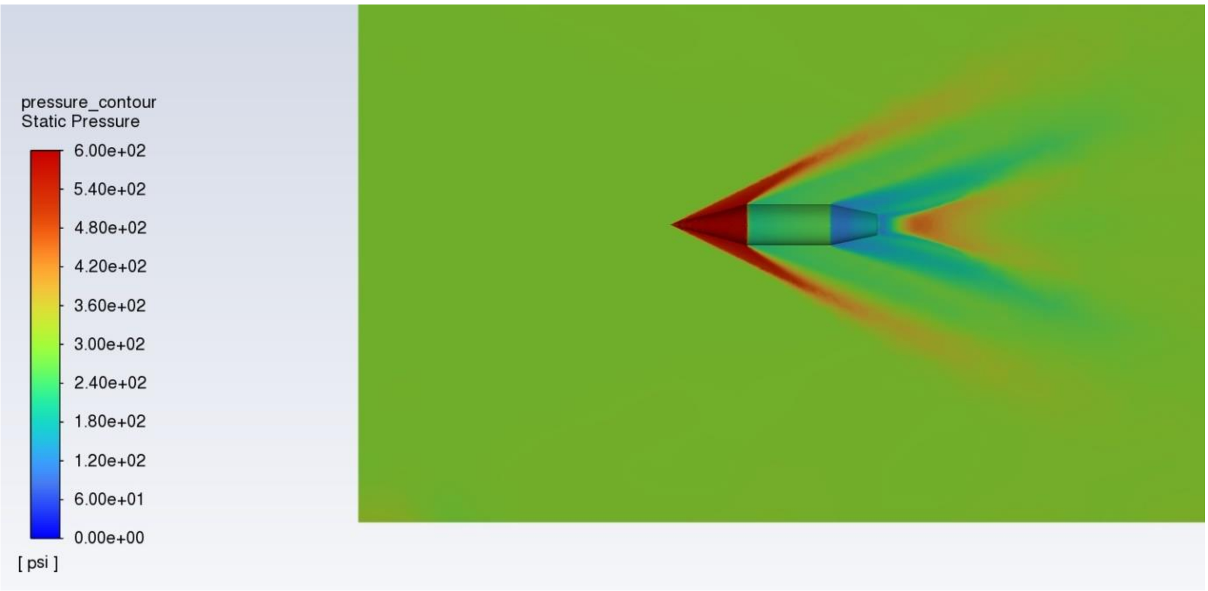

Figure 88. Pressure contour of P380-2BL-12-15 in free flight (methane-air mixture at 300 psi) at 1000 m/s.

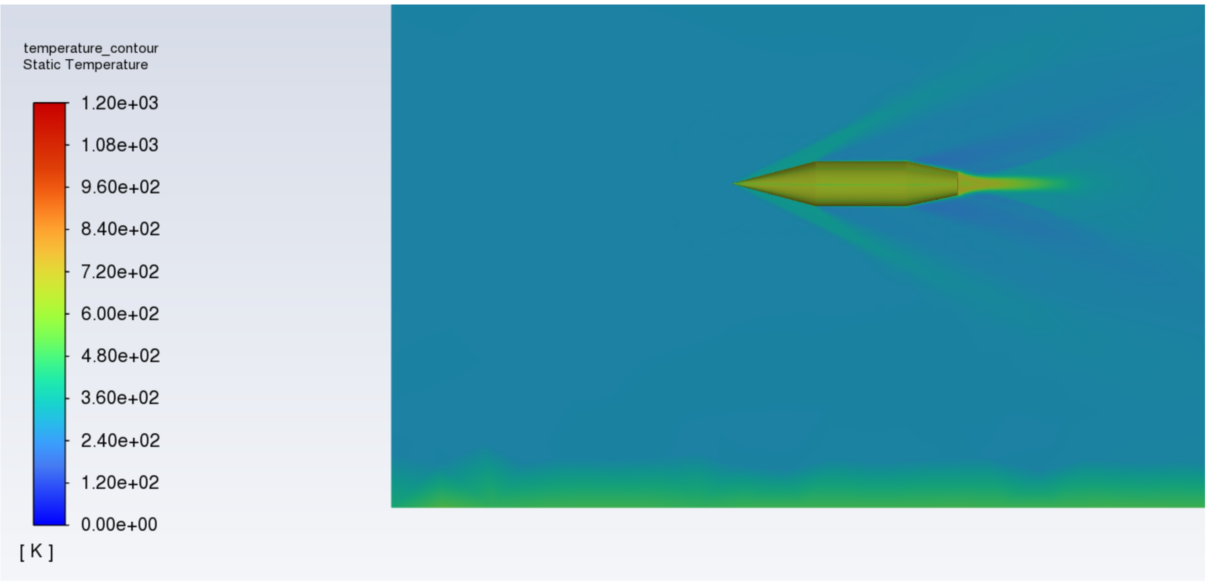

Figure 89. Temperature contour of P380-2BL-12-15 in free flight (methane-air mixture at 300 psi) at 1000 m/s.

8.3 Drawing Geometry

The geometries were drawn using Ansys design modeler. The steps are described below:

1. The domain was divided into 4 sections. One section having the projectile and its dimensions is referred to as b2. There are two rectangular sections, one in front of b2 and one at the back of b2. The domain in the back of b2 is b1 and the one in front is b3. Lastly, the domain containing the baffles is designated as b4.

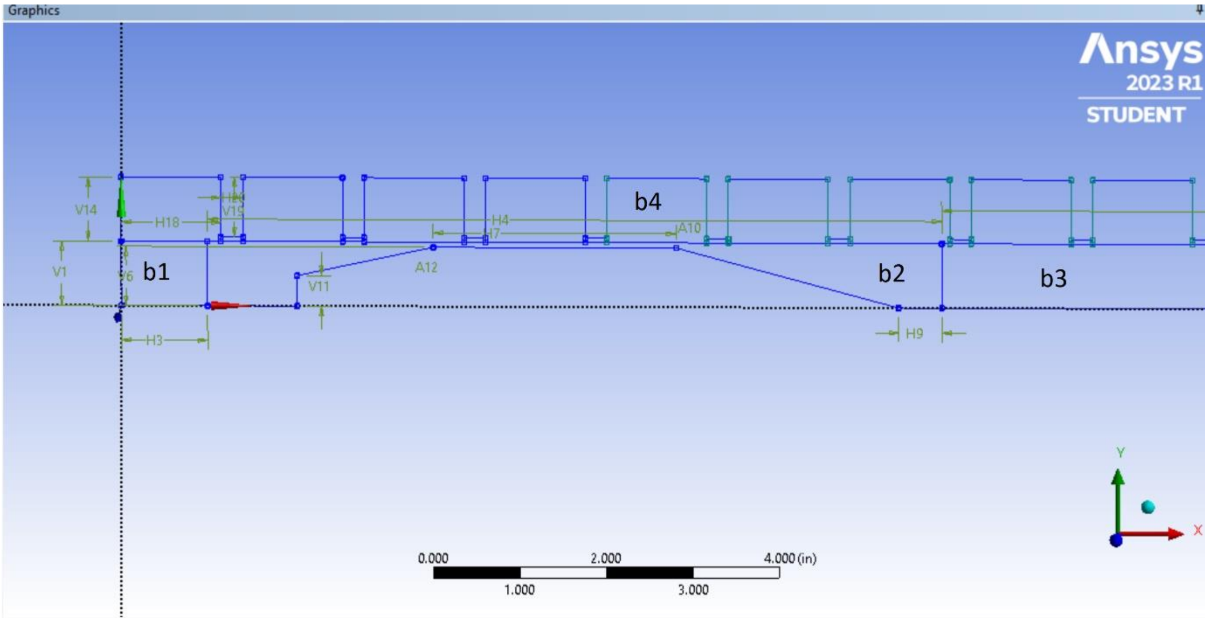

Figure 90. CFD domain drawing.

2. The length of b4 was 39 inches, b1 was 1 inch. The length of b2 and b3 vary based on the projectile size. It was ensured that all the sections connect to their neighboring sections.

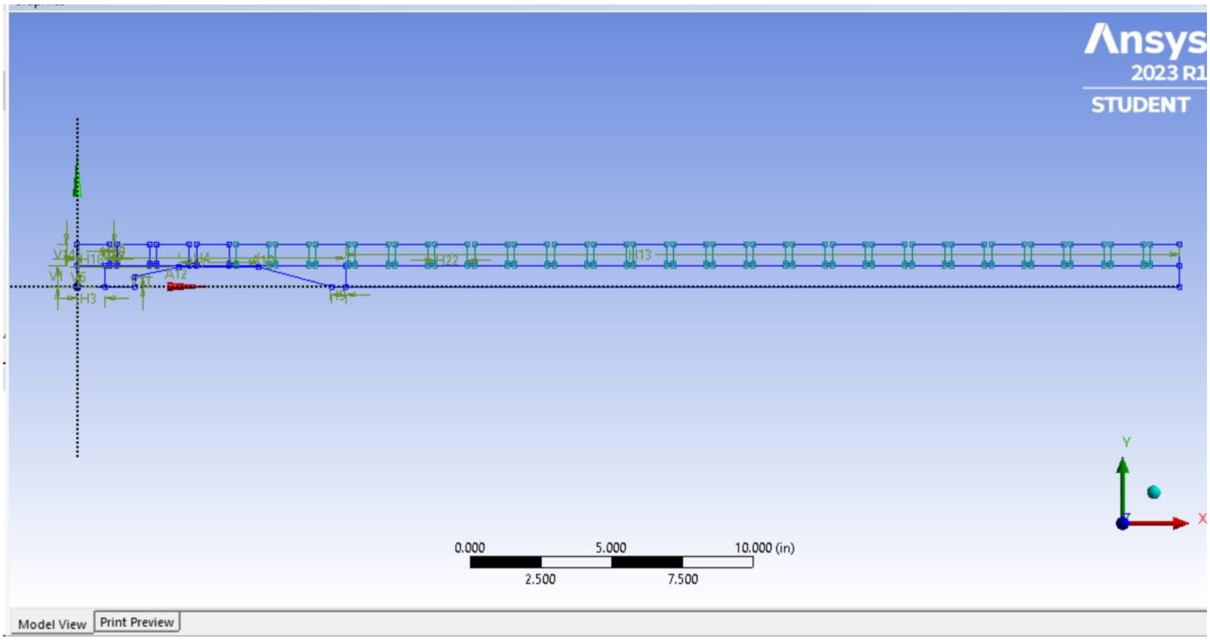

Figure 91. CFD domain drawing.

3. After the sketches were completed, the revolve feature was used to make a 1/8th symmetry domain, which is 45°.

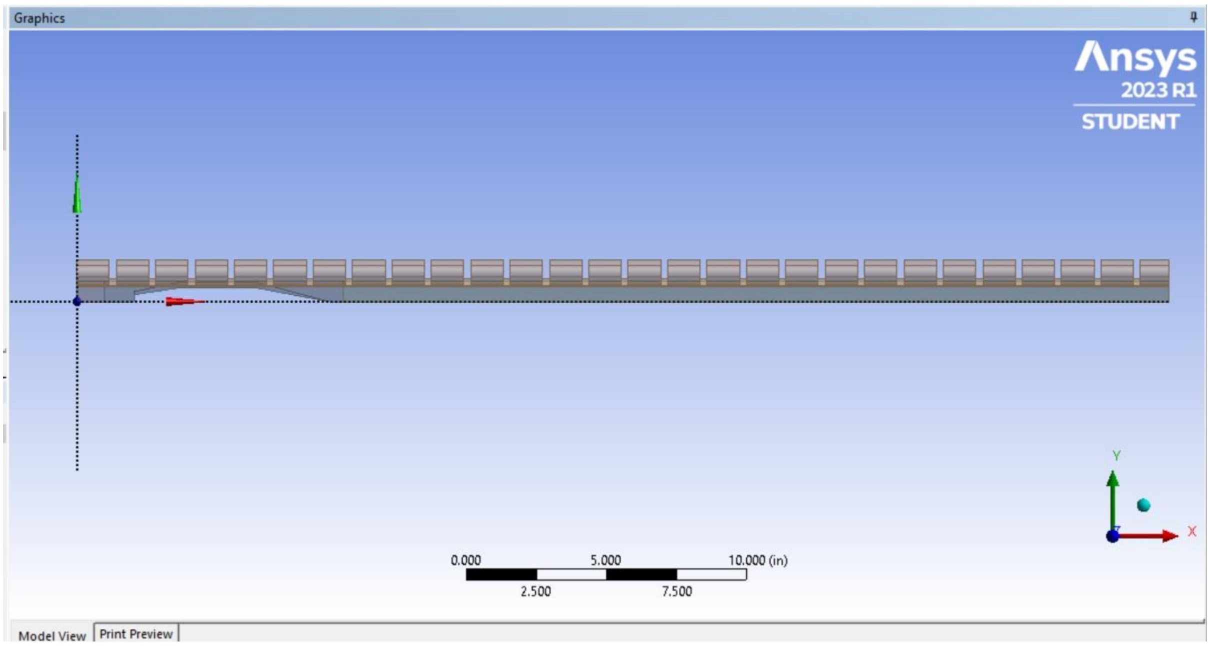

Figure 92. CFD domain drawing.

4. Now, the baffle rail was drawn which runs across the entire length of b4.

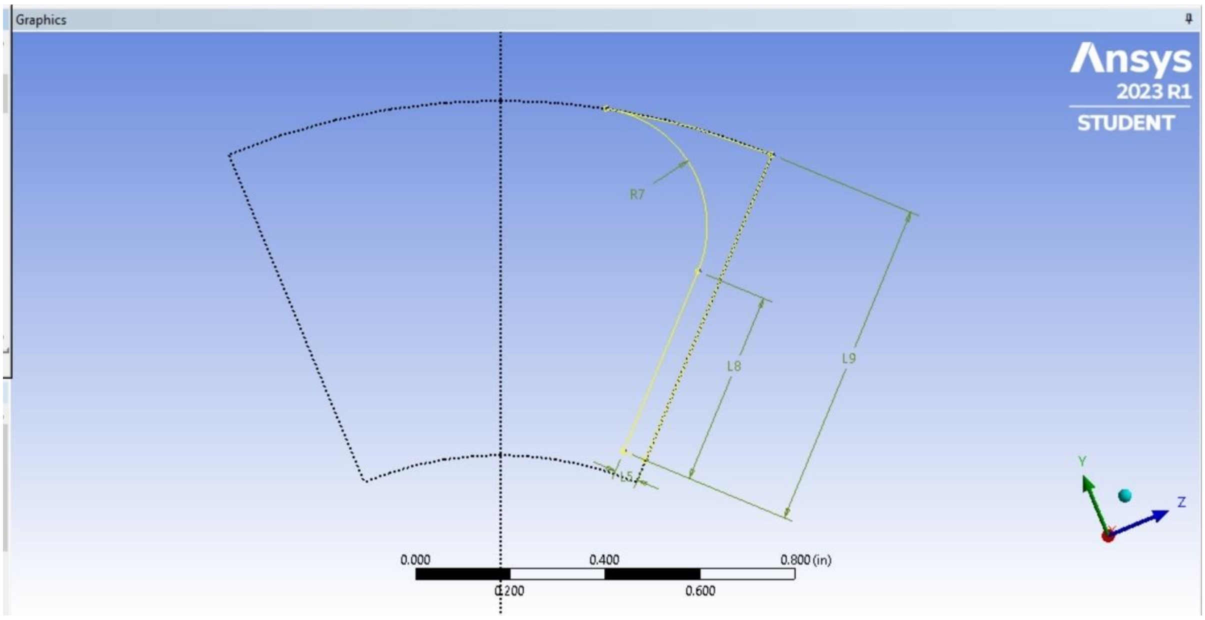

Figure 93. CFD domain drawing.

5. Extrude Feature was used to create the rail section (Slice materials, through all). All the small bodies generated from this operation were suppressed.

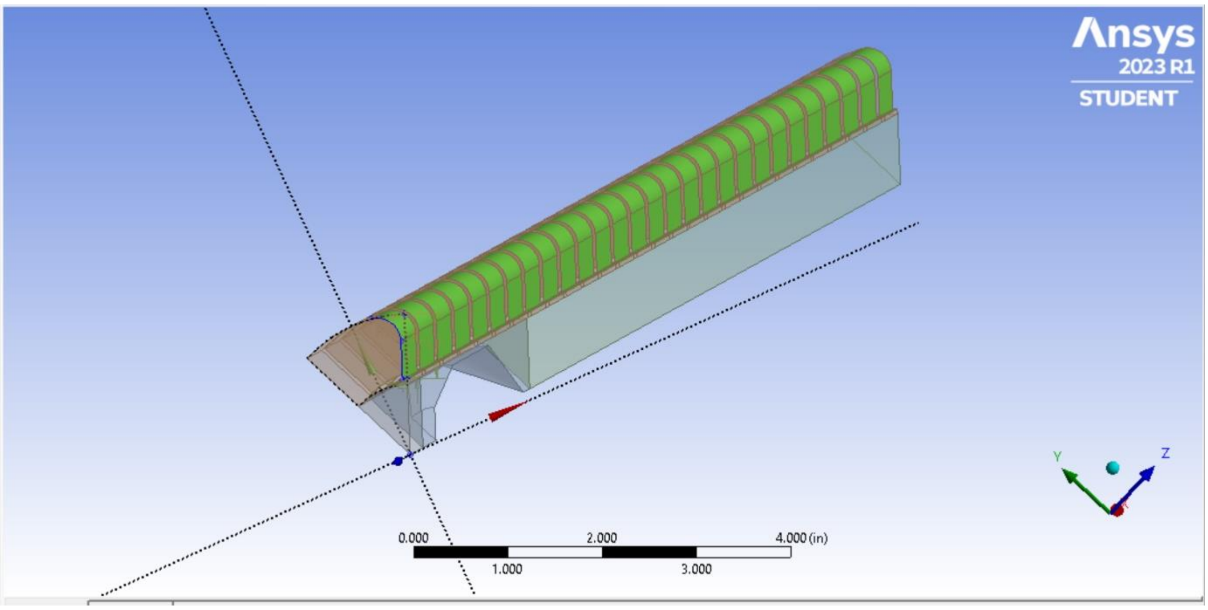

Figure 94. CFD domain drawing.

6. Now, small subsections under each baffle were drawn on both sides of b4 to fit to add more cells in that gap.

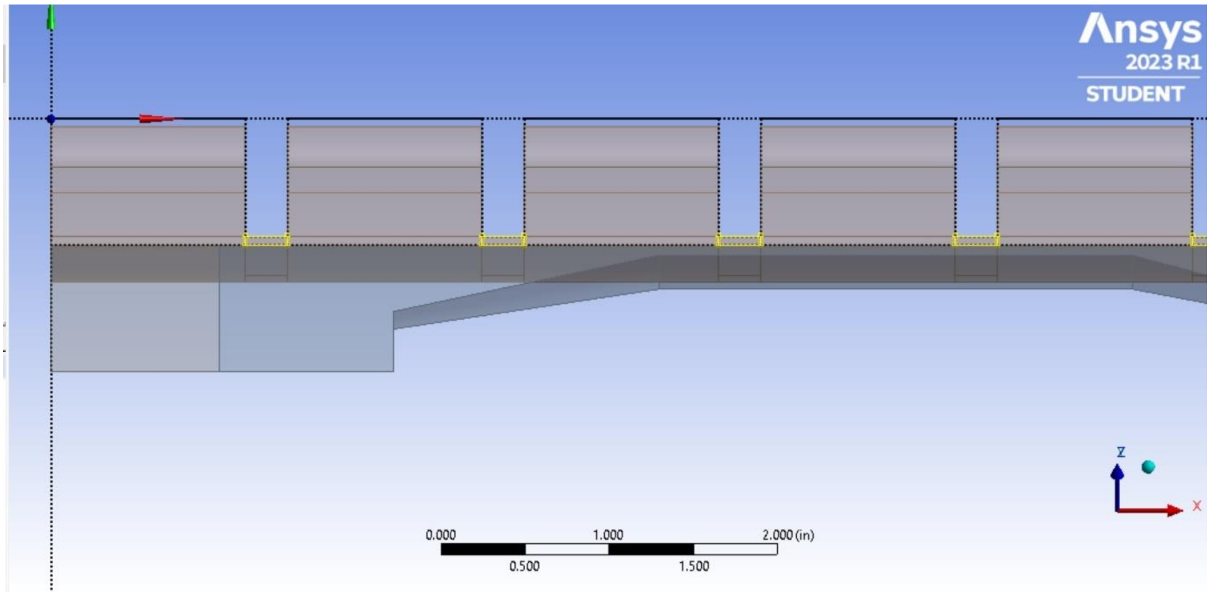

Figure 95. CFD domain drawing.

7. Line bodes were created from the sketches and the projection feature was used. The target face was the face that the drawing was on. By doing this, the small subsections can be selected.

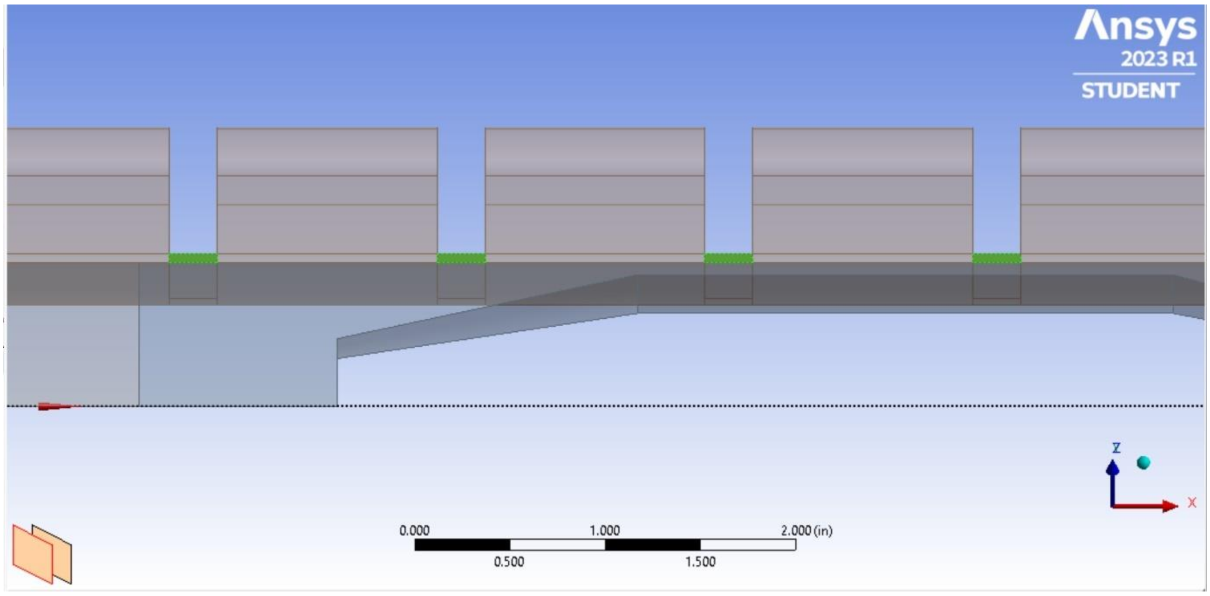

Figure 96. CFD domain drawing.

8. Domain was complete.

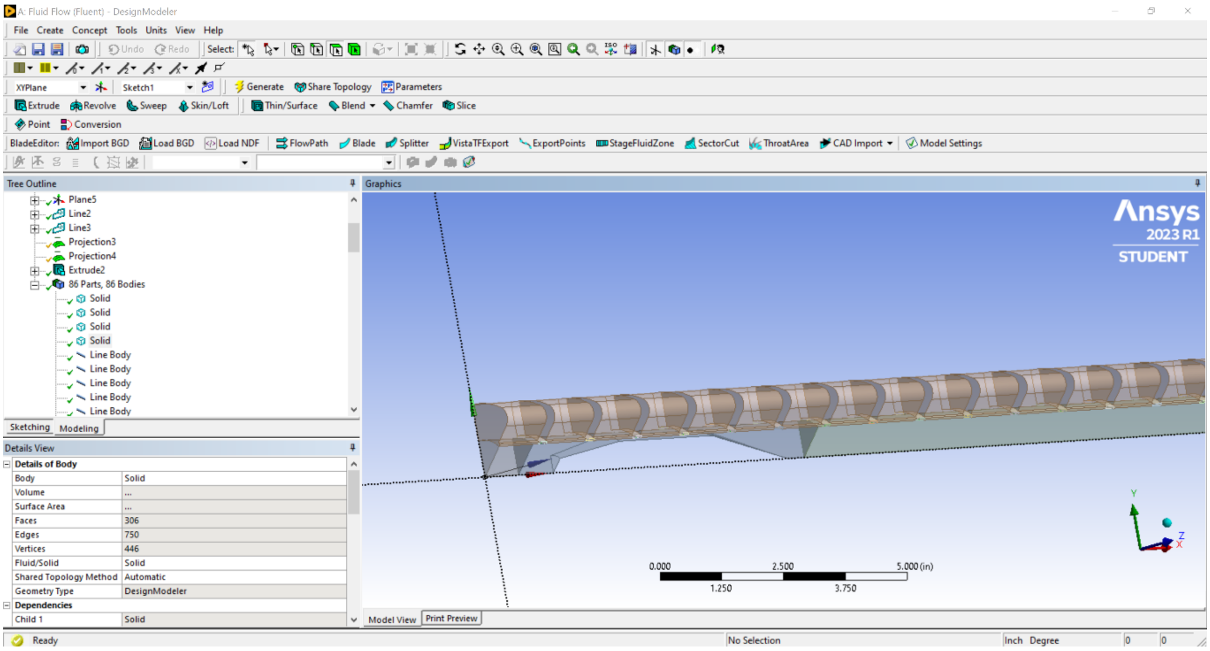

Details View

Details of Body	
Body	Solid
Volume	...
Surface Area	...
Faces	306
Edges	750
Vertices	446
Fluid/Solid	Solid
Shared Topology Method	Automatic
Geometry Type	DesignModeler
Dependencies	
Child 1	Solid

Figure 97. Complete CFD domain.

8.4 Meshing

The steps to complete the meshing are described below:

1. After importing the geometry into meshing, each of the face sections was named accordingly, including the inlet and the outlet. The end faces of b1 and b4 behind the projectile was considered as the outlet and end faces of b3 and b4 was considered as the inlet, assuming upstream of the flow is ahead of the projectile.

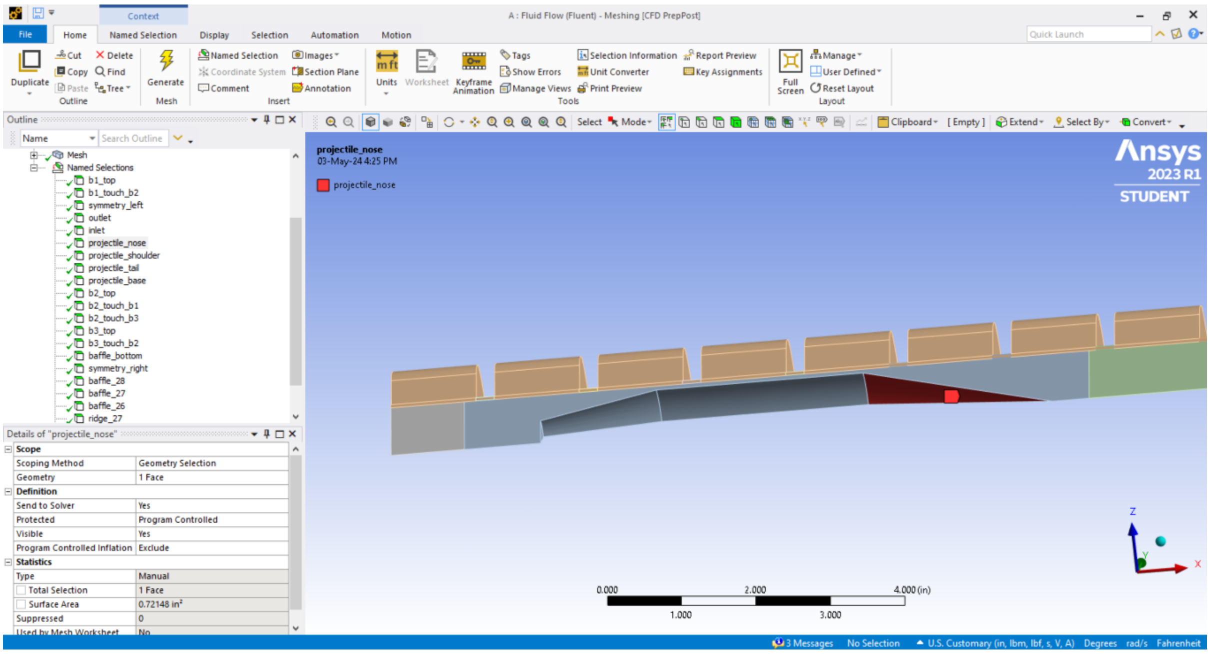

Details of "projectile_nose"

Scope	
Scoping Method	Geometry Selection
Geometry	1 Face
Definition	
Send to Solver	Yes
Protected	Program Controlled
Visible	Yes
Program Controlled Inflation	Exclude
Statistics	
Type	Manual
☐ Total Selection	1 Face
☐ Surface Area	0.72148 in²
Suppressed	0
Used by Mesh Worksheet	No

Figure 98. CFD Meshing.

2. Contacts were created accordingly to make the mesh airtight.

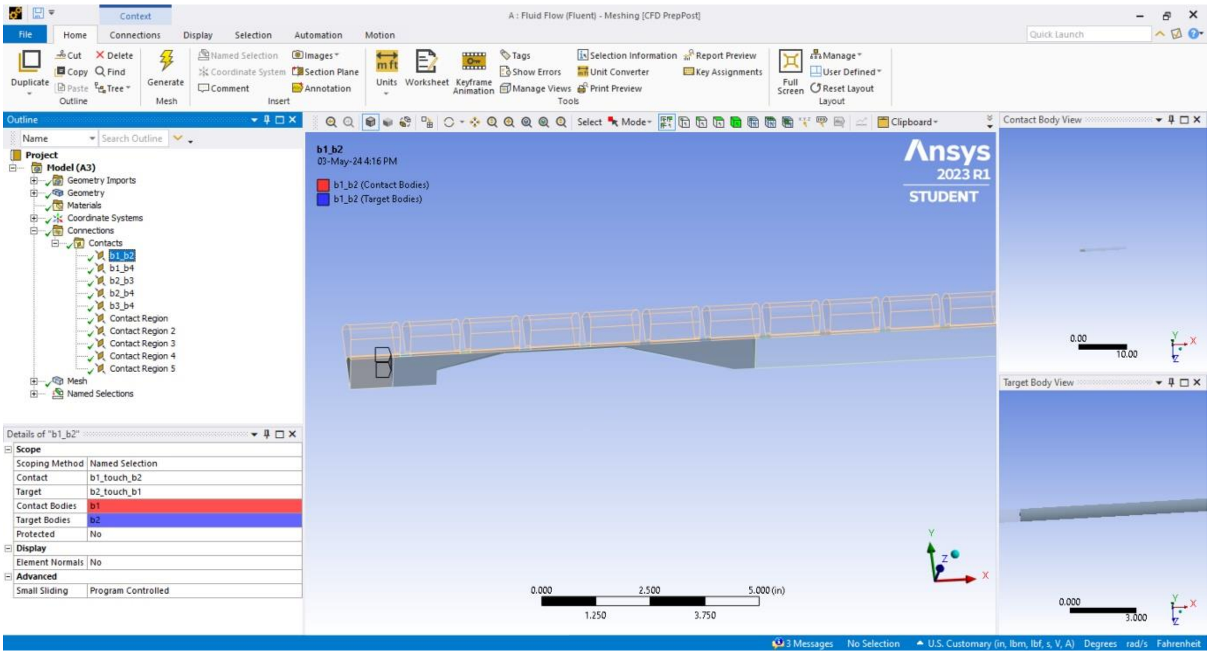

Details of "b1_b2"

Scope	
Scoping Method	Named Selection
Contact	b1_touch_b2
Target	b2_touch_b1
Contact Bodies	b1
Target Bodies	b2
Protected	No
Display	
Element Normals	No
Advanced	
Small Sliding	Program Controlled

Figure 99. CFD Meshing.

3. Then the mesh was generated. The cell sizes were varied depending on the importance of the region. Sections b1 and b3 can have coarse meshes as they are of less importance. Whereas b2 had to be much finer as it has the projectile in it.

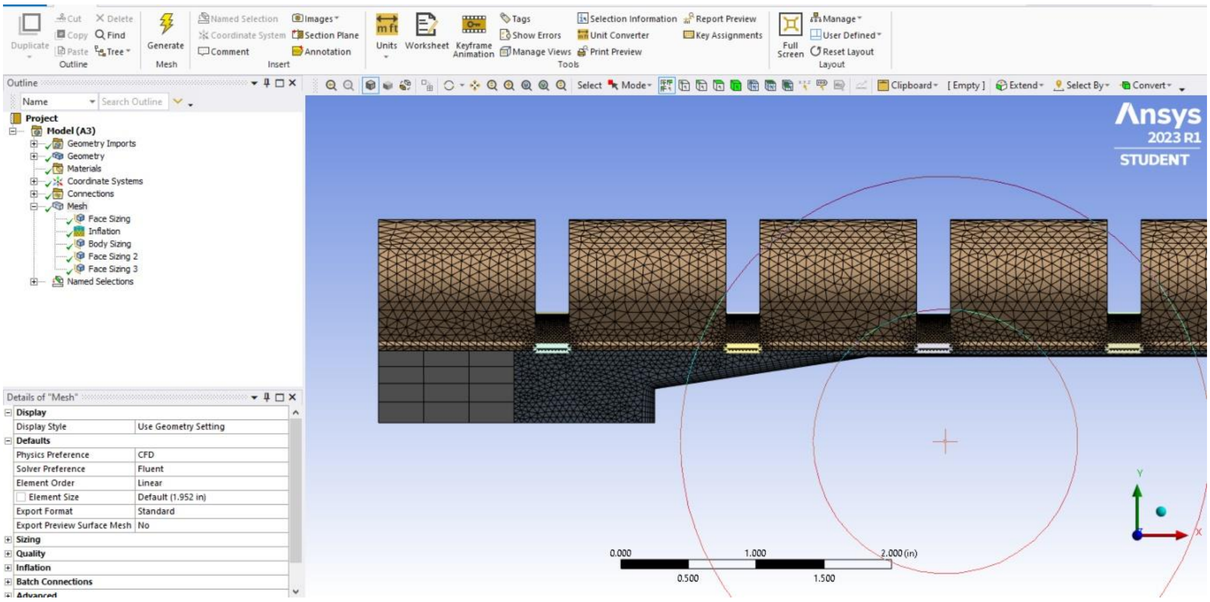

Details of "Mesh"

Display	
Display Style	Use Geometry Setting
Defaults	
Physics Preference	CFD
Solver Preference	Fluent
Element Order	Linear
☐ Element Size	Default (1.952 in)
Export Format	Standard
Export Preview Surface Mesh	No
Sizing	
Quality	
Inflation	
Batch Connections	
Advanced	

Figure 100. CFD Meshing.

4. Face sizing was added to the baffle regions.

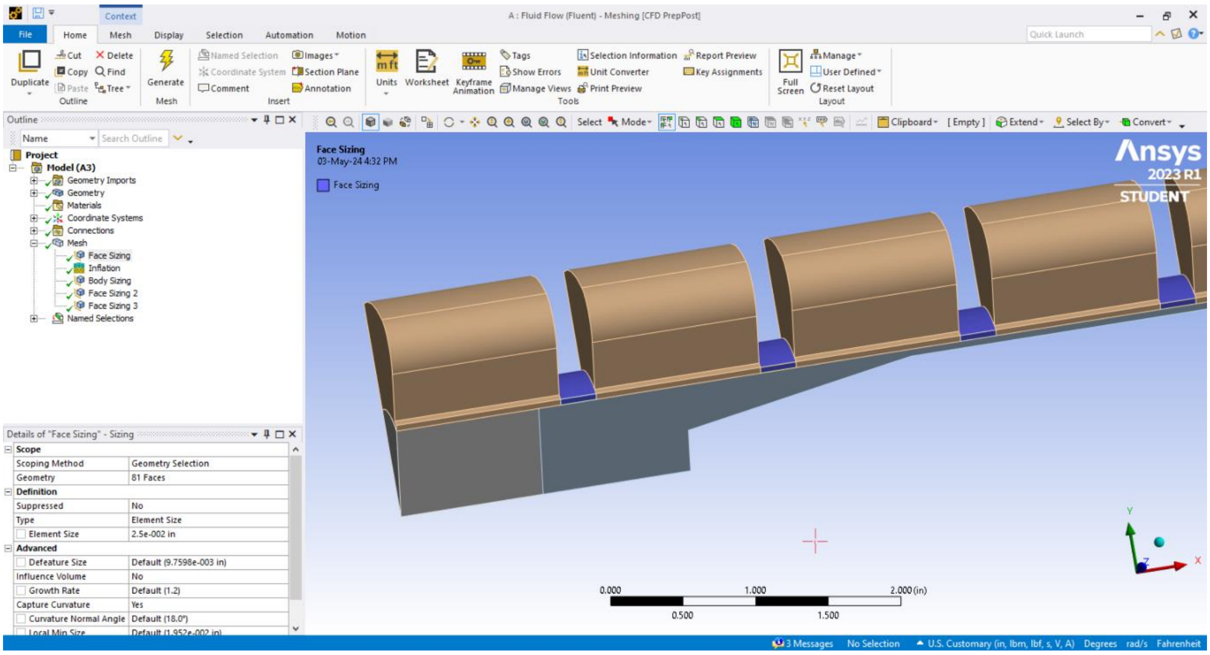

Details of "Face Sizing" - Sizing

Scope	
Scoping Method	Geometry Selection
Geometry	81 Faces
Definition	
Suppressed	No
Type	Element Size
☐ Element Size	2.5e-002 in
Advanced	
☐ Defeature Size	Default (9.7598e-003 in)
Influence Volume	No
☐ Growth Rate	Default (1.2)
Capture Curvature	Yes
☐ Curvature Normal Angle	Default (18.0°)
☐ Local Min Size	Default (1.952e-002 in)

Figure 101. CFD Meshing.

5. Face sizing was also added to other regions to increase the quality of the mesh.

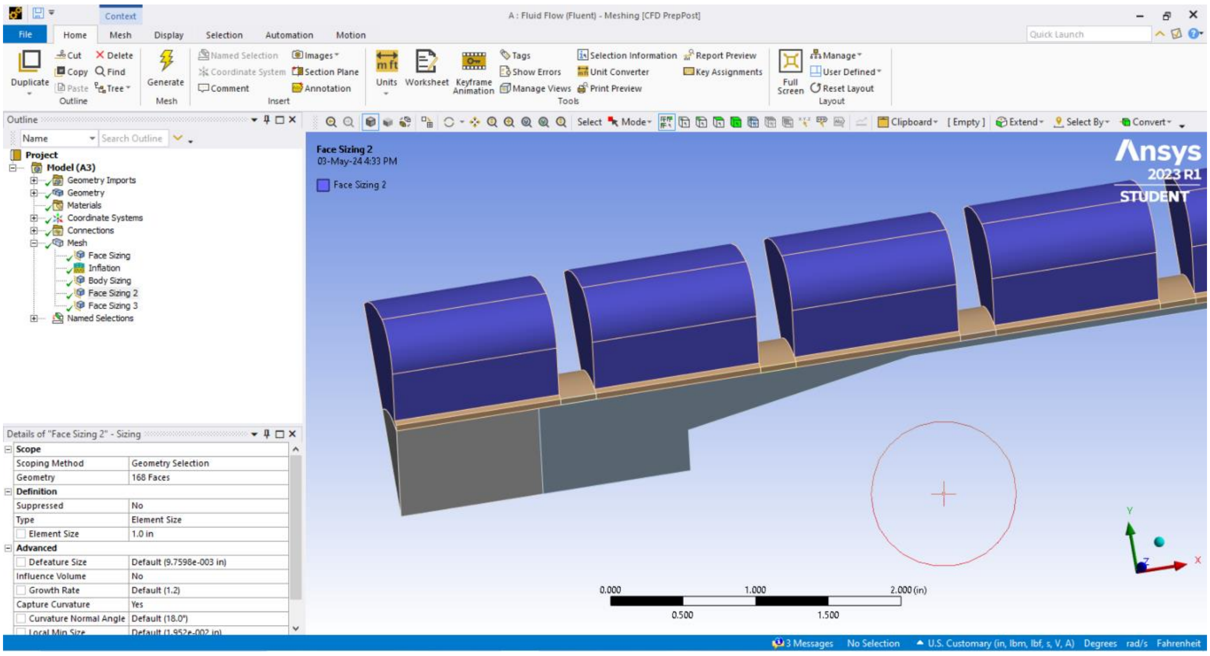

Details of "Face Sizing 2" - Sizing

Scope	
Scoping Method	Geometry Selection
Geometry	168 Faces
Definition	
Suppressed	No
Type	Element Size
☐ Element Size	1.0 in
Advanced	
☐ Defeature Size	Default (9.7598e-003 in)
Influence Volume	No
☐ Growth Rate	Default (1.2)
Capture Curvature	Yes
☐ Curvature Normal Angle	Default (18.0°)
☐ Local Min Size	Default (1.952e-002 in)

Figure 102. CFD Meshing.

6. Six layers of inflations were added to the projectile section to have accurate flow simulation around the projectile.

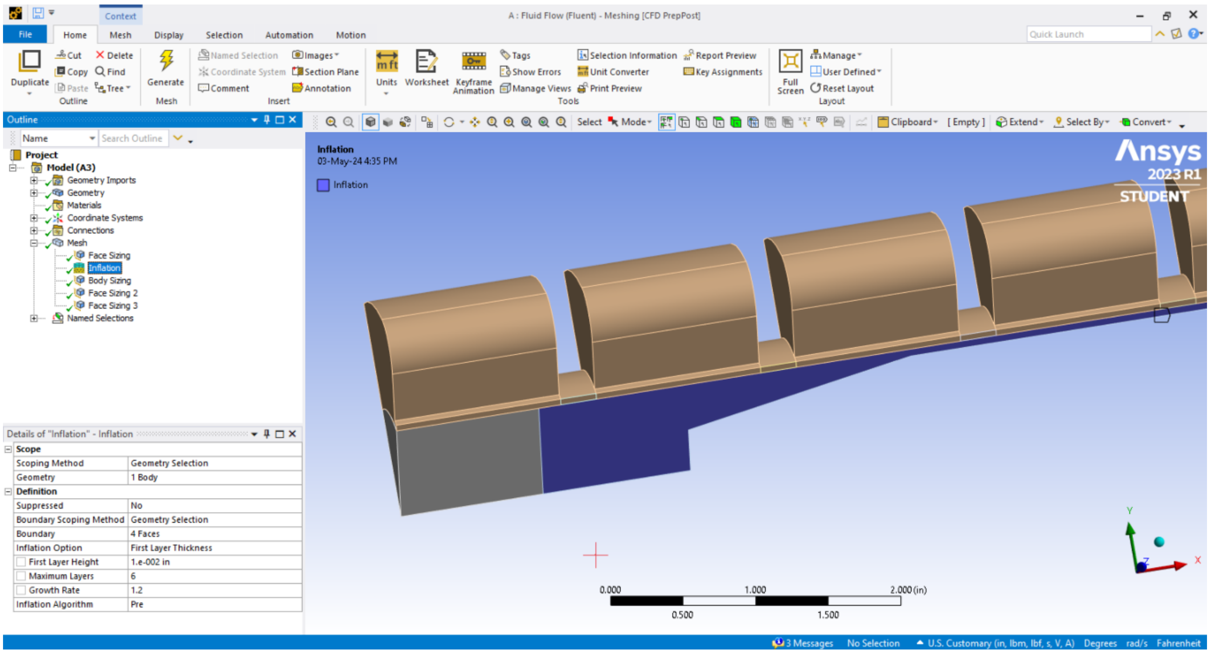

Details of "Inflation" - Inflation

Scope	
Scoping Method	Geometry Selection
Geometry	1 Body
Definition	
Suppressed	No
Boundary Scoping Method	Geometry Selection
Boundary	4 Faces
Inflation Option	First Layer Thickness
☐ First Layer Height	1.e-002 in
☐ Maximum Layers	6
☐ Growth Rate	1.2
Inflation Algorithm	Pre

Figure 103. CFD Meshing.

7. Meshing was complete.

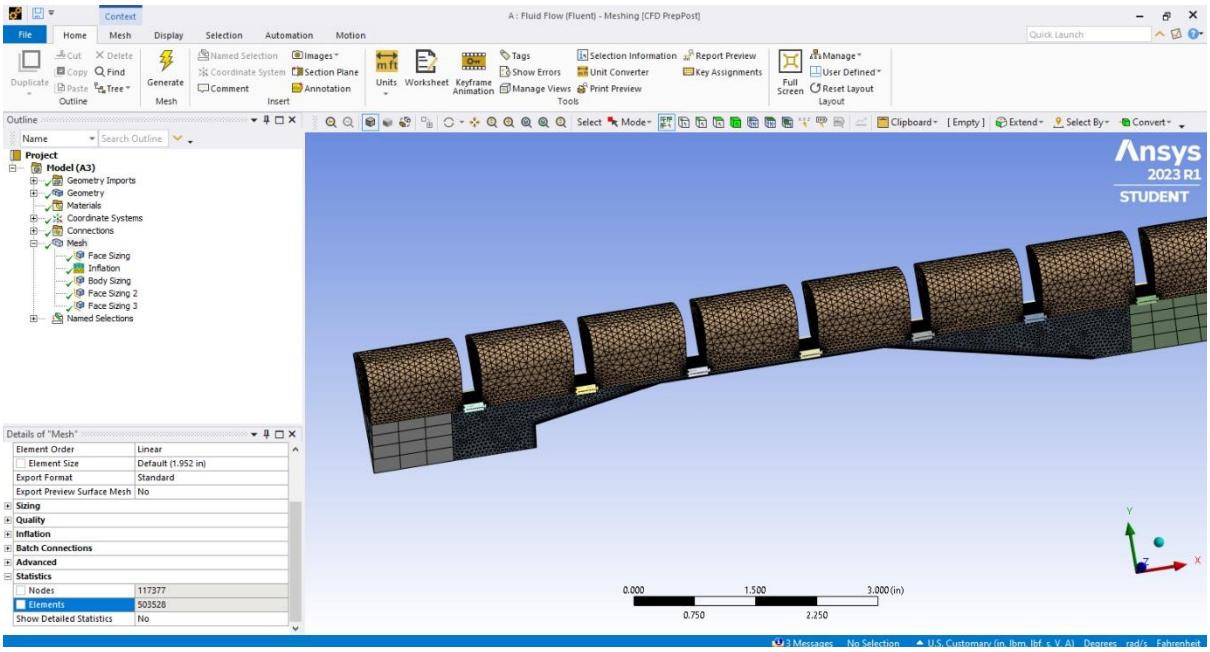

Details of "Mesh"

Element Order	Linear
☐ Element Size	Default (1.952 in)
Export Format	Standard
Export Preview Surface Mesh	No
⊞ **Sizing**	
⊞ **Quality**	
⊞ **Inflation**	
⊞ **Batch Connections**	
⊞ **Advanced**	
⊟ **Statistics**	
☐ Nodes	117377
☐ Elements	503528
Show Detailed Statistics	No

Figure 104. CFD Meshing.

8.5 Solver Setup

Server computer ram1 was used to run the simulations. The input parameters and steps are described below:

1. After completing the mesh, the mesh was imported to Ansys fluent on ram1. Parallel processing with 38 cores was selected with double precision to launch Fluent.

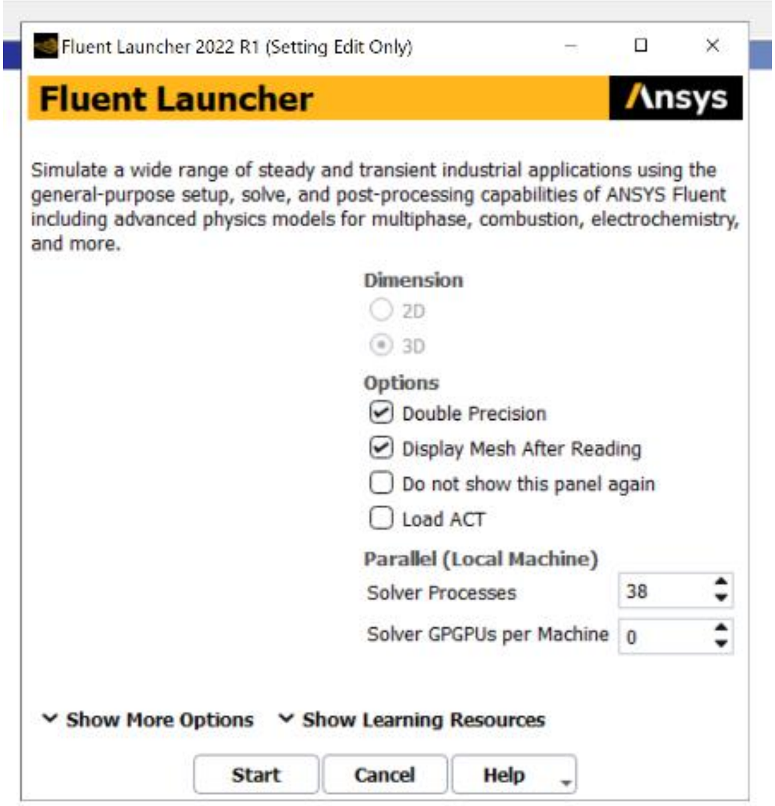

Simulate a wide range of steady and transient industrial applications using the general-purpose setup, solve, and post-processing capabilities of ANSYS Fluent including advanced physics models for multiphase, combustion, electrochemistry, and more.

Dimension
○ 2D
● 3D

Options
☑ Double Precision
☑ Display Mesh After Reading
☐ Do not show this panel again
☐ Load ACT

Parallel (Local Machine)
Solver Processes 38
Solver GPGPUs per Machine 0

Figure 105. Fluent launch window.

2. After loading the mesh, units were checked. The length was in inches and the pressure was in psi. Everything else remained unchanged.
3. View > display > views, all the planes shown in the box were selected and mirrored. This way, the cross-section of the domain from the side and the projectile motions were seen.

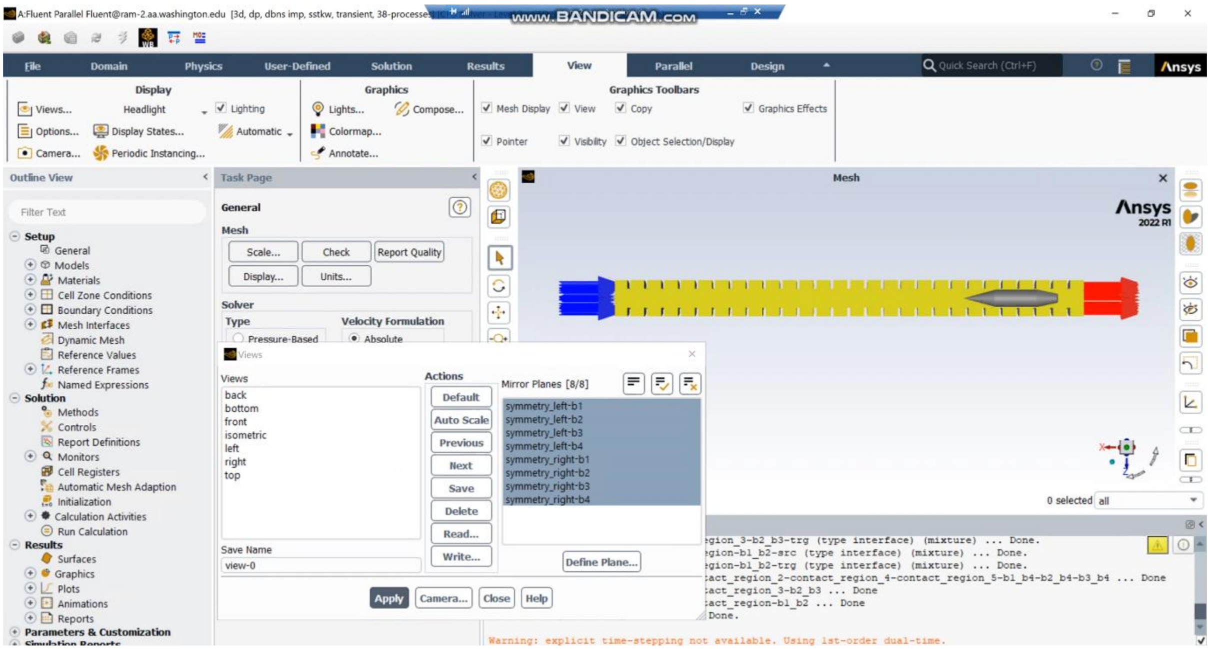

```
gion_3-b2_b3-trg (type interface) (mixture) ... Done.
gion-b1_b2-src (type interface) (mixture) ... Done.
gion-b1_b2-trg (type interface) (mixture) ... Done.
act_region_2-contact_region_4-contact_region_5-b1_b4-b2_b4-b3_b4 ... Done
act_region_3-b2_b3 ... Done
act_region-b1_b2 ... Done
Done.
Warning: explicit time-stepping not available. Using 1st-order dual-time.
```

Figure 106. Fluent solver setup.

4. Model > Energy: ON, Species: Species Transport. Select methane-air.
5. Materials > ideal gas was selected.
6. Model > viscous model K-SST omega, compressibility effect was tuned on.
7. Cell zone conditions > operating pressure was set to 0.
8. Boundary Condition > for both inlets, 300 psi for initial and outflow gauge pressure and 300k temperature were selected. In the species tab, mole fraction was selected, 0.128 for CH4 and 0.257 for O2 were put. The rest remained 0. N2 was the balance in the mixture.

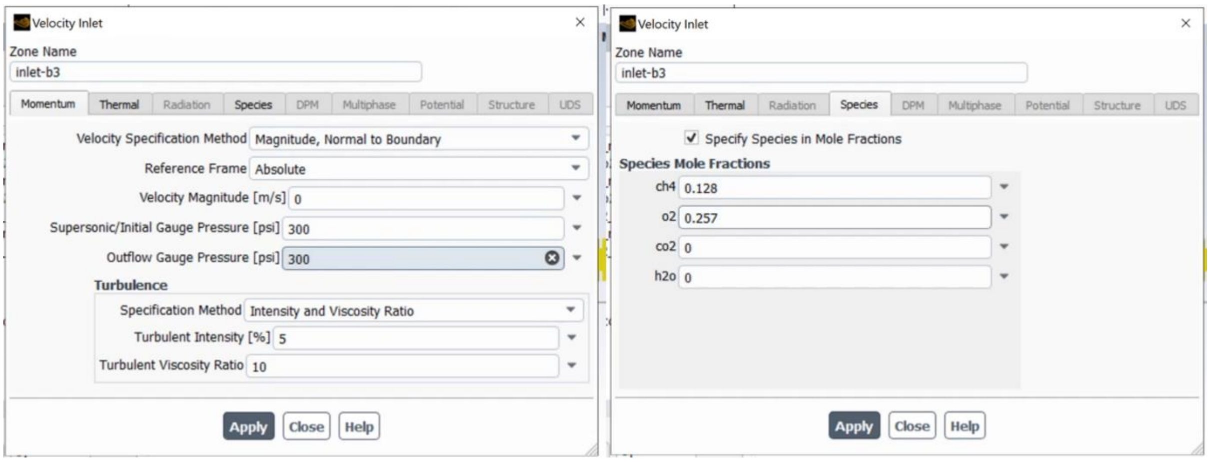

Zone Name: inlet-b3

Velocity Specification Method: Magnitude, Normal to Boundary

Reference Frame: Absolute

Velocity Magnitude [m/s]: 0

Supersonic/Initial Gauge Pressure [psi]: 300

Outflow Gauge Pressure [psi]: 300

Turbulence

Specification Method: Intensity and Viscosity Ratio

Turbulent Intensity [%]: 5

Turbulent Viscosity Ratio: 10

Zone Name: inlet-b3

☑ Specify Species in Mole Fractions

Species Mole Fractions

ch4: 0.128

o2: 0.257

co2: 0

h2o: 0

Figure 107. Fluent solver setup.

9. For both outlets, 300 psi gauge pressure and “prevent reverse flow” were selected.
10. Nest step was dynamic mesh. To use dynamic mesh, a c code was compiled to create the udf (user defined function). The udf was added by browsing, user defined > functions > compiled > add. Then the file path shown in the box was opened and the c code was pasted. The c code was selected in fluent. Then the udf was built and loaded.
11. The dynamic mesh was turned on. Layering was selected and ratio-based was chosen.
12. Dynamic mesh zones were created. B2 and its front and back interfaces (4 interfaces) were selected as a rigid body. The cell height was set to 1.6 in on the meshing option.
13. B4 and the inlets and outlets were set as stationary, with a cell height of 1.6 in.
14. B1 and b3 were set as deforming. Global settings were unchecked. Zone scale info was clicked to see the minimum and maximum length scale for b1 and b3. The same minimum length scale within the range for both b1 and b3 was entered. Similarly, the same maximum length scale was entered.

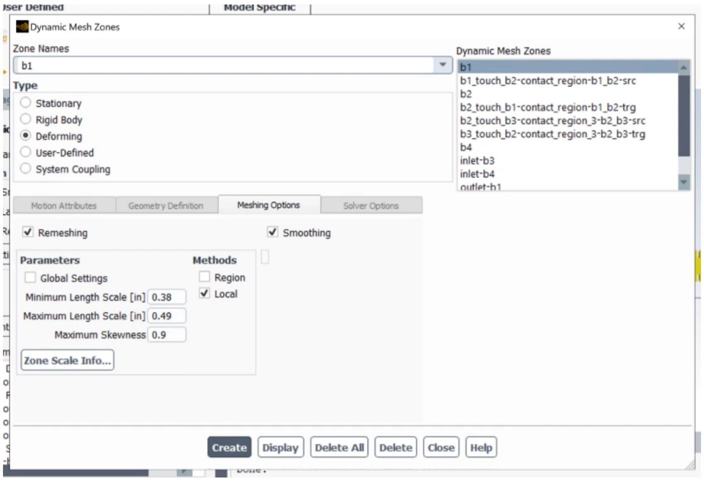

Zone Names: b1

Type
○ Stationary
○ Rigid Body
● Deforming
○ User-Defined
○ System Coupling

Dynamic Mesh Zones
b1
b1_touch_b2-contact_region-b1_b2-src
b2
b2_touch_b1-contact_region-b1_b2-trg
b2_touch_b3-contact_region_3-b2_b3-src
b3_touch_b2-contact_region_3-b2_b3-trg
b4
inlet-b3
inlet-b4
outlet-b1

☑ Remeshing
☑ Smoothing

Parameters
☐ Global Settings
Minimum Length Scale [in] 0.38
Maximum Length Scale [in] 0.49
Maximum Skewness 0.9

Methods
☐ Region
☑ Local

Figure 108. Fluent solver setup.

15. The dynamic mesh was checked using display mesh motion. The project was reset and saved.
16. The mesh was checked using preview mesh motion. The projectile was ensured to move forward without errors. The mesh was changed permanently, so the project was exited without saving and restarted to retrieve the initial state of the domain.
17. Solution > Methods > Implicit > AUSM was selected. High Order Term relaxation for all variables was chosen.
18. Solution > Controls > Courant Number was selected as 0.2. Limits were set and the following parameters were adjusted.

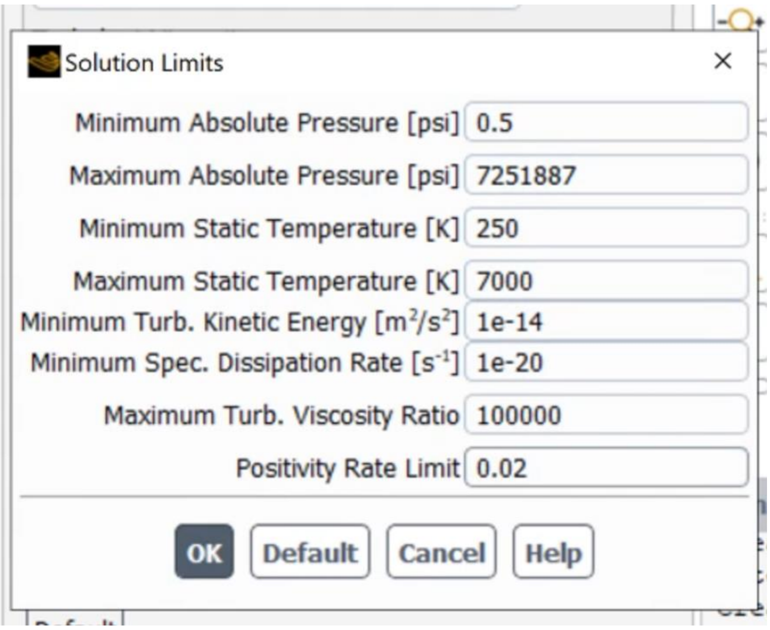

Minimum Absolute Pressure [psi] 0.5

Maximum Absolute Pressure [psi] 7251887

Minimum Static Temperature [K] 250

Maximum Static Temperature [K] 7000

Minimum Turb. Kinetic Energy $[m^2/s^2]$ 1e-14

Minimum Spec. Dissipation Rate $[s^{-1}]$ 1e-20

Maximum Turb. Viscosity Ratio 100000

Positivity Rate Limit 0.02

Figure 109. Fluent solver setup.

19. The parameters to make the plots were created. Report definitions > New > Force report was selected. Cd and drag parameters for nose, shoulder, tail, and base were created. Create report file and plot were unchecked.
20. A density parameter was created from new > surface report > area weighted average. All surfaces were selected. Create report file and plot were unchecked.
21. A density parameter was created from new > volume > mass average. All cell zones were selected. Create report file and plot were unchecked.
22. Monitor > Create New Report file was selected and all report definitions were added.

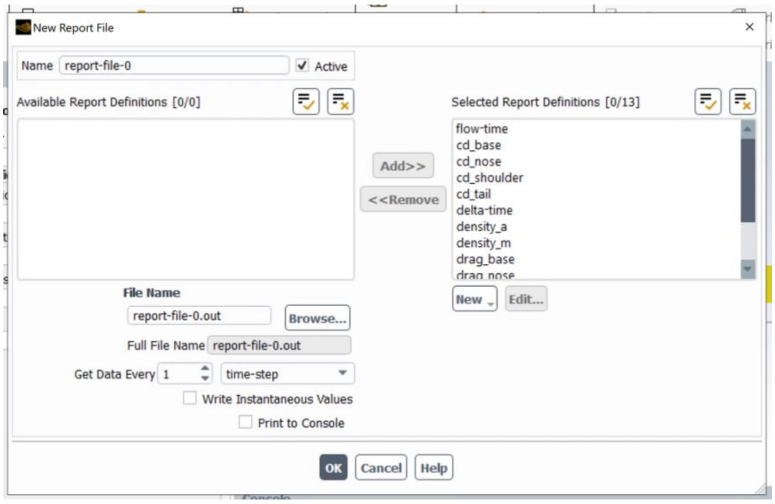

Name report-file-0 ☑ Active

Available Report Definitions [0/0]

Selected Report Definitions [0/13]
- flow-time
- cd_base
- cd_nose
- cd_shoulder
- cd_tail
- delta-time
- density_a
- density_m
- drag_base
- drag_nose

File Name report-file-0.out

Full File Name report-file-0.out

Get Data Every 1 time-step

☐ Write Instantaneous Values

☐ Print to Console

Figure 110. Fluent solver setup.

23. Initialization > Standard initialization > compute from inlet was selected.
24. Calculation activities > Solution animation > New Object > Contour was selected. The desired contours were created using global range, selecting all surfaces. Animation for the corresponding object was created and bottom was selected as the view. Animation for pressure, density, temperature, and Mach number for certain cases was created.

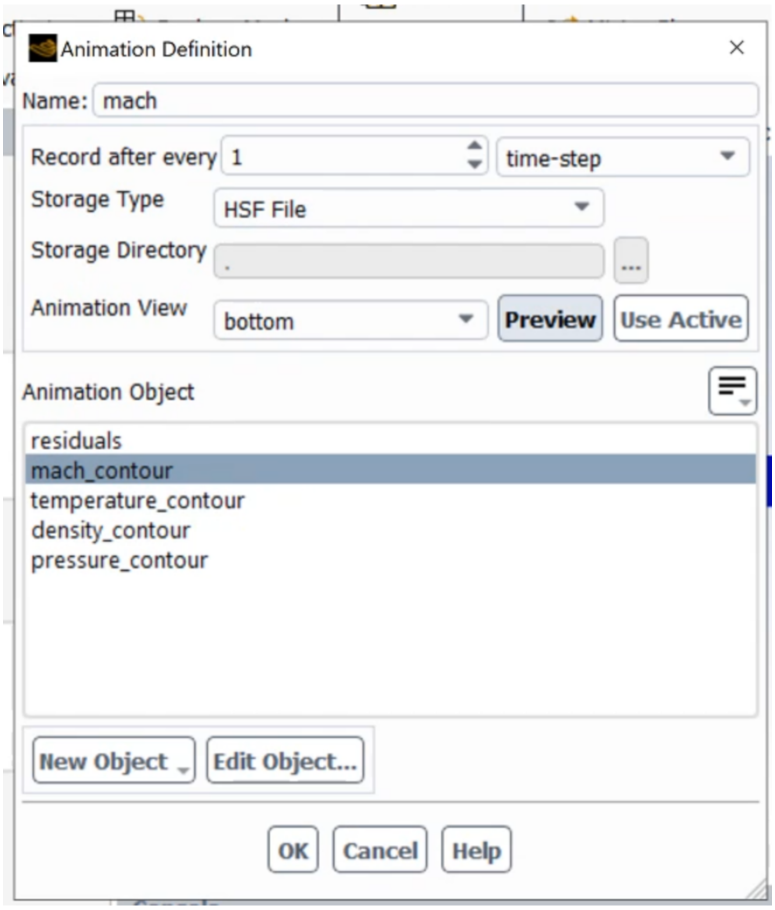

Animation Definition

Name: mach

Record after every 1 time-step

Storage Type HSF File

Storage Directory .

Animation View bottom

Animation Object

residuals
mach_contour
temperature_contour
density_contour
pressure_contour

Figure 111. Fluent solver setup.

25. Run calculation was selected. The time step size was input as 2.5e-6, the number of time steps as 400 or higher, and the max iteration per time step as 30.
26. Everything was double-checked and the project was saved before pressing calculate.
27. Calculate was pressed, and the live scaled residual plot showed up along with the animations after one time step.

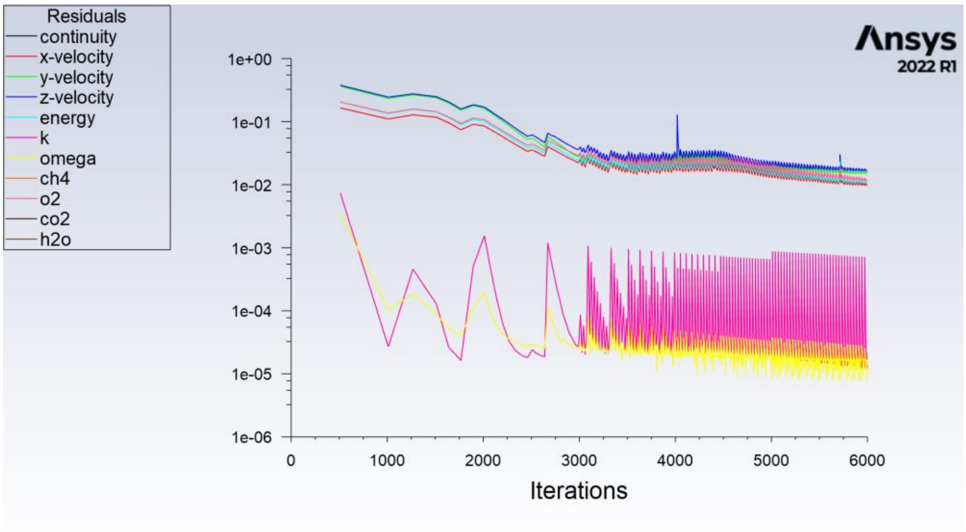

Figure 112. Residuals.

28. The time to complete one case varied depending on the number of iterations and animations.
29. When b2 reached the end of the domain, a pop-up window appeared saying “Update dynamic mesh failed. Negative cell volume detected,” indicating the calculation was complete.

8.6 Post Processing

After completing the calculation, all the files were copied into a separate folder before closing fluent. Next, to get the animation pictures, fluent was opened and the cxa files were read in the solution playback module. The resolution was changed to 1080 p and the picture files for each animation frame were written. Fluent can take around 15-20 minutes to generate all the pictures for an animation.

After obtaining the out file from Ansys, the file was converted into a txt file. The txt file was used as an input file on MATLAB to plot the result (drag of the projectile). The MATLAB code was reused for all simulation results.

8.7 Code

C code for Dynamic mesh:

```
#include "udf.h"

#include "dynamesh_tools.h"



/* Projectile Movement */



DEFINE_CG_MOTION(projectile, dt, vel, omega, time, dtime)

{

Thread *t;

face_t f;

vel[0]=1000;

}
```

MATLAB code:

Drag Components Plot:

```
close all

clear all



% Import the data from the out file using importdata

data = importdata('2bl_1000.txt');

name = '1000 m per second';

% name = 'P380-2BL-12-15';



% Extract parameter names from the 3rd row

fid = fopen('2bl_1000.txt');

for i = 1:2 % skip the first two lines

    fgetl(fid);

end

parameter_names_line = fgetl(fid);

parameter_names = strsplit(parameter_names_line);

fclose(fid);



% Extract columns for plotting

x = data.data(:, 1); % 1st column
```

```
y = (-1)*data.data(:, 17:20);

net_drag = sum(y,2);



% set plot size and position

plot_width = 800;

plot_height = 600;

figure('Position', [100,100,plot_width, plot_height]);



% Plot each column against the 1st column

plot(x,net_drag,'LineWidth', 1.5);

hold on;

for i = 1:size(y, 2)

    plot(x, y(:, i), 'LineWidth', 1.5);

end

hold off;



% xlabel(parameter_names{1}); % Label for the x-axis

xlabel('Time step'); % Label for the x-axis

ylabel('Drag (N)'); % Label for the y-axis

% ylim([-300, 760]);

ylim([-300, 1800]);
```

```
legend_labels = strrep(parameter_names(17:20), '_', ' ');
legend('Net drag', legend_labels{:}, 'Location', 'best');
title(name,'Drag vs. Time step');

new_drag = net_drag(end-71:end);
avg_drag = mean(new_drag)
rho = 22.8;
v = 1000;
A = 0.00012;
Cd = avg_drag/(0.5*rho*A*v^2)
t_drag = y(end-71:end,4);
avg_t_drag = mean(t_drag)

s_drag = y(end-71:end,3);
avg_s_drag = mean(s_drag)
n_drag = y(end-71:end,2);
avg_n_drag = mean(n_drag)
b_drag = y(end-71:end,1);
avg_b_drag = mean(b_drag)
```

```
% % Save the plot in PNG format with the same filename

% saveas(gcf, [name, '.png']);



% Specify the folder where you want to save the PNG file

folder = 'C:\Users\Dell\Downloads\thesis\postprocess\all_plots'; % Specify your desired folder path



% Check if the folder exists, if not, create it

if ~exist(folder, 'dir')

    mkdir(folder);

end



% Define the filename for the PNG file

filename = fullfile(folder, [name, '.png']);



% Save the plot as a PNG file

saveas(gcf, filename);



disp(['Plot saved as: ', filename]);
```

Mach vs. Thrust, Drag and Cd Plot:

```
% Define the data
mach_thrust = [2.77, 3.1, 3.46, 3.72];
thrust = [5.5, 13.4, 9.6, 8];

mach_cd = [2.256, 2.820, 3.384, 3.948, 5.640];
cd = [0.169, 0.1943, 0.2422, 0.24, 0.2066];

drag = [148, 266, 477 ,643 ,1130];

% set plot size and position
% plot_width = 800;
% plot_height = 600;
% figure('Position', [100,100,plot_width, plot_height]);

% Plot Mach vs. drag on the left y-axis
yyaxis left;
plot(mach_cd, drag, '-s', 'LineWidth', 2, 'MarkerSize', 8);
ylabel('Drag');
xlabel('Mach');
```

```
title('Mach vs. Thrust and Drag of P380-2BL-12-15');

% % Plot Mach vs. Cd on the left y-axis
% yyaxis left;
% plot(mach_cd, cd, '-s', 'LineWidth', 2, 'MarkerSize', 8);
% ylabel('Cd');
% xlabel('Mach');
% title('Mach vs. Thrust and Cd of P380-2BL-12-15');

grid on;

% Plot Mach vs. Thrust on the right y-axis
yyaxis right;
plot(mach_thrust, thrust, '-o', 'LineWidth', 2, 'MarkerSize', 8);
ylabel('Thrust');

% Adjust axes properties
set(gca, 'YColor', 'k'); % Set the color of the right y-axis to black

% Display legend
legend('drag', 'Thrust', 'Location', 'best');
```

```
% % Display legend

% legend('Cd', 'Thrust', 'Location', 'best');



% Save the plot as a PNG file

saveas(gcf, 'Mach_vs_Thrust_and_drag.png');



% % Save the plot as a PNG file

% saveas(gcf, 'Mach_vs_Thrust_and_Cd.png');
```